AN ABSTRACT OF THE DISSERTATION OF

Pedram Pakseresht for the degree of Doctor of Philosophy in Mechanical Engineering presented on March 16, 2020.

Title: On the Euler-Lagrange Modeling of Particle-laden Turbulent Flows

Abstract approved: _____
Sourabh V. Apte

Particle-laden turbulent flows, wherein a large number of small size particles are dispersed in a fluid, are widely encountered in environmental and industrial applications. Understanding their underlying physics, making predictions without performing expensive experiments, and ultimately optimizing the systems carrying such flows, require accurate and robust modelling tools. The Euler-Lagrange (EL) approach has received much attention in modeling such flows due to its simplicity, affordability and partial accuracy. In this approach, the fluid phase is solved using an Eulerian framework while particles are treated as Lagrangian point-particles (PP) in the flow and tracked following the Newton's second law of motion based on the available closures for the fluid forces acting on the particles.

For two-way coupled flows, the effect of particles on the fluid phase is modelled by applying the particle reaction force to the background flow through a momentum source term. Using such a simplified point force model, however, could result in inaccuracies in capturing the experimental observations or analytical solutions. One source of inaccuracy is that, the fluid phase equations in this approach are solved for the entire flow field including the volume occupied by the particles, and the mass displacement of the particles is not taken into account. The other source is that the accuracy of the fluid forces acting on the particles depends on the

'undisturbed fluid velocity', that is by definition, the velocity that is not influenced by the presence of particles. However, in two-way coupled simulations, particles disturb the fluid phase at their location, and such an 'undisturbed' fluid velocity is no longer available. The alternative and common use of the disturbed fluid velocity can produce erroneous predictions by as much as 100%.

In this dissertation, the spatio-temporal variations in the volume fraction of the fluid phase are taken into account to capture the mass displacement effect of particles. Large-eddy simulations (LES) coupled with PP approach performed for a particle-laden jet under a range of volume loadings show that the mass displacement effect tends to become important for particle volume loadings above 5%. Concerning the second issue, a general scheme is developed to correct the PP approach in order to recover the undisturbed fluid velocity at the location of particles. The model is accurate, cost-efficient and applicable for isotropic and anisotropic grids with high aspect ratio typically encountered in the turbulent channel flow simulations. The present scheme handles all types of particle-laden flows with and without no-slip walls. Tests performed on a settling particle in parallel and perpendicular motion to a no-slip wall shows the accuracy and robustness of the model in reducing the errors in predicting the particle settling velocity.

The present EL-PP approach is applied to a particle-laden turbulent channel flow to predict the interaction of particle and turbulence. It is observed that the uncorrected PP approach, wherein the disturbed fluid velocity is employed for the fluid force computations, fails in capturing the experimental observations. However, when the PP approach is corrected with the newly developed correction scheme, the recovery of the undisturbed fluid velocity at the location of particles produces accurate fluid forces and captures most of the experimental observations.

Finally, the effect of deforming particles, such as liquid droplets in liquid atomization, is briefly investigated. Different deformation models are tested against the experimental data to identify the best model for each breakup regime. It is observed that ignoring such an effect produces significant underprediction on the motion of droplets.

On the Euler-Lagrange Modeling of Particle-laden Turbulent Flows

by

Pedram Pakseresht

A DISSERTATION

submitted to

Oregon State University

in partial fulfillment of
the requirements for the
degree of

Doctor of Philosophy

Presented March 16, 2020
Commencement June 2020

Doctor of Philosophy dissertation of Pedram Pakseresht presented on
March 16, 2020.

APPROVED:

_____

Major Professor, representing Mechanical Engineering

_____

Head of the School of Mechanical, Industrial, and Manufacturing Engineering

_____

Dean of the Graduate School

I understand that my dissertation will become part of the permanent collection of
Oregon State University libraries. My signature below authorizes release of my
dissertation to any reader upon request.

_____

Pedram Pakseresht, Author

ACKNOWLEDGEMENTS

CONTRIBUTION OF AUTHORS

Dr. Sourabh V. Apte contributed to the development of the numerical method used in Chapter 2 as well as to the interpretation of the results throughout this dissertation. Dr. Mahdi Esmaily contributed to the development as well as the interpretation of the results of Chapter 3.

TABLE OF CONTENTS

LIST OF FIGURES

LIST OF FIGURES (Continued)

LIST OF TABLES

To my parents and my family, for their love and support

Chapter 1   Introduction

Turbulent flows laden with solid particles, liquid droplets or gaseous bubbles are common in both natural phenomena and man-made systems. Sediment transport in river, liquid atomization in combustion process, contaminant transport in industry, pollutant dispersion in the atmosphere, and drug delivery among others are some examples of these flows. It is worth noting that further on in this dissertation, the word 'particle' represents all types of the dispersed phases unless otherwise mentioned. Particles in such flows interact with the background flow through the exchange of mass, momentum and energy that could affect the characteristic or performance of these flows. In order to better understand their underlying physics, make predictions without performing expensive experiments, and ultimately optimize the current systems, accurate and affordable predictive tools are required. In this dissertation, efforts are made to improve the predictive capability and accuracy of the current approaches in modeling of these flows.

Studying the characteristics of particulate turbulent flows helps improve modeling of these flows more accurately and practically. One of the interesting observations is the preferential concentration of particles. It is widely accepted that even in isotropic turbulence, particles' distribution is not uniform and heavier-than-fluid particles tend to accumulate in regions of high strain rate with avoiding intense vorticity regions. On the contrary, lighter-than-fluid particles accumulate in vortical regions (Maxey (1987); Squires & Eaton (1990, 1991)), signifying the importance of the density ratio between phases, ρ_p/ρ_f.

Turbulent modulation due to the presence of particles is another phenomenon that depends on two parameters; (i) Stokes number, $St=\tau_p/\tau_f$, which is the ratio of particle relaxation time (τ_p) and fluid time scale (τ_f), and (ii) the volume loading of particles, $\phi_p=V_p/(V_p+V_f)$, where V_p and V_f represent the total volume of particles and fluid, respectively. Elghobashi (1991, 1994, 2006) classified a map for such a

modulation with identifying the type of interaction between both phases. They showed that for volume loadings of $\phi_p \leq 10^{-6}$, particles do not affect the turbulence, yet they are dispersed by the background flow, hence one-way coupled regime. For larger volume loadings ($10^{-6} < \phi_p < 10^{-3}$), however, the momentum transfer from particles to the flow is large enough that the background flow gets influenced and the regime is called two-way coupled.

They showed that depending on the St number, turbulence of the background flow could be attenuated or augmented. The former occurs for particles smaller than the size of the most energetic eddies, as a fraction of energy of the eddies is spent for dragging and carrying such small particles (Elghobashi, 2006). Conversely, for a given volume loading, increasing in the particle relaxation time or its length scale increases particle Reynolds number ($Re_p = \rho_f d_p |u_p - u_f|/\mu_f$), and for $Re_p \geq 400$ vortex shedding takes place behind the particles, hence turbulence augmentation (Gore & Crowe, 1989). Increasing the loading of particles to $\phi_p > 10^{-3}$, results in the inter-particle collisions in addition to the inter-phase interaction, which make the regime four-way coupled.

A variety of numerical methods has been developed up to date for modeling the different regimes of particle-laden flows. Balachandar (2009); Balachandar & Eaton (2010) classified a range of applicability of the different computational schemes based on two parameters (i) the relative size of particle to the smallest flow scale (d_p/Δ) and (ii) the volume loading of particles (ϕ_p). In ascending order of cost and accuracy, these numerical schemes are (i) Euler-Euler, (ii) Euler-Lagrange, and (iii) particle-resolved techniques. In the Euler-Euler approach (Crowe *et al.*, 1996), particles are simulated as a continuum using Eulerian framework that is also used to solve the fluid phase. This method is suitable for flows with large number of particles, however, its accuracy degrades for inertial particles. The next level of accuracy is the Euler-Lagrange (EL) method that has the longest history in the field (Maxey, 1987; Elghobashi, 1991; Squires & Eaton, 1991) and has received much attention in simulating particle-laden flows due to its simplicity, affordability and partial accuracy. This approach was initially introduced for modeling dilute

particle-laden flows with relatively small size particles that have negligible effects on the background flow. For such one-way coupled flows (Elghobashi, 1991), imposing the no-slip boundary condition on the surface of particles is not needed as the perturbation generated at the particle scale is insignificant. The fluid phase is solved using an Eulerian framework while particles are treated as Lagrangian point-particles (PP) in the flow and tracked following the Newton's second law of motion based on the available closures for the fluid forces acting on them. Such one-way coupled simulations are mostly used for particle tracking and clustering. Nevertheless, owing to its affordability, this EL-PP approach has also been applied to particulate flows with dense loading or those with relatively large size particles wherein the effect of particles on the background flow is inevitable (Squires & Eaton, 1990; Elghobashi & Truesdell, 1993). For such two-way coupled flows, the effect of particles on the carrier phase is modelled by applying the particle reaction force to the background flow through a momentum source term. Using such a simplified point force in modelling the inter-phase interactions, however, could result in some inaccuracies in capturing the experimental observations (Segura, 2004; Eaton, 2009; Pakseresht *et al.*, 2017) or analytical solutions (Pan & Banerjee, 1996) of particle-laden flows.

While the particle-resolved (PR) techniques provide the most accurate solution for particle-laden flows, they are extremely expensive and impractical for realistic flows involving thousand or millions of particles. Therefore, there is a pressing need for developing affordable and accurate methods for modeling flows laden with relatively large number of particles. Such a need has motivated research to fill the gap between EL and PR techniques. The focus of this dissertation is to fill such a gap and improve the predictive capability of the EL-PP approaches for two-way coupled regimes wherein the lack of accuracy has widely been observed. One source of inaccuracy is that the fluid phase equations in this approach are solved for the entire flow field including the volume occupied by the particles, and the volume/mass displacement of the particles is not accounted for. Several works have shown the considerable effects of this displacement and argued that

this effect should be included in addition to the point-particle force (Ferrante & Elghobashi, 2004; Apte *et al.*, 2008; Cihonski *et al.*, 2013). The other one is that the accuracy of this method in predicting the fluid forces on the particles can decay when the two phases are two-way coupled, owing to the disturbance created by the particles' force on the background flow. Such a disturbance produces an error in the fluid force computations since the closure models often rely on the slip velocity computed based on the *undisturbed* fluid flow, which is not readily available in the two-way coupled simulations.

In Chapter 2, the first issue that is the mass displacement effect of particles on the EL-PP predictions is investigated. Large Eddy Simulations (LES) of a particle-laden jet flow with a wide range of particle volume loadings and particle Stokes numbers is studied. The standard PP approach, wherein the mass displacement effect is ignored, is compared with the modified PP approach wherein such a displacement effect is taken into account. It is shown that for inlet volume loadings above 5%, the displacement effect alters both mean and r.m.s. velocities of the background flow. This chapter is published in the International Journal of Multiphase Flow. In Chapter 3, the second issue is addressed and a general velocity correction scheme is developed to recover the undisturbed fluid velocity at the location of particles, in the presence or absence of no-slip walls, to capture the accurate fluid forces acting on the particles. The model is accurate and cost-efficient, and can handle isotropic and anisotropic grid resolutions that are typically encountered in turbulent channel flows. The newly developed model reduces the errors associated with the prediction of settling velocity of a particle to few percent. Both parallel and perpendicular motions of a particle respective to a no-slip wall are examined at various wall distances. This chapter is submitted to the Journal of Computational Physics and is under review. In Chapter 4, formulations developed in Chapters 2 and 3 are applied to a full-fledged particle-laden turbulent channel flow. It is shown that the standard uncorrected PP approach fails in capturing the effect of particles on the flow. In other words, predictions of turbulent channel flow with and without particles are almost identical in the uncorrected approach.

However, the corrected PP scheme is able to capture the effects of particles on the flow, in consistent with the experimental observations. This chapter is under preparation for submitting to the International Journal of Multiphase Flow. Chapter 5, investigates the effect of deforming particles, e.g., liquid droplets in sprays and liquid atomization processes. Different deformation models are investigated for different breakup regimes with identifying the best model for each regime. It is shown that ignoring such an effect could produce significant underprediction in the dynamics of droplets. This chapter was presented and published in the proceeding of ILASS-Americas, 30th Annual Conference on Liquid Atomization and Spray Systems, Tempe, AZ, May 2019. Finally, conclusions of this dissertation and suggestions for the future works are given in Chapter 6.

Chapter 2   Volumetric displacement effects in Euler-Lagrange LES predictions of particle-laden jet flows

Pedram Pakseresht and Sourabh V. Apte

Abstract

Large-eddy simulations (LES) of a particle-laden jet under a range of volume loadings are performed using a modified point-particle Euler-Lagrange (EL) approach to evaluate the effect of the volume/mass displaced by the subgrid particles on the flow. The spatio-temporal variations in the volume fraction of the carrier phase are taken into account giving rise to a zero-Mach number, variable density formulation with source terms in both momentum and continuity equations. The influence of volume loading as well as particle relaxation time on these volumetric displacement effects are investigated by performing numerical tests at different inlet volume loadings (0.047%-37.6%) and Stokes numbers (0.038-11.6). It is shown that for volume loadings above 5%, the volumetric displacement effects tend to become important. For the cases studied, these effects increase the mean and r.m.s. velocities of the carrier phase due to the continuity source term; however, they decrease further downstream due to dispersion of particles and spreading of the jet. It is observed that reducing the particle Stokes number increases the volumetric displacement effects due to their quick response time to the changes in the background flow, lower dispersion and smaller reaction forces.

2.1   Introduction

Liquid spray atomization plays an important role in analyzing the combustion process in many propulsion related applications. A standard modeling approach for liquid fuel atomization is to use a two step process involving primary followed by secondary atomization as shown in Fig. 2.1. During primary atomization the liquid exhibits relatively few complex coherent structures that undergo breakup initiated by a multitude of physical mechanisms. The secondary atomization region is characterized by a vast number of droplets that interact with the surrounding
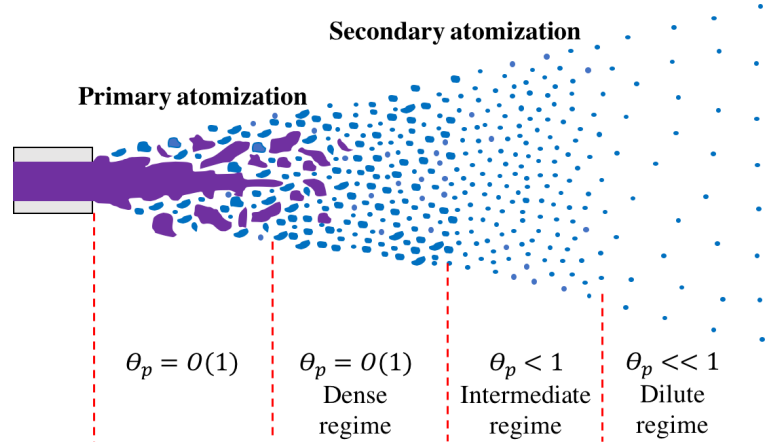
Figure 2.1: Different regimes in a liquid atomization process modified based on Herrmann (2010b).

fluid transferring mass, momentum, and energy and can be characterized by three different regimes as shown in Fig. 2.1. In the dense regime, the local liquid volume fraction, θ_p, (subscript 'p' refers to the dispersed phase) is on the order of one with liquid droplets undergoing secondary breakup. In the intermediate regime, droplets continue to undergo further disintegration; however, θ_p is now smaller than unity. Finally, in the dilute regime, atomization is rare, θ_p is small, the droplets evaporate, and the fuel vapor mixes with the surrounding hot gases (Herrmann, 2010b). In the dense and intermediate regimes, not only are droplet deformation, collision, and coalescence important, but significant droplet-loading and local variations in θ_p are crucial and should be considered to capture the spray evolution correctly.

In the traditional approaches for spray modeling, the dynamics of the liquid/gas interface are not resolved. Instead the spray dynamics is modeled using an EL point-particle/parcel approach where liquid droplets are assumed subgrid and their motion is captured by laws for drag, lift, added mass, and pressure forces due to the gas phase. Their effect on the carrier phase is then modeled through two-way coupling of mass, momentum, and energy exchange with the Eulerian equations of the gaseous phase (Dukowicz, 1980). Liquid blobs with the size of the injector diam-

eter are introduced into the combustion chamber that undergo atomization based on either deterministic breakup models such as Taylor analogy breakup (TAB) (O'Rourke & Amsden, 1987) and wave models (Reitz, 1987) or stochastic breakup models (Apte *et al.*, 2003). Alternative approaches for modeling atomization include the $\Sigma - Y$ model (Vallet & Borghi, 1999; Vallet *et al.*, 2001) that considers atomization as a turbulent mixing process, the Eulerian-Lagrangian Spray Atomization (ELSA) approach which couples the Eulerian mixing description of primary atomization for both phases to an EL formulation for the secondary atomization (Blokkeel *et al.*, 2003; Lebas *et al.*, 2005; Ning *et al.*, 2009). These models were originated in the context of Reynolds-Averaged Navier-Stokes equations (RANS) turbulence models; however, extensions to LES formulations have been recently proposed by Chesnel *et al.* (2011*b*,*a*).

In EL point-particle approach, the volume fraction and size of the dispersed phase is assumed small compared to the computational cell, so that point-particle assumption (Maxey & Riley, 1983; Maxey, 1987; Squires & Eaton, 1991) is practical and feasible. This approach, however, is not strictly applicable to regions with high volume fraction of the dispersed phase such as near the nozzle injector where the dispersed phase could displace a remarkable portion of the carrier phase. This results in spatio-temporal variations in local volume fraction of the carrier phase.

Recently, hybrid approaches of direct numerical simulation (DNS) for the primary atomization along with LES coupled with point-particle/parcel approach for the secondary atomization have been developed by Herrmann (2010*b*,*a*, 2011). They have shown quite success in predicting atomization even in complex aircraft engine injectors, yet they are still computationally expensive. On the other hand, the spatio-temporal variations in volume fraction of the carrier phase are still neglected in dense regime of EL secondary atomization. Accounting for these effects was originally proposed by Dukowicz (1980) in the context of spray simulations and modified later by Joseph *et al.* (1990). In this formulation, the carrier and dispersed phases are coupled volumetrically by two mechanisms: (i) displacement of the carrier phase by the volume occupied by particles, and (ii) momentum exchange

between the phases through a reaction force. However, the volume displacement effects are typically ignored in most EL dense spray simulations because of the complexity of the numerical algorithm embedded in this formulation.

Several works have depicted the importance of accounting for the volume/mass displaced by the dispersed phase in EL approaches. Patankar & Joseph (2001a) utilized this scheme for sedimentation column of dense particles, while Snider (2001) used similar formulation for some canonical test cases on laminar dense particle-laden flows. Ferrante & Elghobashi (2004, 2005) observed that taking into account for the volumetric displacement effects results in accurately capturing the drag reduction in a microbubble-laden turbulent boundary layer over a flat plate. The local negative velocity divergence, $\nabla \cdot \mathbf{u_f} < 0$, created by bubble concentration was found to be the physical mechanism behind this reduction. In contrast, Vreman $et\ al.$ (2004) showed insignificant difference in the prediction of this approach for a particle-laden channel flow with average loading of 1.3% compared to the standard two-way coupling EL method where these effects are neglected. Deen $et\ al.$ (2004, 2007), Darmana $et\ al.$ (2006) applied this formulation in the context of gas-liquid two-phase flows as mentioned in a comprehensive review by Van der Hoef $et\ al.$ (2008). Apte $et\ al.$ (2008) illustrated a large difference in the prediction of particle dispersion in fluidization process using this approach compared to the standard Euler-Lagrange approach. They showed that the fluid displaced by the particles plays an important role in predicting the correct behavior of particle motion. However, most of the cases studied were for low density ratio of the dispersed phase and the carrier flow on the order of 1 to 10. In line with previous works, Finn $et\ al.$ (2011) and Cihonski $et\ al.$ (2013) showed that under some conditions, the entrainment of eight small bubbles, 1100 μm or less in diameter, results in significant levels of vortex distortion matching the corresponding experimental observations when the volumetric displacement effects of the bubbles are taken into account. Neglecting these effects, however, did not result in any vortex distortion. Shams $et\ al.$ (2011) and Capecelatro & Desjardins (2013) presented EL strategies for simulating turbulent flows in complex geometries using this formulation. Fox (2014)

provided a rigorous derivation of a Reynolds-average turbulence model for colli-sional fluid-particle flows showing that new turbulence production terms arise due to correlations between the particle-phase volume fraction and fluid-phase velocity fluctuations. Capecelatro *et al.* (2014) employed this formulation in the context of granular flows where a strong correlation between the local volume fraction and the granular temperature was shown in the results of fully developed cluster-induced turbulence. Finn *et al.* (2016) applied this formulation for simulation of natu-ral sand dynamics in the wave bottom boundary layer wherein overall excellent agreement between simulation and experiments was achieved.

Recently, a new point-particle approach, pairwise interaction extended point-particle (PIEP), that accounts for the influence of neighboring particles in EL approaches was introduced by Akiki *et al.* (2017*a,b*). Perturbation induced by each neighbor is considered separately, then the effects of all neighbors are lin-early superposed to obtain the total perturbation. They observed the new model predicts much closer to the particle-resolved DNS results than the classical point-particle approach. This could be a complementary approach for current EL formu-lations upon its availability and implementation in the current packages. However, whether this approach is able to capture the volumetric displacement effects leaves an open question for further investigations.

In this work, LES coupled with point-particle approach modified with spatio-temporal variations in the volume fraction of the carrier phase is used for studying the volumetric displacement effects of this phase on the characteristics of dense sprays. To isolate this specific effect; breakup, coalescence, evaporation and de-formation in shape and size of the dispersed phase are masked by performing simulations of solid particle-laden turbulent round jet flow. Results of this formu-lation are compared with those of standard EL point-particle approach where these effects are neglected. To quantify the effects of volume displacement from dilute to dense regimes, a range of particle volume loadings are considered by keeping other parameters constant. In addition, the influence of Stokes number on the volume displacement effects are investigated.

The studied cases (A-F) are shown in Fig. 2.2, a classification map by El-ghobashi (1991) on the particle-turbulence interactions. This map is based on the Stokes number, $St=\tau_p/\tau_f$, and the average volume fraction of particles, θ_p. Stokes number is defined as the ratio of particle response time for Stokes flow, $\tau_p=\rho_p d_p^2/18\mu_f$, and turnover time of large eddy, $\tau_f=l/u$. As explained in El-ghobashi (1991, 1994, 2006) and illustrated in Fig. 2.2, the one-way coupling region is identified for flows where the motion of particles is affected by turbulence; however, due to very low values of θ_p ($\leq 10^{-6}$) they have negligible effects on turbulence. In the two-way coupling regime, the volume loading of particles is large enough, $10^{-6}<\theta_p\leq 10^{-3}$, to affect the turbulence structure through the momentum exchange between fluid and particle phases. In the four-way coupling, because of the high loading of particles, $\theta_p>10^{-3}$, the inter-particle collision occurs in addition to the two-way coupling interaction of turbulence and particles. However, collisions should also be included if the overall volume fraction is smaller than 10^{-3} as in some particular flows there are regions in which, due to preferential concentration, the local volume fraction is larger than 0.001 (Vreman (2007), Kuerten & Vreman (2015)). In addition, it is possible that the mass loading which has the effect of both density ratio and volume loading plays an important role instead of volume loading alone in identifying the different couplings.

As Fig. 2.2 depicts, case A lies in the close proximity to the two-way coupling region while the rest, B-F, lie in the dense suspension region where inter-particle collisions as well as two-way coupling between phases become important. In the physics of dense suspensions the displacement effects are inherently embedded in the two-way coupling between phases; therefore, any accurate experimental measurement or particle-resolved DNS result would essentially capture the volume displacement effects in this region. However, in the modeling of two-way coupling mechanism in the dense regions using an EL point-particle approach, where neither the interface between phases is directly resolved by first principles nor accurate boundary conditions are applied on the surface of particles, the volume displacement effects are not necessarily captured. Accordingly, we hypothesize
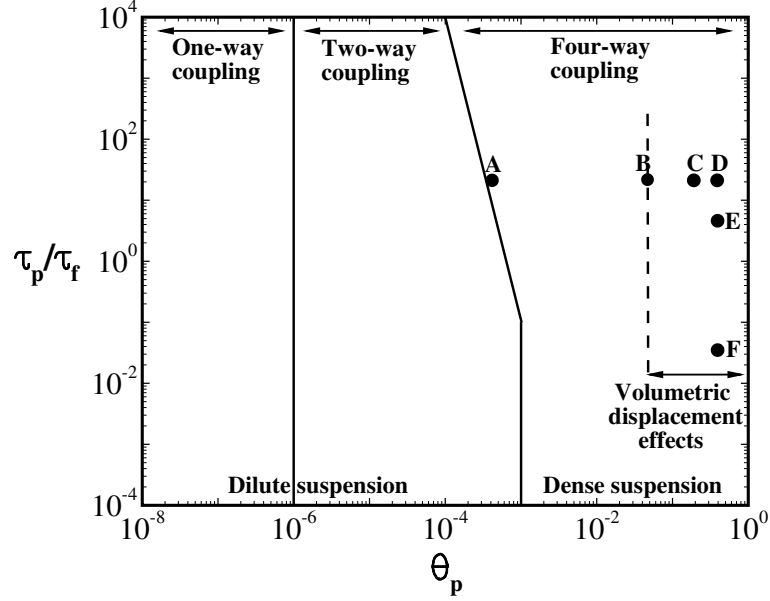
Figure 2.2: Classification map on particle-turbulence interactions by Elghobashi (1991).

that in the dense regimes (e.g. B-F) the standard momentum exchange force typically employed in common EL point-particle approaches might be insufficient to accurately capture the physics of these regimes and necessitates accounting for the volume displacements. In line with work of Shams *et al.* (2011); Finn *et al.* (2011); Cihonski *et al.* (2013), throughout the paper if volume displacement of the carrier phase is accounted for, the particle-turbulence interaction coupling is named *volumetric coupling* while the standard coupling is used if this effect is excluded.

The rest of paper is arranged as follows. Section 2.2 describes the mathematical formulation of EL point-particle approach modified with spatio-temporal variations in the volume fraction of the carrier phase. Source terms that appear in both momentum and continuity equations due to volume displacement of the carrier phase are described. Section 2.3 compares results of the standard EL point-particle approach with those of volumetric coupling on the prediction of particle-laden

turbulent round jet. With this comparison, the volumetric displacement effects of the carrier phase are identified at different particle loadings and Stokes numbers. Section 2.4 concludes the paper with final remarks and summary of the work.

2.2 Mathematical description

An EL approach is used wherein the carrier phase is captured through solving the momentum and continuity equations in an Eulerian LES framework whereas motion of solid particles is modeled in a Lagrangian framework with closure models for forces. As in the point-particle approach (Maxey, 1987; Elghobashi, 1991; Squires & Eaton, 1991), the dispersed phase particles are assumed subgrid and their motion is captured by tracking their centroids using Newton's laws. However, unlike point-particle approach, wherein the particles are assumed as point sources, the volume of each particle is taken into account thus modifying the interaction between the two phases primarily by two mechanisms: (i) the displacement of the carrier phase by the volume occupied by the particles and (ii) momentum exchange through reaction force between the phases. Details of the governing equations are given in the following sections.

2.2.1 Carrier phase formulation

The volume-averaged governing equations used for turbulent jet flow laden with point-particles are given in Eq. 2.2.1 and 2.2.2 (Anderson & Jackson, 1967; Dukowicz, 1980; Joseph *et al.*, 1990).

$$\frac{\partial}{\partial t}(\rho_f \theta_f) + \frac{\partial}{\partial x_j}(\rho_f \theta_f u_j) = 0 \qquad (2.2.1)$$

$$\frac{\partial}{\partial t}\left(\rho_f\theta_f u_i\right) + \frac{\partial}{\partial x_j}\left(\rho_f\theta_f u_i u_j\right) =$$

$$-\theta_f\frac{\partial P}{\partial x_i} + \frac{\partial}{\partial x_j}\left[2\mu_f\theta_f\left(\frac{1}{2}\left(\frac{\partial u_i}{\partial x_j}+\frac{\partial u_j}{\partial x_i}\right)-\frac{1}{3}\delta_{ij}\frac{\partial u_k}{\partial x_k}\right)\right] + \rho_f\theta_f g_i + F^t_{i,p\rightarrow f}$$

$$(2.2.2)$$

where g_i is the gravitational acceleration, μ_f, ρ_f, θ_f, and u_f are dynamic viscosity, density, volume fraction, and velocity of the carrier phase, respectively. Volume fraction of the carrier phase in each computational cell is calculated as $\theta_f{=}1-\theta_p$, where θ_p corresponds to the volume fraction of particles (N_p) at the cell centroid, $\mathbf{x}_{cv}$, and is computed as

$$\theta_p(\mathbf{x}_{cv}) = \sum_{p=1}^{N_p}\vartheta_p G_\sigma(\mathbf{x}_{cv},\mathbf{x}_p) \qquad (2.2.3)$$

where $\mathbf{x}_p$ and ϑ_p are the location and volume of each particle in the cell, respectively. The function G_σ is used to interpolate Lagrangian quantities at the Eulerian field and is defined later in Eq. 2.2.18. The point-particle force, $F^t_{i,p\rightarrow f}$, includes the equal and opposite reaction forces from the particle surface forces excluding the pressure force (Van der Hoef *et al.*, 2008; Cihonski *et al.*, 2013). Note that the pressure term in the momentum equation can be expanded as two separate terms as (Cihonski *et al.*, 2013)

$$-\theta_f\frac{\partial P}{\partial x_j} = -\frac{\partial P}{\partial x_j} + \theta_p\frac{\partial P}{\partial x_j} \qquad (2.2.4)$$

The second term, $\theta_p\partial P/\partial x_j$, is the pressure-gradient force, $F_{i,pr}$, which can be considered as the reaction due to pressure-gradient force on the particles. This term can be added to the particle reacting forces, thus $F_{i,p\rightarrow f}{=}F^t_{i,p\rightarrow f}{+}F_{i,pr}$, and then momentum equation is rewritten as

Abbreviation	Coupling type	$F_{i,p \to f}$	Volumetric displacement effects
S1W	Standard one-way coupling	No	No
V1W	Volumetric one-way coupling	No	Yes
S2W	Standard two-way coupling	Yes	No
V2W	Volumetric two-way coupling	Yes	Yes

Table 2.1: Terminologies used for different couplings in EL formulations.

$$\frac{\partial}{\partial t}\left(\rho_f \theta_f u_i\right) + \frac{\partial}{\partial x_j}\left(\rho_f \theta_f u_i u_j\right) =$$
$$-\frac{\partial P}{\partial x_i} + \frac{\partial}{\partial x_j}\left[2\mu_f \theta_f \left(\frac{1}{2}\left(\frac{\partial u_i}{\partial x_j} + \frac{\partial u_j}{\partial x_i}\right) - \frac{1}{3}\delta_{ij}\frac{\partial u_k}{\partial x_k}\right)\right] + \rho_f \theta_f g_i + F_{i,p \to f}$$
$$(2.2.5)$$

Rewriting the momentum equation in this fashion is advantageous as this leads to a constant coefficient Poisson equation for pressure as shown in Cihonski *et al.* (2013); Shams *et al.* (2011). Since the zero-Mach number variable density equations account for the volumetric displacement of the carrier phase as well as point-particle forces, thus the inter-phase coupling is named volumetric two-way coupling (V2W). Setting $\theta_f{=}1$ in the above formulation, the standard two-way coupling (S2W) is recalled in which the displacement effects are neglected. In addition, volumetric one-way coupling (V1W) can simply be achieved by setting $F_{i,p \to f}{=}0$ while the volumetric displacement is still maintained. In this case, the carrier phase is not affected by the point-particle force; however, is altered by the volumetric displacement. Note that setting $F_{i,p \to f}{=}0$ and $\theta_f{=}1$, the standard one-way coupling (S1W) is obtained. Table 2.1 describes these inter-phase couplings. It should be noted that throughout the paper the two-way terminology is used for the inter-phase coupling in regimes with $\theta_p{>}10^{-6}$; however, accounting for the inter-particle collisions is mentioned separately if required.

For LES, the equations above are spatially filtered using Favre (density-weighted)

averaging (e.g., $\overline{\rho\theta u}=\overline{\rho\theta\widetilde{u}}$) where the filtering operation is denoted by an overbar and density-weighted Favre averaging by a tilde (Moin & Apte, 2006). The governing equations for LES of particle-laden turbulent flow then become

$$\frac{\partial}{\partial t}\left(\overline{\rho_f\theta_f}\right) + \frac{\partial}{\partial x_j}\left(\overline{\rho_f\theta_f}\widetilde{u}_j\right) = 0 \tag{2.2.6}$$

$$\frac{\partial}{\partial t}\left(\overline{\rho_f\theta_f}\widetilde{u}_i\right) + \frac{\partial}{\partial x_j}\left(\overline{\rho_f\theta_f}\widetilde{u}_i\widetilde{u}_j\right) = -\frac{\partial\widetilde{P}}{\partial x_i} + \frac{\partial}{\partial x_j}\left(2\overline{\mu_f\theta_f}\widetilde{S}_{ij}\right) - \frac{\partial q_{ij}^{r,vol}}{\partial x_j} + \overline{\rho_f\theta_f}g_i + F_{i,p\rightarrow f} \tag{2.2.7}$$

where,

$$\widetilde{S}_{ij} = \frac{1}{2}\left(\frac{\partial\widetilde{u}_i}{\partial x_j} + \frac{\partial\widetilde{u}_j}{\partial x_i}\right) - \frac{1}{3}\delta_{ij}\frac{\partial\widetilde{u}_k}{\partial x_k}. \tag{2.2.8}$$

Here, $\overline{\rho_f\theta_f}$ is the filtered density modified by local volume fraction. $\widetilde{u}_i$, $\widetilde{P}$ and $\widetilde{S}_{ij}$ are the Favre-averaged velocity field, pressure and rate of strain respectively.

The additional term in the momentum equation containing $q_{ij}^{r,vol}$, represents the subgrid-scale stress in the volumetric coupling formulation and is modeled using the dynamic Smagorinsky (Germano et $al.$, 1991; Moin et $al.$, 1991). The unclosed term in Eq. 2.2.7 is modeled using the gradient-diffusion hypothesis with eddy-viscosity as

$$q_{ij}^{r,vol} = \overline{\rho_f\theta_f}(\widetilde{u}_i\widetilde{u}_j - \widetilde{u_iu_j}) = 2\mu_t\widetilde{S}_{ij} - \frac{1}{3}\overline{\rho_f\theta_f}q^2\delta_{ij} \tag{2.2.9}$$

where $\frac{1}{2}\rho_f\theta_fq^2$ is the subgrid kinetic energy and the eddy viscosity, μ_t, is calculated as

$$\mu_t = C_\mu\overline{\rho_f\theta_f}\Delta^2|\widetilde{S}| \quad ; \quad \Delta = V_{cv}^{1/3} \quad ; |\widetilde{S}| = \left(\widetilde{S}_{ij}\widetilde{S}_{ij}\right)^{1/2} \tag{2.2.10}$$

where V_{cv} is the volume of the cell and the model constant, C_μ, is evaluated dynamically (Pierce & Moin, 1998). Note that in the volumetric coupling formulation the subgrid effects of fluid displacement are also present in the subgrid model. For the standard two-way coupling the subgrid-scale stress term, $q_{ij}^{r,2w}$, is simply obtained

by setting $\theta_f=1$ in the Eq. 2.2.9-2.2.10.

2.2.2 Dispersed phase formulation

Similar to the point-particle approach (Maxey & Riley, 1983), particles (smaller than the resolved fluid length scale) are tracked using the Newton's second law of motion as

$$\frac{d}{dt}(\mathbf{x}_p) = \mathbf{u}_p \qquad (2.2.11)$$

$$\frac{d}{dt}(\mathbf{u}_p) = \frac{1}{m_p}\left(\mathbf{F}_g + \mathbf{F}_{pr} + \mathbf{F}_d + \mathbf{F}_{l,Saff} + \mathbf{F}_{am}\right) \qquad (2.2.12)$$

where $\mathbf{x}_p$ and $\mathbf{u}_p$ denote the respective position and velocity components of each individual particle of mass m_p. Equation 2.2.12 shows all possible forces including gravitational body force, $\mathbf{F}_g$, hydrostatic pressure-gradient force, $\mathbf{F}_{pr}$, shear induced lift force (Saffman, 1965), $\mathbf{F}_{l,Saff}$, as well as added mass induced force (Auton, 1983), $\mathbf{F}_{am}$. In order to more accurately capture the particle-turbulence interactions involved in dense regimes, the drag closure, $\mathbf{F}_d$, by Tenneti *et al.* (2011) is employed where the coefficient of drag, $C_d(Re_p, \theta_p)$, accounts for the local volume fraction of the dispersed phase as well as finite particle Reynolds number effects. It has been observed that the Basset history force does not remarkably affect the motion of particles in the presence of steady drag force (Maxey & Riley, 1983; Bagchi & Balachandar, 2003); therefore, this force is excluded in this study. All aforementioned forces are given as follows

$$\mathbf{F}_g = (\rho_p - \overline{\rho_f})\vartheta_p\mathbf{g} \quad ; \quad g = -9.81m/s^2 \qquad (2.2.13)$$

$$\mathbf{F}_{pr} = -\vartheta_p\nabla\overline{P}_{f|p} \qquad (2.2.14)$$

$$\mathbf{F}_{l,Saff} = m_p C_l \frac{\overline{\rho_f}}{\rho_p} \left(\widetilde{\mathbf{u}}_{f|p} - \mathbf{u}_p \right) \times (\nabla \times \widetilde{\mathbf{u}}_f)_{|p} \quad ; \quad C_l = \frac{1.61 \times 6}{\pi d_p} \sqrt{\frac{\mu_f}{\overline{\rho_f}} | (\nabla \times \widetilde{\mathbf{u}}_f)_{|p} |}$$

$$(2.2.15)$$

$$\mathbf{F}_{am} = m_p C_{am} \frac{\overline{\rho_f}}{\rho_p} \left(\frac{D\widetilde{\mathbf{u}}_{f|p}}{Dt} - \frac{d\mathbf{u}_p}{dt} \right) \quad ; \quad C_{am} = 0.5 \qquad (2.2.16)$$

$$\mathbf{F}_d = m_p \frac{C_d(Re_p, \theta_p)}{\tau_p} \left(\widetilde{\mathbf{u}}_{f|p} - \mathbf{u}_p \right)$$

$$C_d \left(Re_p, \theta_p \right) = (1 - \theta_p) \left(\frac{C_d(Re_p, 0)}{(1 - \theta_p)^3} + A + B \right),$$

$$A = \frac{5.81\theta_p}{(1 - \theta_p)^3} + 0.48 \frac{\theta_p^{1/3}}{(1 - \theta_p)^4}, \qquad (2.2.17)$$

$$B = \theta_p^3 Re_p \left(0.95 + \frac{0.61\theta_p^3}{(1 - \theta_p)^2} \right),$$

$$C_d \left(Re_p, 0 \right) = 1 + 0.15 Re_p^{0.687}$$

where $\mathbf{u}_{rel} = \widetilde{\mathbf{u}}_{f|p} - \mathbf{u}_p$ is the relative velocity between phases at the location of parti-
cle. In addition, $\tau_p = (\rho_p d_p{}^2)/(18\mu_f \theta_f)$ and $Re_p = \overline{\rho_f \theta_{f|p}} |\mathbf{u}_{rel}| d_p / \mu_f$ are the respective
particle relaxation time and Reynolds number modified by its local volume fraction
(Finn *et al.*, 2016). D/Dt and d/dt denote the time derivative following the fluid
(material derivative) and particle phases respectively (Maxey & Riley, 1983).

Fluid velocity employed in drag calculation is defined based on the undisturbed
field. However, in two-way coupled EL calculations, this velocity is disturbed by
drag force thus producing less accurate predictions. Horwitz & Mani (2016, 2018);
Esmaily & Horwitz (2018) among others developed schemes to obtain the undis-
turbed velocity field in two-way coupled computations. Better accuracy in several
cases has been observed using these schemes; however, extension of these correc-
tions to dense regimes such as cases in this work requires further investigations.

Note that the unfiltered carrier phase velocity is required for force calculations

(Eq. 2.2.12); however, only the filtered field is computed in LES. Recently, Marchioli (2017) developed a conceptual classification of EL modeling approaches to the LES simulations of particle-laden flows as a function of two parameters. According to this classification, the subgrid particle Stokes number, St_{SGS}, and the ratio between LES filter and Kolmogorov length scale, Δ/η, are the relevant parameters. St_{SGS} is defined as the ratio of particle response time, τ_p, and cut-off time scale, $\tau_\Delta \sim (\Delta^2/\epsilon)^{1/3}$, where ϵ is energy dissipation. When $St_{SGS} \ll 1$, particles are sensitive to the unresolved high-frequency fluctuations of subgrid turbulence and a particle subgrid-scale (SGS) is required. In the opposite limit ($St_{SGS} \gg 1$), particles become SGS-inertial with respect to subgrid eddies and no particle SGS model is necessary. In the cases we studied here, the subgrid particle Stokes number is 28.33 for cases A-D (Tab. 2.2), and thus do not need a particle SGS model. For case F, however, the subgrid particle Stokes number is small (0.093), and thus the dynamics and preferential concentration of these particles will be affected by the particle SGS model. Although this might be important, since the scope of this work is comparing the standard and volumetric two-way coupling results, then the particle SGS model was neglected in both couplings. However, any coupled effect between the volumetric displacement and particle SGS model requires further investigation. It is worth mentioning that particles are indirectly affected by the fluid phase SGS model which affects the filtered velocity field.

For interpolations between the Eulerian grid points and Lagrangian particle locations, a Gaussian function is employed (Moin & Apte, 2006; Apte *et al.*, 2008). These interpolations are needed to compute fluid velocity at particle locations, projecting particle reaction forces to the Eulerian grid, and computing the volume fraction fields. The Gaussian interpolation scheme is given as

$$G_\sigma \left(\mathbf{x}_{cv}, \mathbf{x}_p \right) = \frac{1}{\left(\sigma \sqrt{2\pi} \right)^3} exp \left[-\frac{\sum_{i=1}^3 \left(x_{cv,i} - x_{p,i} \right)^2}{2\sigma^2} \right] \qquad (2.2.18)$$

where bandwidth, σ, is proportional to the grid size containing the particle. The interpolation stencil utilizes 6 neighboring grid cells in three-dimension as well as

the cell in which particle is located. $x_{cv,i}$ and $x_{p,i}$ are the positions of these cells and the particle of interest, respectively. Accordingly, depending on the location of particle in the grid, its volume will be weighted and distributed over these cells based on its distance from the cell centroid. For each particle, G_σ is normalized to satisfy

$$\oint_{V_{cv}} G_\sigma\left(\mathbf{x}_{cv}, \mathbf{x}_p\right) dV = 1 \qquad (2.2.19)$$

where the integration is performed over the cell containing the particle and all 6 neighbors. The final step is necessary to enforce mass (or volume) as well as force conservations. The Gaussian kernel provides quadrature spectral accuracy, provided that the interpolation is being performed over a region much larger than the bandwidth, otherwise the accuracy reduces to second order (Finn *et al.*, 2011).

2.2.3 Collision modeling

Inter-particle collision plays a crucial role in dynamics of the dense flows in addition to the inter-phase momentum two-way coupling forces. In order to model the collision in a physically realistic way, soft–sphere Discrete Element Model (DEM) based on work of Cundall & Strack (1979) is employed here. Collision force, $\mathbf{F}_{c,ij}$, generated by two particles undergoing collision is modeled by considering the overlap between particle-particle as a linear-damper system with spring constant (stiffness parameter), k_c, and damping constant, η_c, as

$$\mathbf{F}_{c,ij} = \begin{cases} -k_c\delta_{ij}\mathbf{n}_{ij} - \eta_c\mathbf{u}_{ij} & \text{for:}|\Delta\mathbf{x}_{ij}| < 0.5\left(d_{p,i} + d_{p,j}\right) + \alpha \\ 0 & \text{Otherwise} \end{cases} \qquad (2.2.20)$$

where,

$$\delta_{ij} = 0.5\left(d_{p,i} + d_{p,j}\right) - |\mathbf{x}_{p,i} - \mathbf{x}_{p,j}|, \qquad (2.2.21)$$

and $\Delta\mathbf{x}_{ij}{=}\mathbf{x}_{p,i}{-}\mathbf{x}_{p,j}$, $\mathbf{u}_{ij}{=}\mathbf{u}_{p,i}{-}\mathbf{u}_{p,j}$ and $\mathbf{n}_{ij}$ is the normal vector between two particles of i and j with position, diameter and velocity of $\mathbf{x}_p$, d_p and $\mathbf{u}_p$, respectively. Also, α is the radius of influence adjusted linearly as a function of collision CFL number in line with Capecelatro & Desjardins (2013). The damping parameter, η_c, is computed as (Patankar & Joseph, 2001b)

$$\eta_c = \frac{-2\ln\left(e\right)\sqrt{m_{ij}k_c}}{\sqrt{\pi^2 + \ln^2\left(e\right)}}, \tag{2.2.22}$$

where restitution coefficient, e, is taken to be 0.65 in line with Finn et $al.$ (2016) and $m_{ij}{=}m_i m_j/(m_i{+}m_j)$ is the reduced mass of colliding particles.

The stiffness parameter is important for the collision modeling and in fact can affect the clustering and dispersion of particles. For instance, increasing this parameter would increase the particle dispersion and consequently reduce the local volume fraction and volumetric displacement effects. This parameter could be calculated directly from the Young's and shear modulus of a material (Tsuji et $al.$, 1992); however, this would result in small collision events and impractical EL simulations for dense flows. In order to avoid this, lower values are commonly employed in the presence of dominant drag (Finn et $al.$, 2016). In the present configuration, especially near the injector, the particle volume fraction would still remain $\sim O(1)$, and thus collision parameters may not affect the present conclusions in that region. However, further downstream, indeed collision parameters can affect the local clustering and should be investigated in the future. This work aims to isolate the volumetric displacement effects by comparing the results of volumetric and standard two-way couplings; therefore, a small value for stiffness parameter in both couplings would be appropriate as long as the overlapping between particles is avoided.

2.2.4 Quantification of volumetric displacement effects

In this part the volumetric displacement effects are quantified. Cihonski *et al.* (2013) derived an expression for a momentum source term due to volumetric displacement effects. This was performed by writing the original conservative form of the volumetric coupling governing equations in a non-conservative form and expressing the additional terms as the volumetric displacement forces in comparison with the standard two-way coupling formulation. Here, we recall their derivation on spatially filtered equations employed in LES. The momentum equation in conservative form (Eq. 2.2.7) are expanded in a non-conservative form as

$$
\widetilde{u}_i \underbrace{\left(\frac{\partial}{\partial t} \left(\overline{\rho_f \theta_f} \right) + \frac{\partial}{\partial x_j} \left(\overline{\rho_f \theta_f} \widetilde{u}_j \right) \right)}_{I} + \overline{\rho_f \theta_f} \left(\frac{\partial \widetilde{u}_i}{\partial t} + \widetilde{u}_j \frac{\partial \widetilde{u}_i}{\partial x_j} \right)
$$

$$
= -\frac{\partial \widetilde{P}}{\partial x_i} + \frac{\partial}{\partial x_j} \left(2\overline{\mu_f \theta_f} \widetilde{S}_{ij} \right) - \frac{\partial q_{ij}^{r,vol}}{\partial x_j} + \overline{\rho_f \theta_f} g_i + F_{i,p \to f}
$$

$$
(2.2.23)
$$

Utilizing conservation of mass (Eq. 2.2.6), term (I) vanishes, and it gives

$$
\overline{\rho_f \theta_f} \left(\frac{\partial \widetilde{u}_i}{\partial t} + \widetilde{u}_j \frac{\partial \widetilde{u}_i}{\partial x_j} \right) = -\frac{\partial \widetilde{P}}{\partial x_i} + \frac{\partial}{\partial x_j} \left(2\overline{\mu_f \theta_f} \widetilde{S}_{ij} \right) - \frac{\partial q_{ij}^{r,vol}}{\partial x_j} + \overline{\rho_f \theta_f} g_i + F_{i,p \to f} \quad (2.2.24)
$$

The above equation can be rewritten using the product rule for the advective terms and rearranging to get

$$
\overline{\rho_f \theta_f} \left(\frac{\partial \widetilde{u}_i}{\partial t} + \frac{\partial \widetilde{u}_i \widetilde{u}_j}{\partial x_j} \right) = -\frac{\partial \widetilde{P}}{\partial x_i} + \frac{\partial}{\partial x_j} \left(2\overline{\mu_f \theta_f} \widetilde{S}_{ij} \right) - \frac{\partial q_{ij}^{r,vol}}{\partial x_j} + \overline{\rho_f \theta_f} g_i + F_{i,p \to f} + \overline{\rho_f \theta_f} \left(\widetilde{u}_i \frac{\partial \widetilde{u}_j}{\partial x_j} \right)
$$

$$
(2.2.25)
$$

To find the forcing terms arising from the volumetric displacement effects, Eq. 2.2.25 is compared to the standard two-way coupling equations for an incompress-

ible fluid with an additional momentum source term, $S_{v,mom}$, given as

$$\overline{\rho_f} \left(\frac{\partial \widetilde{u}_i}{\partial t} + \frac{\partial \widetilde{u}_i \widetilde{u}_j}{\partial x_j} \right) = -\frac{\partial \widetilde{P}}{\partial x_i} + \frac{\partial}{\partial x_j} \left(2\overline{\mu_f} \widetilde{S}_{ij} \right) - \frac{\partial q_{ij}^{r,2w}}{\partial x_j} + \overline{\rho_f} g_i + F_{i,p \to f} + S_{v,mom}$$

(2.2.26)

Note that the advective terms in Eq. 2.2.26 and 2.2.25 are written in a conservative form, mainly because, for incompressible flows, the numerical approach uses this form for discrete approximations. The additional source term, $S_{v,mom}$, can be obtained by subtracting Eq. 2.2.26 from Eq. 2.2.25 as

$$S_{v,mom} = \underbrace{\overline{\rho_f \theta_p} \left(\frac{\partial \widetilde{u}_i}{\partial t} + \frac{\partial \widetilde{u}_i \widetilde{u}_j}{\partial x_j} \right)}_{(S_{v,mom})_1} - \underbrace{\frac{\partial}{\partial x_j} \left(2\overline{\mu_f \theta_p} \widetilde{S}_{ij} \right) - \frac{\partial}{\partial x_j} \left(2c_\mu \overline{\rho_f \theta_p} \Delta^2 |\widetilde{S}| \widetilde{S}_{ij} - \frac{2}{3} \overline{\rho_f \theta_p} q^2 \delta_{ij} \right)}_{(S_{v,mom})_2}$$

$$- \underbrace{\overline{\rho_f \theta_p} g}_{(S_{v,mom})_3} + \underbrace{\overline{\rho_f \theta_f} \left(\widetilde{u}_i \frac{\partial \widetilde{u}_j}{\partial x_j} \right)}_{(S_{v,mom})_4}$$

(2.2.27)

The net source includes the volumetric displacement effects of carrier phase, due to spatial and temporal volume fraction variations. The terms on the right-hand side of Eq. 2.2.27 can be interpreted as follows

$$(S_{v,mom})_1 = \text{unsteady and fluid inertial terms,} \tag{2.2.28a}$$

$$(S_{v,mom})_2 = \text{stresses due to volume fraction variation,} \tag{2.2.28b}$$

$$(S_{v,mom})_3 = \text{hydrostatic buoyancy term,} \tag{2.2.28c}$$

$$(S_{v,mom})_4 = \text{local fluid divergence term.} \tag{2.2.28d}$$

Likewise, a continuity source term, $S_{v,cont}$, due to the volumetric displacement effects can also be derived by expanding the volume-averaged continuity equation

(Eq. 2.2.6) and rewriting it in a typical form of two-way coupled formulations as

$$\frac{\partial \widetilde{u}_j}{\partial x_j} = S_{v,cont} \qquad (2.2.29)$$

where,

$$S_{v,cont} = \frac{-1}{\rho_f \theta_f} \left(\frac{\partial}{\partial t} \left(\overline{\rho_f \theta_f} \right) + \widetilde{u}_j \frac{\partial}{\partial x_j} \left(\overline{\rho_f \theta_f} \right) \right) = \frac{-1}{\rho_f \theta_f} \frac{D}{Dt} \left(\overline{\rho_f \theta_f} \right) \qquad (2.2.30)$$

This shows that the spatio-temporal variations in the volume fraction of carrier phase generate a source term in the continuity equation as well which is called velocity divergence effect in line with Ferrante & Elghobashi (2004, 2005). For standard two-way coupled incompressible flows wherein θ_f=1, this source term is zero. However, in the volumetric two-way coupled formulation, this non-zero source term could potentially alter the flow field. These extra source terms, namely, (i) volumetric displacement forces and (ii) velocity divergence effect constitute the volumetric displacement effects of the carrier phase due to the presence and motion of particles.

2.2.5 Numerical method

Details on the numerical method employed in this study can be found in Finn *et al.* (2011); Shams *et al.* (2011), thus only a brief description is given here. The variable density zero-Mach number equations presented above are solved using a pressure-based, second-order, fractional time stepping scheme on a collocated grid arrangement. In this scheme, the velocity, pressure and volume fraction of the carrier phase are stored at the centroid of the control volumes. The Lagrangian particle equations are advanced first using a simple forward Euler approximation with subcycling within each flow time step (Shams *et al.*, 2011) to accurately account for the particle time scales relative to the fluid time scale. The volume fraction for both phases are then computed at the cell centres knowing the particle

locations. Given the volume fraction variations, the eddy viscosity, μ_t, is modified based on these variations through $\overline{\rho_f \theta_f}$ in order to account for their effects even in the subgrid scales (Eq. 2.2.10). In addition, point-particle forces are calculated and projected back to the cells in which particles are located. Knowing the volume fraction of each cell as well as particle reaction forces, the cell-centred velocities, $\overline{\rho_f \theta_f} \widetilde{u}_i$, are advanced by solving the momentum equation as a predictor step. The predicted velocities are interpolated to the faces and then projected to satisfy the continuity constraint. Projection yields the pressure potential at the cell centres, and its gradient is used to correct the cell and face-normal velocities.

2.3 Results

The numerical scheme employed in this study has been extensively applied to and validated for different flows and applications (Shams *et al.*, 2011; Finn *et al.*, 2011; Cihonski *et al.*, 2013; Finn *et al.*, 2016; Pakseresht & Apte, 2017; Pakseresht *et al.*, 2017; He *et al.*, 2018; Pakseresht & Apte, 2018, 2019*a*). In addition, the accuracy and robustness of the method is first investigated on a turbulent round jet flow laden with a dilute regime of inertial solid particles injected at the jet inlet ($[\overline{\theta_p}]_{inlet}$=0.047%) as illustrated in Fig. 2.3. Then, to investigate the volumetric displacement effects of the carrier phase due to presence and motion of particles in different suspensions, denser particulate jet cases with respective inlet solid volume loading of 4.7% up to 37.6% are studied. Influence of Stokes number (particle relaxation time) on the volumetric displacement effects is finally investigated in the densest suspension ($[\overline{\theta_p}]_{inlet}$=37.6%) with Stokes numbers of 11.6 down to 0.038. The studied cases and the corresponding flow parameters are listed in Tab. 2.2.

2.3.1 Numerical simulation setup

As provided in Tab. 2.2, cases B-D are similar to case A except with higher inlet volume loading in order to study and investigate the volumetric displacement effects at different loadings. Case C1 is similar to C; however, in the former neither
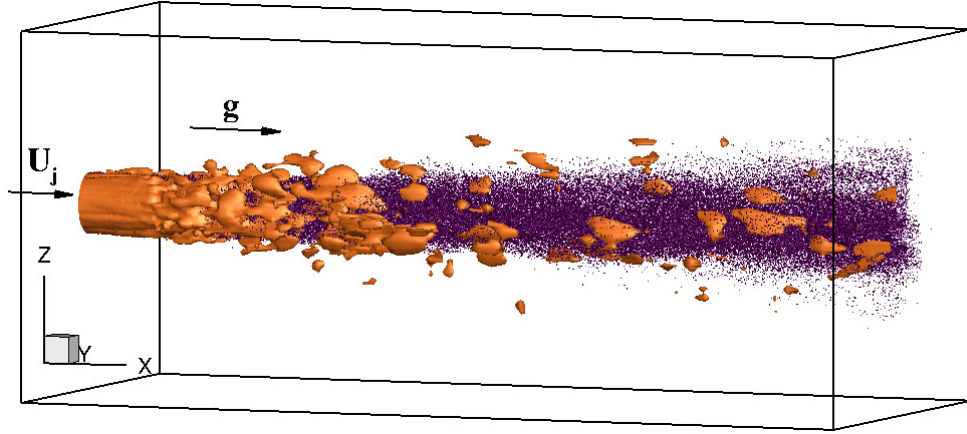
Figure 2.3: Schematic of particle-laden turbulent jet. Shown are vorticity magnitude and particle distribution with exaggerating in particle size for sake of clarity.

momentum exchange point-particle force nor inter-particle collision is included in order to isolate the effects of spatio-temporal variations in the carrier phase. Influence of Stokes number on the volumetric displacement effects is studied through cases D to F wherein all flow parameters are identical to those in case D, yet density ratio is varied to achieve different Stokes numbers. An experimental data by Mostafa *et al.* (1989) is available for case A; however, to our best of knowledge, for higher loadings no data exist. Thus, for cases B-F in order to investigate the volumetric displacement effects, only numerical results preformed with and without accounting for the spatio-temporal variations in the fluid volume fraction (standard versus volumetric two-way coupling) are compared together.

Spherical particles of diameter 105 micron are injected at the nozzle exit based on different volume loadings and different density ratios (or specific gravity, $S.G.=\rho_p/\rho_f$) per each case. Reynolds number of clear jet denoted by $Re_j=\rho_f U_j d_j/\mu_f=5712$ is defined based on the clear jet bulk velocity, $U_j=3.546m/s$, nozzle diameter, $d_j=0.0253m$, and the carrier phase properties for air, $\rho_f=1.178kg/m^3$ and $\mu_f = 1.8502\times10^{-5}kg/(m.s)$ corresponding to the experimental work of Mostafa *et al.* (1989). Total number of particles, $N_{p,inlet}$, required for injecting into the domain

per each flow time step, Δt_f, is calculated based on the given inlet volume loading, $[\overline{\theta_p}]_{inlet}$, particle's diameter, d_p, nozzle diameter, d_j, and jet bulk velocity as

$$N_{p,inlet} = \frac{6[\overline{\theta_p}]_{inlet}d_j{}^2 U_j \Delta t_f}{4d_p{}^3} \tag{2.3.1}$$

Tracking Lagrangian particles individually results in large number of particles ($\sim$ 13-100 million) in dense cases. To reduce the number of Lagrangian trajectories used, a discrete-parcel-model is commonly employed (O'Rourke & Bracco, 1980; O'Rourke, 1985). A parcel or computational particle represents a group of identical particles, N_{par}, with similar characteristics (diameter, velocity). For cases B-F, 40 particles form a parcel. The total number of particles/parcels in the domain, $N_{p,tot}$, interacting with the carrier phase is tabulated in Tab. 2.2. It is crucial to mention that for cases with parcel employed, collision takes place between parcels and the corresponding collision parameters are modified based on the total number of particles in each parcel (N_{par}). Accordingly, the mass or volume of each parcel is N_{par} times the particle mass or volume. In addition, effective diameter of parcels is obtained as $d_{parc}=d_{part}N_{par}^{1/3}$.

A Cartesian structured grid is utilized for solving fluid flow in a rectangular computational domain. Convective outflow boundary condition is applied at the outlet while slip boundary condition is enforced at the other sides of the domain except at the nozzle exit (inlet). Inflow data over several flow through times is generated by a periodic turbulent pipe flow with the same clear jet Reynolds number and read at each flow time step to specify the carrier phase velocity components at the inlet. In all cases, solid particles are injected at the nozzle surface into the already statistically stable turbulent clear round jet with prescribed mean and r.m.s. velocities measured at $x/d_j=0.04$ corresponding to the experiment of case A. It is well recognized that the hyperbolic characteristic of the convective outlet boundary condition may reflect error toward upstream of the flow if the computational domain is not long enough in the stream-wise direction (Dai *et al.*, 1994). Therefore, in order to overcome this error, a long enough computational domain with size of $14d_j \times 6d_j \times 6d_j$ in the directions of x, y and z, respectively is

Case	$d_p(\mu m)$	Re_j	S.G.	St	$[\overline{\theta_p}]_{inlet}$	N_{par}	$N_{p,tot}$	Inter-particle collision	Coupling type
A	105	5712	2122.24	11.6	0.047(%)	1	0.15×10^6	No	S2W and V2W
B	105	5712	2122.24	11.6	4.7(%)	40	0.34×10^6	Yes	S2W and V2W
C	105	5712	2122.24	11.6	18.8(%)	40	1.3×10^6	Yes	S2W and V2W
D	105	5712	2122.24	11.6	37.6(%)	40	2.56×10^6	Yes	S2W and V2W
E	105	5712	700	3.83	37.6(%)	40	2.56×10^6	Yes	S2W and V2W
F	105	5712	7	0.0383	37.6(%)	40	2.56×10^6	Yes	S2W and V2W
C1	105	5712	2122.24	11.6	18.8(%)	40	1.3×10^6	No	S1W and V1W

Table 2.2: Flow parameters for different particle-laden turbulent jet cases.

employed. A grid resolution of $100{\times}140{\times}140$ in x, y and z directions, respectively was found to be sufficient to accurately capture the effect of the large scales of motion as gauged by the flow statistics. Non-uniform grid spacing was chosen for the stream-wise direction, x, with minimum grid spacing of $\Delta x_{min}{=}455\mu m$ at the inlet. To capture the shear layer of the jet, a uniform and relatively fine resolution was used in y and z directions up to $3.5r_j$ from center of the jet with grid spacing of $\Delta y_{min}{=}\Delta z_{min}{=}703\mu m$ while stretching resolution was used further away, $r{>}3.5r_j$. The grid resolution satisfies the so-called assumption of point-particle approach where particles/parcels are to be subgrid, i.e., their size must be smaller than the smallest resolved length scale, $d_p{<}\Delta$. For the cases with parcels, the volume of all particles in a parcel is also less than the grid volume. Collision parameters are all identical among cases B-D as they have similar material properties. However, for cases E and F different stiffness coefficients are employed based on their densities which are explained later.

It should be noted that the Reynolds number in the particulate cases could vary as the bulk velocity of the laden jet gets influenced by particles as shown later. Although one may calculate it based on the modified bulk velocity, here we only tabulate it based on the clear jet to ensure that the flow into which particles are injected is identical among all cases. Throughout the paper, all numerical results at each nozzle distance are obtained based on the azimuthal averaging in space (y and z directions) as well as time averaging.

2.3.2 Dilute particle-laden turbulent jet

Case A is performed as a validation study for the numerical scheme presented above and serves as a baseline case for further investigations on the volumetric displacement effects. For this case, the results of standard and volumetric two-way couplings are compared with the corresponding experiment of Mostafa *et al.* (1989). Figure 2.4 shows the comparison on the mean velocity of the carrier as well as dispersed phases of case A at different nozzle distances. Stream-wise mean velocity of the carrier and dispersed phases is normalized by bulk velocity of the clear jet, U_j, and the local centreline velocity of the particle laden jet at each nozzle distance, U_c, respectively. A good agreement between numerical results and the corresponding experiment is achieved on the mean velocity of both phases validating our numerical model in simulating the particle-laden jet flows. As illustrated, the developing $(x/d_j{<}6)$ and self-similar $(x/d_j{>}6)$ regions of the jet are clearly noticeable. Decay and spread of the jet are well captured. As depicted, prediction of the volumetric two-way coupling matches the results of standard two-way coupling. This is expected due to the dilute loading in this case (0.047%) and even inter-particle collision is negligible. Therefore, the spatio-temporal variations in the fluid volume fraction and consequently the volumetric displacement effects are negligible in this case. Similar observation was also reported by Vreman *et al.* (2004) wherein they found insignificant difference between the results of these two couplings for a turbulent channel flow laden with average volume loading of $\overline{\theta_p}{=}0.013$ (i.e., 1.3%).

2.3.3 Influence of volume loading

In this part, cases B-D are computed to investigate the volumetric displacement effects in denser regimes. According to the classification map by Elghobashi (2006) (Fig. 2.2), the inter-particle collision is crucial for these cases ($St{=}11.6$ and $\overline{\theta_p}{\geq}10^{-3}$). Accordingly, both standard and volumetric two-way couplings include the inter-particle collisions. Figure 2.5 depicts the radial profile of carrier phase
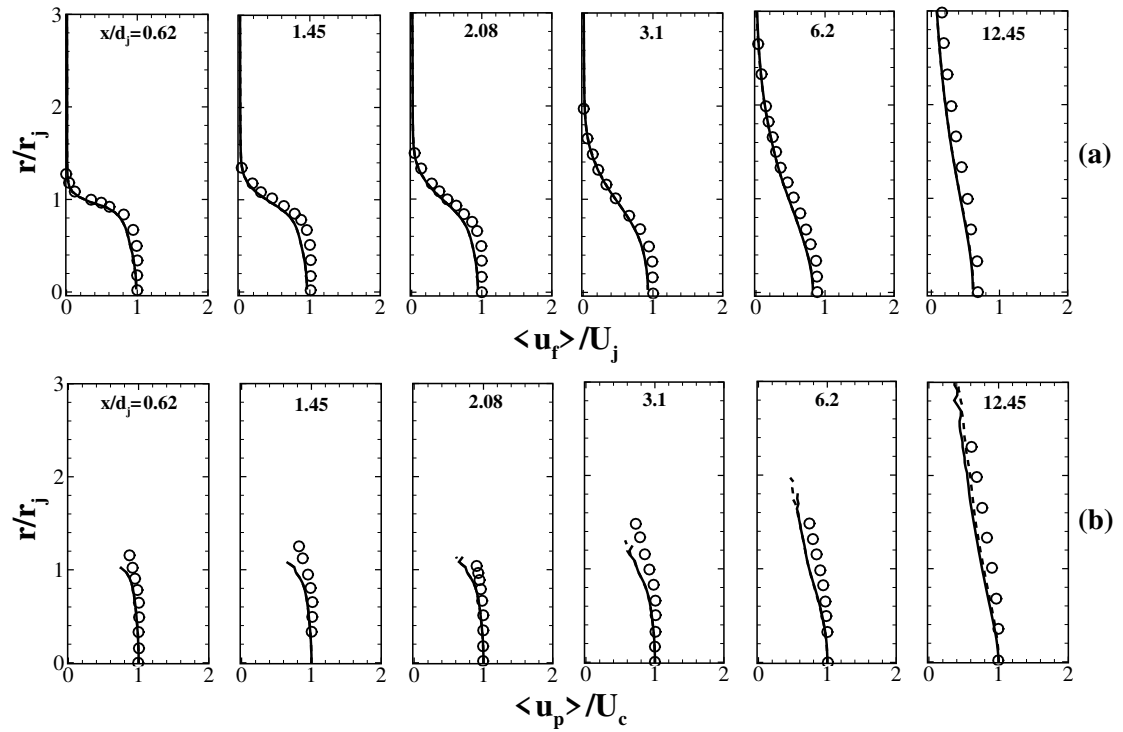
Figure 2.4: Radial profile of normalized stream-wise mean velocity for the carrier phase (a) and dispersed phase (b) corresponding to case A. Volumetric two-way coupling (solid); standard two-way coupling (dashed); Experiment (○) by Mostafa *et al.* (1989).

mean velocity predicted by both couplings normalized by the bulk velocity of the clear jet, U_j. For case B as shown in Fig. 2.5(a), a marginal increase exists on the centreline (r/r_j=0) mean velocity of the volumetric two-way coupling prediction at x/d_j=0.04. For the same nozzle distance, the difference between these two formulations becomes more pronounced and remarkable as particle loading increases as shown in Fig. 2.5(b) and 2.5(c) for cases C and D, respectively. This increase in mean velocity of the carrier phase is attributed to the volumetric displacement effects. It is worth mentioning that despite this increase in the near field of jet (x/d_j<0.62), the volumetric displacement effects decrease with nozzle distance in all dense cases (B-D) resulting in nearly similar predictions between two formulations. The decrease in these effects further downstream is conjectured to be due to the particle dispersion as well as the more enhanced point-particle reaction forces as explained in section 2.3.3.

Similar observations are obtained by looking at the r.m.s. velocity of the carrier phase in the stream-wise direction. Figure 2.6 shows the normalized carrier phase turbulence intensity obtained by these two couplings. In line with mean velocity, slight difference in r.m.s. velocity between these two couplings is observed for case B (Fig. 2.6(a)) while it becomes more significant and noticeable for cases C and D as depicted in Fig. 2.6(b) and 2.6(c), respectively. Moreover, this difference decreases with nozzle distance similar to the mean velocity results. The relative increase in the results of volumetric coupling respect to the standard coupling is plotted in Fig. 2.7 for both mean and r.m.s. velocities. A 28% and 160% increase in the volumetric coupling prediction of centreline mean and r.m.s. velocities, respectively, is observed for case D at x/d_j=0.04. As illustrated, the dynamics of the flow is more remarkably affected by the volumetric displacement effects than the mean flow.

Mechanisms involved in volumetric coupling formulation

In this part, the mechanisms behind increasing and decreasing the volumetric displacement effects in the volumetric coupling formulation are discussed in detail. In
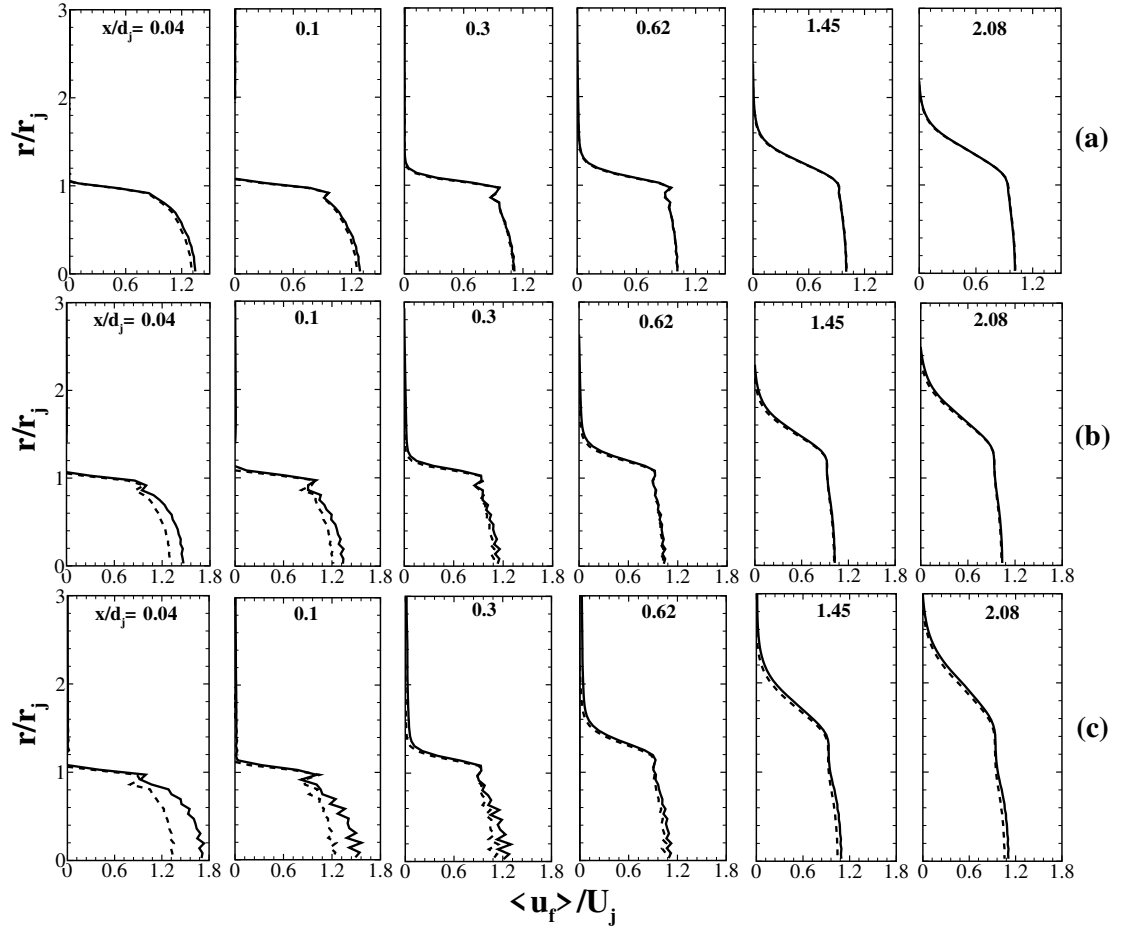
Figure 2.5: Radial profile of normalized stream-wise mean velocity of the carrier phase for cases B-D shown in (a)-(c) respectively. Volumetric two-way coupling (solid); standard two-way coupling (dashed).
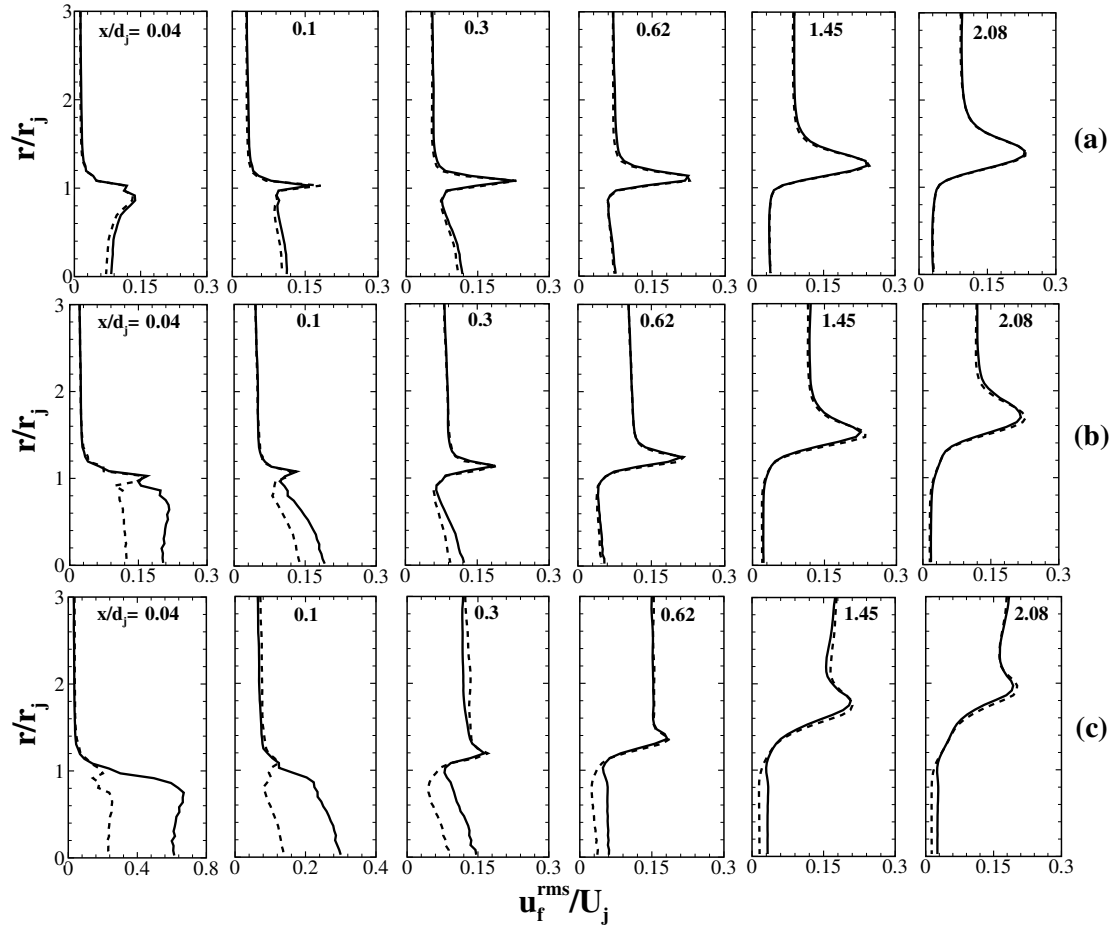
Figure 2.6: Radial profile of normalized stream-wise r.m.s. velocity of the carrier phase for cases B-D shown in (a)-(c) respectively. Volumetric two-way coupling (solid); standard two-way coupling (dashed).
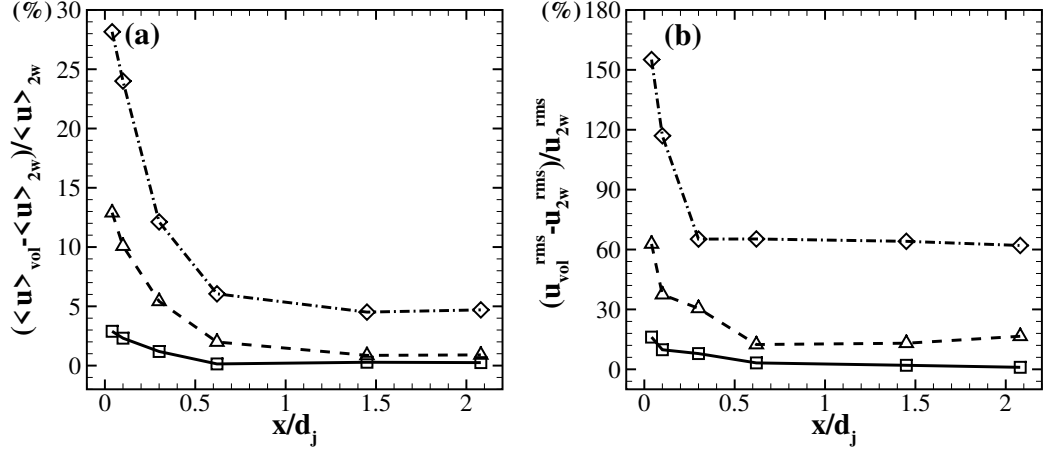
Figure 2.7: Relative increase in the volumetric two-way coupling prediction of the centreline mean (a) r.m.s. (b) velocities of cases B-D. Case B (solid); Case C (dashed); Case D (dash dot).

this formulation, the carrier phase gets influenced by the dispersed phase not only through the momentum exchange point-particle forces, $F_{i,p \to f}$, but also through the spatio-temporal variations in the volume fraction of the carrier phase which the latter generates source terms in both continuity and momentum equations. On the one hand, Ferrante & Elghobashi (2004) concluded that the accurate prediction of the drag reduction in the microbubble-laden turbulent boundary layer over a flat plate was due to the results of velocity divergence effect, the continuity source term ($S_{v,cont}$). On the other hand, Cihonski *et al.* (2013) showed that the accurate prediction of volumetric coupling for lower-than-fluid density bubbles was solely due to volumetric displacement forces, the momentum source term induced by this formulation ($S_{v,mom}$). The effects of these source terms are investigated in detail for the densest case, D, wherein a remarkable difference between the standard and volumetric couplings exists.

As shown in Fig. 2.8, the radial profile of velocity divergence effect for case D at different nozzle distances is plotted for both standard and volumetric couplings. As depicted, volumetric coupling generates a non-zero divergence of velocity due
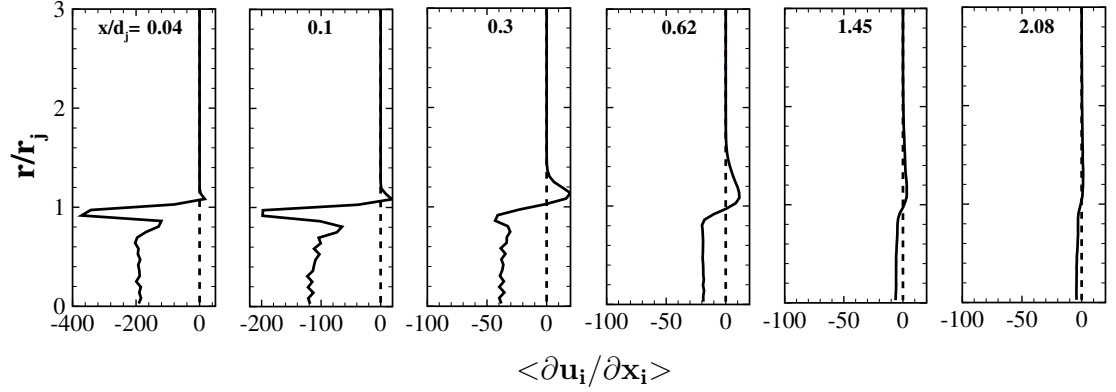
Figure 2.8: Radial profile of time-averaged divergence of the carrier phase velocity for case D based on prediction of volumetric two-way coupling (solid) compared to the standard two-way coupling (dashed).

to the variations in the volume fraction of the fluid. This continuity source term in the volumetric coupling formulation increases the pressure and velocity of the carrier phase in the region of high void fraction (i.e., volume fraction of the dispersed phase) to satisfy the conservation of mass. That is speculated to be the dominant mechanism in increasing the velocity in this formulation. The deviation of this term from the standard two-way coupling, however, decreases further downstream owing to the jet spread and dispersion of particles which in turn reduce the local volume fraction of particles. This decreases the velocity divergence effects downstream which consequently weakens the volumetric displacement effects on the flow. Figure 2.9 depicts the radial distribution of solid volume fraction predicted by both couplings. Different dispersion between these two couplings is observed. As shown, particles are more dispersed in the volumetric coupling compared to the standard coupling. That is conjectured due to the volumetric displacement effects which displace more particles from core region of the jet owing to the higher velocity prediction of this formulation.

The effect of volumetric coupling induced momentum source term ($S_{v,mom}$) on the flow is studied by evaluating its magnitude compared to the point-particle
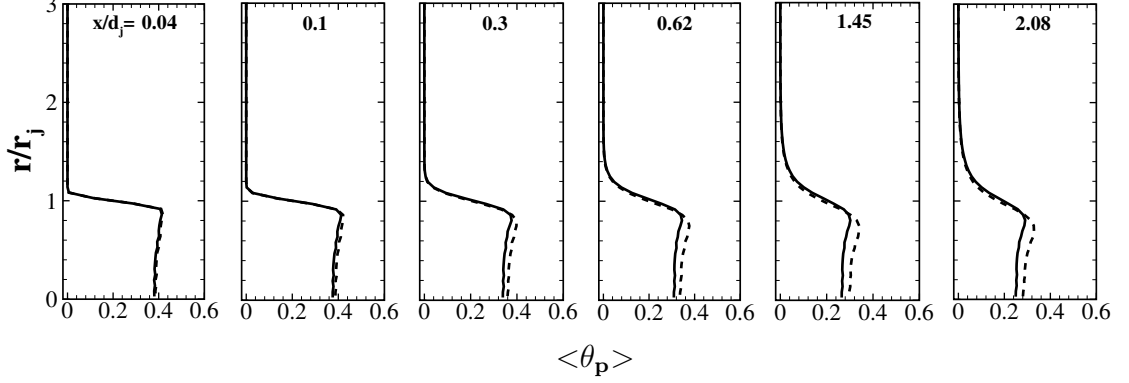
Figure 2.9: Radial profile of time-averaged solid volume fraction along the jet for case D based on prediction of volumetric two-way coupling (solid) compared to the standard two-way coupling (dashed).

forces $(F_{p \to f})$. Figure 2.10 depicts a comparison on the radial profile of these forces in the volumetric two-way coupling prediction of case D. The point-particle feedback force of the corresponding standard two-way coupling prediction, $F_{p \to f, 2w}$, for case D is also plotted as a reference. Forces on this plot are normalized by the stream-wise momentum of the clear jet, $\rho_f A_j U_j^2$. As illustrated, contribution of $S_{v,mom}$ is quite insignificant compared to its counterpart point-particle force, $F_{p \to f, vol}$. Therefore, higher velocity in the regions with high void fraction is solely attributed to the continuity source term. The point-particle force predicted in the volumetric coupling $(F_{p \to f, vol})$ is much higher than that of the standard coupling $(F_{p \to f, 2w})$. This is caused by the higher velocity prediction in the volumetric coupling formulation which increases the point-particle forces back to the flow. This could potentially decelerate the carrier phase in the downstream region of this formulation more than that of the standard two-way coupling. As a result, beside jet spread and particle dispersion, another opposing mechanism in volumetric displacement effects further downstream could be the higher point-particle forces predicted in the volumetric coupling formulation. However, the latter is conjectured to be less significant as the relative magnitude of the point-particle forces

compared to the jet momentum is still quite insignificant. The interaction between these opposing mechanisms and the effect of the continuity source term may be the reason for small oscillations in the near-field results of the mean velocity, particularly for the densest case (Fig. 2.5(c)). Moreover, these oscillations might be attributed to the computation of $(D\overline{\rho_f \theta_f}/Dt)$ which might not be smooth (Fig. 2.8) due to the sharp variations in the gradients of the volume fraction.
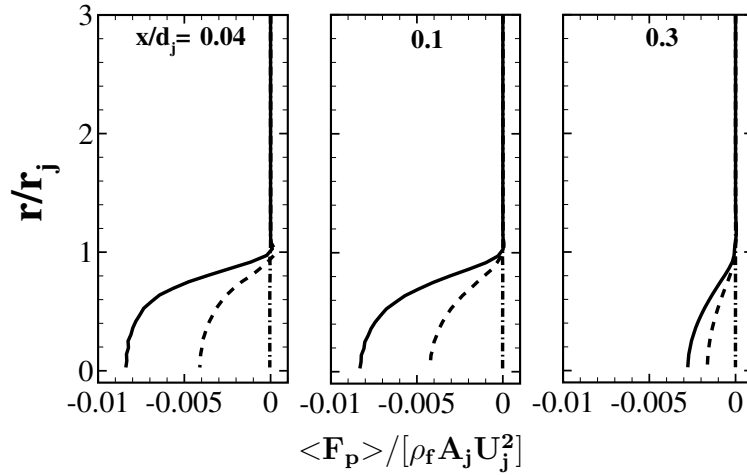
Figure 2.10: Radial profile of the time-averaged stream-wise forces caused by presence of particles normalized by the clear jet momentum. Normalized volumetric two-way coupling point-particle force, $<F_{p\to f,vol}>/[\rho_f A_j U_j^2]$ (solid); normalized standard two-way coupling point-particle force, $<F_{p\to f,2w}>/[\rho_f A_j U_j^2]$ (dashed); volumetric displacement force, $<S_{v,mom}>/[\rho_f A_j U_j^2]$ (dash dot).

The most dominant point-particle forces, viscous drag and pressure-gradient, predicted by the two couplings for case D at x/d_j=0.04 are plotted in Fig. 2.11. Buoyancy force, $m_p g(1-\rho_f/\rho_p)$, is used for normalizing the forces. As shown, both viscous drag and pressure-gradient forces predicted by the volumetric coupling are greater than those of the standard coupling. This is again due to the modified continuity and hence the pressure Poisson equation. The continuity source term increases both pressure and velocity in the region of high void fraction which sequentially intensifies the viscous drag and pressure-gradient forces acting on par-

ticles. As explained in section 2.2.2, the drag force accounts for the local volume fraction of dispersed phase. It is important to mention that even in the standard two-way coupling, wherein the volume fraction variations are not accounted for in continuity and momentum equations, the drag force is still modified by these variations. This is performed to obtain identical force wise conditions between the two couplings.
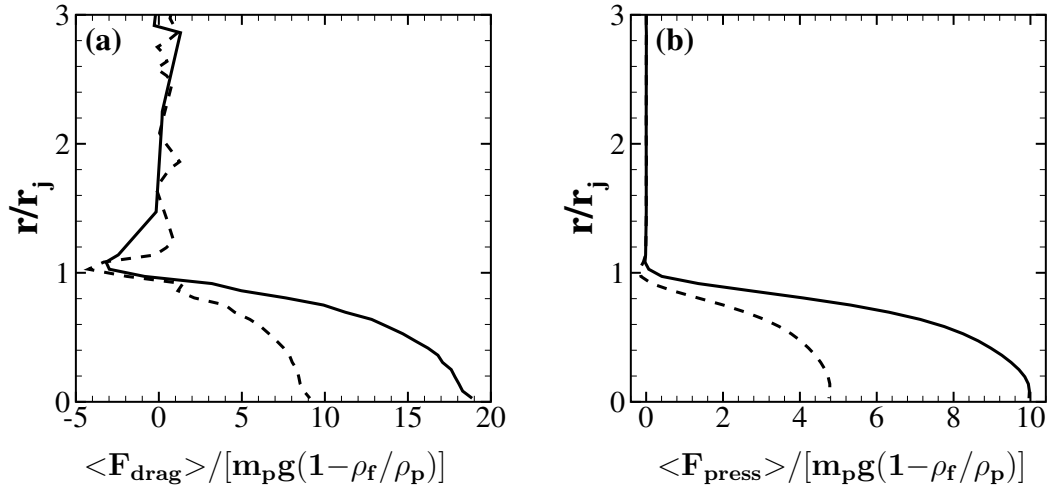
Figure 2.11: Radial profile of the most dominant time-averaged point-particle forces in case D at x/d_j=0.04. (a) viscous drag closure; (b) pressure-gradient closure. Volumetric two-way coupling prediction (solid); standard two-way coupling prediction (dashed). Buoyancy, $m_p g(1-\rho_f/\rho_p)$, is used for normalizing the forces.

Further quantification of the velocity divergence effect in volumetric coupling formulation is achieved by *masking* the point-particle forces as well as inter-particle collisions. Excluding these two opposing mechanisms would reduce the dispersion of particles, keep the local volume fractions nearly unchanged along the jet and isolate the volumetric displacement effects. Note that, unlike the standard one-way coupling approach, in the volumetric coupling formulation even in the absence of point-particle forces, flow could still be altered through the variations in the fluid

volume fraction. Case C1 (Tab. 2.2) compares volumetric and standard one-way couplings. Figure 2.12 depicts the respective mean and r.m.s velocities of the carrier phase for case C1 based on the two different couplings. As shown, a noticeable increase in the mean velocity prediction of volumetric formulation is observed all along the jet compared to the standard one-way coupling. Unlike case C (Fig. 2.5(b)) where only noticeable difference was observed up to x/d_j=0.3, here in case C1, the difference between the two couplings remains unchanged even further downstream. The difference between these two couplings would even become more pronounced and significant for denser loadings. Regarding the dynamics of flow, an increase in the r.m.s. velocity of the volumetric one-way coupling prediction is observed only at x/d_j=0.04 while further downstream both formulations predict similar results. As a result, for cases studied in this part with Stokes number of St=11.6, one can conclude that the velocity divergence effect caused by modified continuity equation in the volumetric coupling formulation is the most dominant mechanism in driving volumetric displacement effects. This increases the velocity of the carrier phase in the regions of high void fraction. However, further downstream, due to the dispersion of particles and their reaction forces, the volumetric displacement effects decrease.

2.3.4 Influence of Stokes number

Three cases (D-F) with different Stokes numbers are examined accordingly while other flow parameters are kept identical. The different Stokes numbers are achieved by changing density of the dispersed phase and keeping other particle parameters constant. As listed in Tab. 2.2, Stokes number varies from 11.6 in case D to 0.0383 in case F. It is important to note that the Stokes number is defined based on turnover time of large eddy (τ_f=d_j/U_j); thus, these numbers would be greater if calculated based on the Kolmogorov time scale (η). In the preceding section, the stiffness coefficient for inter-particle collision was constant among the cases due to the similar density of particles. In this part, however, the coefficient must vary among the cases in order to take into account the density effect on the
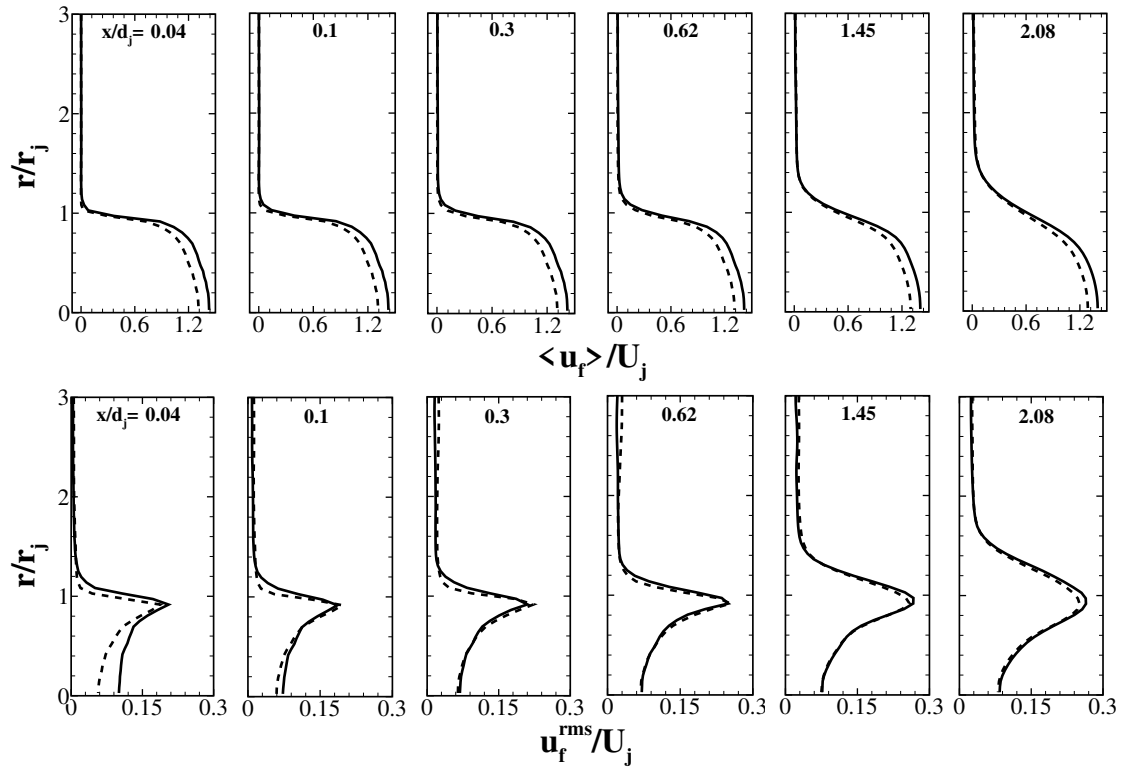
Figure 2.12: Radial profile of normalized stream-wise mean and r.m.s. velocities of the carrier phase for case C1. Volumetric one-way coupling (solid); standard one-way coupling (dashed).

inter-particles collisions. Therefore, a first order linear relationship for stiffness parameter between cases is chosen based on their density ratios. As an example, stiffness parameter for case F, k_F is set as $k_F = k_D \rho_F / \rho_D$ knowing the value for k_D and particle densities for cases F and D.

As Stokes number decreases, particles respond more quickly to the changes in the background flow, and tend to reach lower relative velocity as they move along the jet. Compared to the high Stokes number cases, this could decrease the viscous drag force as well as the effect of opposing point-particle forces in the volumetric displacement effects. In addition, reducing the Stokes number would change the local concentration as well as dispersion of particles among cases. Particles with higher Stokes number may stay longer in the core region of the jet keeping higher void fraction while low Stokes number particles behave more likely as fluid tracers and have less dispersion.

Figure 2.13 shows mean and r.m.s velocities of the carrier phase for case F (the lowest Stokes number) which can be compared with the results of case D (Fig. 2.5(c) and 2.6(c)). As plotted, the volumetric two-way coupling predicts higher mean velocity for case F similar to the observation of case D, although some distinctions between these two cases exist. On the one hand, very close to the nozzle ($x/d_j < 0.3$) the difference between these two couplings for case F is less than that of case D. This can be attributed to the preferential concentration as well as quick response time of low Stokes number particles in case F. Particles in case F tend to preferentially accumulate in the shear layer of the jet. Due to their quick response time, the particles are carried away by the fluid faster, resulting in less accumulation and smaller volume fraction in the core region as shown in Fig. 2.14. This decreases the volumetric displacement effects very close to the nozzle ($x/d_j < 0.3$) for case F compared to D. On the other hand, unlike case D, further downstream in case F ($0.62 < x/d_j < 2.08$), the difference between these two couplings is more noticeable and indeed remains nearly unchanged owing to less dispersion of low Stokes number particles as well as their smaller reaction forces.

The influence of Stokes number on the motion of dispersed phase predicted
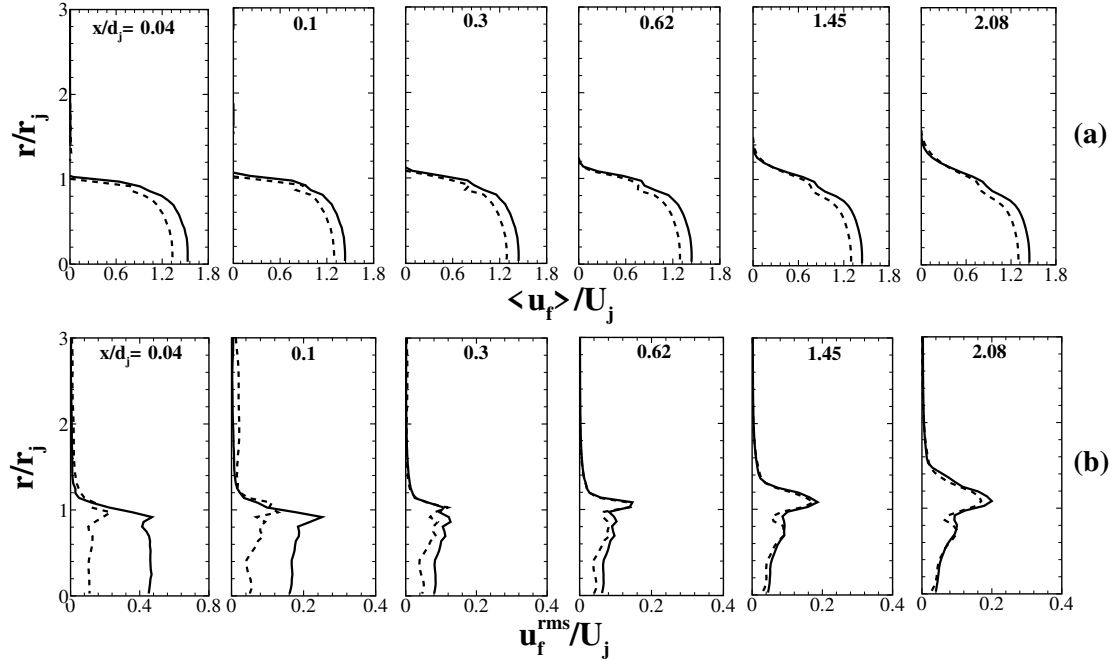
Figure 2.13: Radial profile of mean (a) and r.m.s. (b) velocities of the carrier phase normalized by the clear jet bulk velocity for case F. Volumetric two-way coupling (solid); standard two-way coupling (dashed).
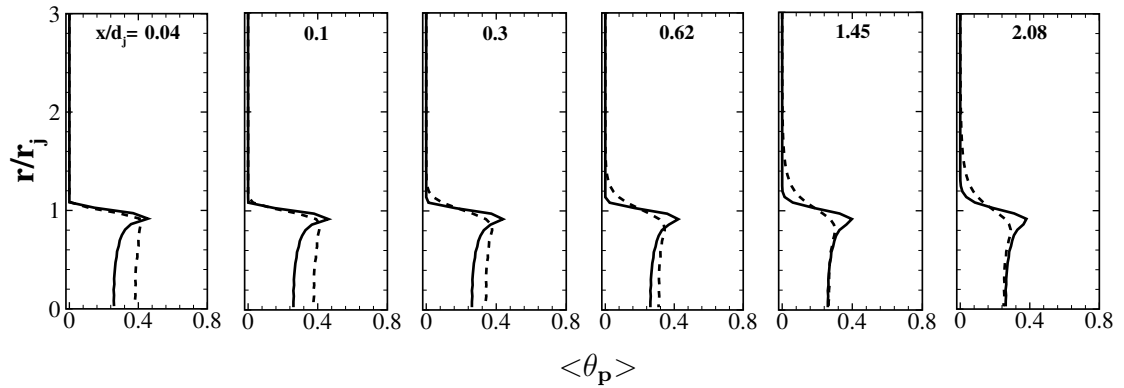
Figure 2.14: Radial profile of particle volume fraction for case F (solid) versus case D (dashed) at different nozzle distances.

by these two approaches is also investigated. Figures 2.15(a,b) depict the particle phase mean velocity for cases D and F, respectively, normalized by the clear jet bulk velocity. As shown, the high Stokes number particles in case D react slowly to the changes in the background flow and it takes them longer to get affected by the increased fluid velocity observed in the volumetric coupling formulation. In fact, very close to the nozzle both couplings predict nearly similar results; however, further downstream a 5% increase in the results of volumetric coupling on the motion of particles is observed. In contrast, as shown in Fig. 2.15(b), lower Stokes number particles in case F react more quickly to the changes in the background flow. In line with the results of the carrier phase for case F, the difference between these two approaches remains unchanged all along the jet with almost 11% increase relatively in the results of volumetric coupling. Figures 2.16(a,b) show the percentage increase in the results of volumetric coupling on the mean velocity of both phases for each case.

Further insight into the influence of Stokes number on the volumetric displacement effects is obtained by looking at the contribution of different momentum forces employed in the volumetric coupling formulation; point-particle forces ($F_{p \to f}$) and volumetric displacement forces ($S_{v,mom}$). Figure 2.17(a) shows the summation of these forces, F_{tot} at centreline of the jet for cases D and F predicted by the volumetric coupling. As shown, high Stokes number particles in case D exert greater forces back to the flow due to the higher relative velocity between phases which in turn push the flow stronger either backward ($x/d_j < 1.45$) or forward ($x/d_j > 1.45$). Although the magnitude of this force is relatively small compared to the jet momentum, it could be interpreted as a mechanism in reducing the fluid velocity further downstream in case D. In contrast, the corresponding force in case F is quite negligible. This allows the velocity divergence effect to increase the fluid mean velocity even further downstream in this case. In addition, as shown in Fig. 2.17(b), the ratio of point-particle forces and volumetric coupling induced momentum source term, $F_p/S_{v,mom}$, is on the order of 100 and 1 for cases D and F, respectively. It shows that for high inertial particles, one can neglect the
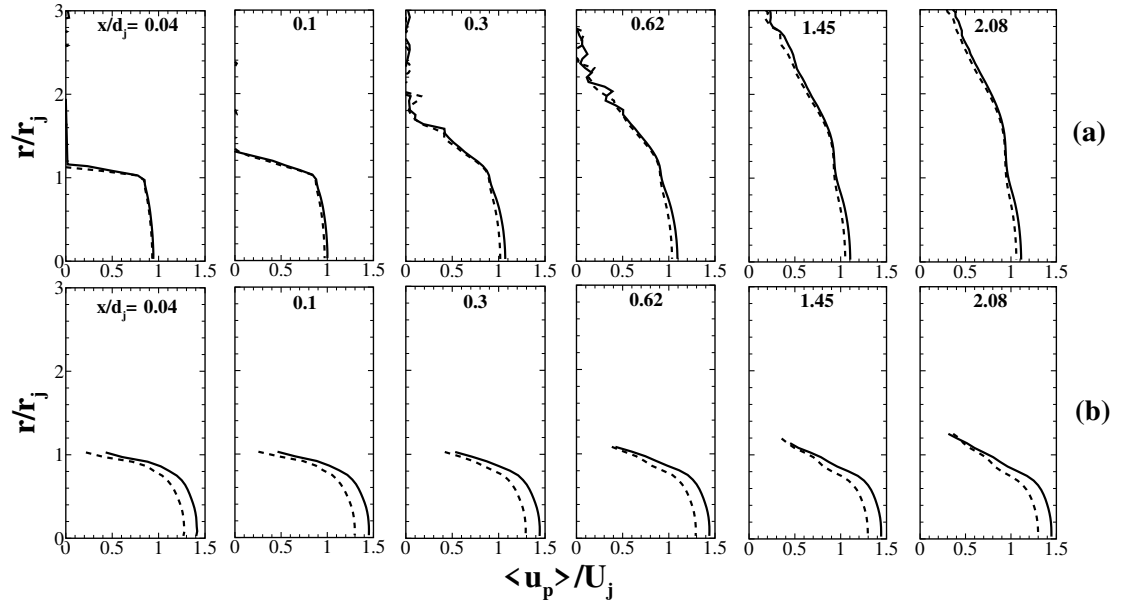
Figure 2.15: Radial profile of mean velocity of the dispersed phase normalized by the clear jet bulk velocity. (a) case D; (b) case F. Volumetric two-way coupling (solid); standard two-way coupling (dashed).
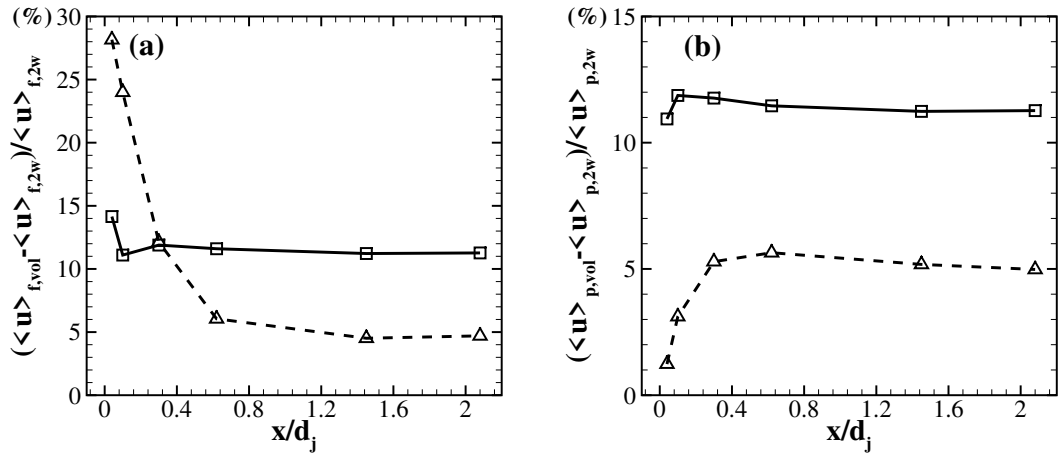
Figure 2.16: Relative increase in volumetric coupling prediction of (a) the fluid mean centreline velocity and (b) the particle mean centreline velocity for cases D and F. Case F (solid); Case D (dashed)

volumetric displacement forces while for low Stokes number particulate flows, this term is important (Cihonski *et al.*, 2013).
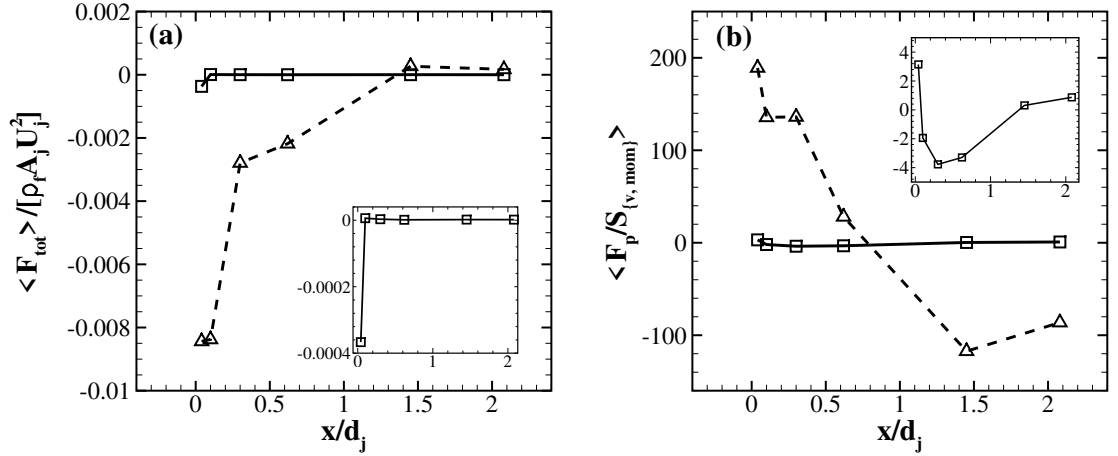
Figure 2.17: Time-averaged momentum forces in the volumetric coupling formulation due to presence of particles. (a) The summation of point-particle forces, $F_{p \to f}$, and volumetric displacement forces, $S_{v,mom}$, at the centreline of jet normalized by its momentum; (b) The ratio of point-particle and volumetric displacement forces at the centreline of jet. Case F (solid); Case D (dashed). Inset is the zoomed in version of the same plot to allow for a better displaying of variations in case F near the nozzle.

2.4 Conclusions

In this work, a large eddy simulation coupled with modified point-particle approach was performed to study a dense particle-laden turbulent jet flow. Two different approaches modelling the particle-turbulence interactions in dense regimes were studied: (i) standard two-way coupling; and (ii) volumetric two-way coupling. In the former, the effect of particles on the flow is modelled through momentum point-particle forces whereas in the latter, in addition to this force, the local variations in the volume fraction of the fluid phase are accounted for in both continuity

and momentum equations. This formulation gives rise to unique source terms in both continuity and momentum equations. Comparing these two formulations, the volumetric displacement effects of the carrier phase due to presence and motion of particles were identified. Investigations were performed through different cases by varying either the inlet volume loading of particles ($0.047{\leq}\theta_p{\leq}37.6\%$) or the particle Stokes number ($0.0383{\leq}St{\leq}11.6$) for each of which other flow parameters remained constant. It was found that the volumetric displacement effects are noticeable when the inlet volume loading is larger than 5%. Above this volume loading, the volumetric displacement effects increased both mean and r.m.s. velocities of the carrier phase with even more pronounced effects for higher loadings.

For the densest case with the highest Stokes number studied, 28 and 160% increase in the mean and r.m.s. velocities of the carrier phase, respectively, were observed at the nozzle exit due to displacement effects. The mechanism behind the velocity increase was found to be the continuity source term, $S_{v,cont}$, that appears in the modified continuity equation. These effects decreased further downstream of the nozzle owing to the radial dispersion of particles and jet spread which reduced the local volume fraction of the particles.

Lowering the Stokes number in the densest case revealed some significant differences on the volumetric displacement effects. Very close to the nozzle, these effects were found to be less pronounced for the lowest Stokes number case (St=0.038) compared to the highest (St=11.6). However, further downstream more remarkable effects were observed for St=0.038. In addition, the dispersed phase in the lowest Stokes number case was observed to be more affected by the volumetric displacement effects particularly in the downstream region. An increase of 11% in the downstream velocity of particles was observed compared to the corresponding 5% for the highest Stokes number case. These differences are attributed mainly to the preferential concentration and dispersion of particles as well as the particles response time. Close to the nozzle, the lowest Stokes number particles would react as fluid tracers and they tend to accumulate in the shear layer of the jet. In addition, due to their quick response time they were carried away by the fluid faster,

which in turn decreases the volume fraction as well as the volumetric displacement effects. On the other hand, further downstream, due to less dispersion of particles as well as their smaller reaction forces, the higher volume fraction in the core region of the jet remains and increases the volumetric displacement effects.

It was shown that the ratio of point-particle and volumetric displacement forces, $F_{p \to f}/S_{v,mom}$, ranged from 1 to 100 for the lowest and highest Stokes number cases, respectively. This emphasizes the importance of volumetric coupling induced momentum source term for low Stokes number particle-laden flows. However, for high Stokes number flows, this term could be negligible and the continuity source term, $S_{v,cont}$, is the only mechanism in dominantly driving the volumetric displacement effects.

As a result, we conclude that for modeling the particulate jets with inlet volume loading of 5% or greater, in addition to the standard two-way coupling approaches, the volumetric displacement effects of the carrier phase due to the motion and presence of particles should be included. Accordingly, we update the well-known classification map by Elghobashi (1991) on the particle-turbulence interactions if employed in EL approaches. A region identifying the necessity of volumetric displacement effects has been added to this map (Fig.2.2). Based on the observations of this work, we conjecture that similar results with more pronounced displacement effects would be achieved for atomizing sprays.

Chapter 3   A general velocity correction scheme for two-way coupled point-particle simulations

Pedram Pakseresht, Mahdi Esmaily and Sourabh V. Apte

Abstract

The accuracy of Euler-Lagrange point-particle models employed in particle-laden fluid flow simulations depends on accurate estimation of the particle force through closure models. Typical force closure models require computation of the slip velocity at the particle location, which in turn requires accurate estimation of the *undisturbed* fluid velocity. However, when the fluid and particle phases are two-way coupled, wherein the particle and fluid phases exchange momentum through equal and opposite reaction forces, the fluid velocity field is disturbed by the presence of the particle. Since the undisturbed fluid velocity is not readily available, a common practice is to use the *disturbed* velocity, without any correction, to compute the particle force. This can result in errors as much as 100% in predicting the particle dynamics. In this work, a general velocity correction scheme is developed that facilitates accurate estimation of the undisturbed fluid velocity in particle-laden fluid flows with and without no-slip walls. The model is generic and can handle particles of different size and density, arbitrary interpolation and distribution functions, anisotropic grids with large aspect ratios, and wall-bounded flows. The present correction scheme is motivated by the recent work of Esmaily & Horwitz (JCP, 2018) on unbounded particle-laden flows. Modifications necessary for wall-bounded flows are developed such that the undisturbed fluid velocity at any wall distance is accurately recovered, asymptotically approaching the unbounded scheme for particles far away from walls. A detailed series of verification tests were conducted on settling velocity of a particle in parallel and perpendicular motions to a no-slip wall. A range of flow parameters and grid configurations; involving anisotropic grids with aspect ratios typically encountered in particle-laden turbulent channel flows, were considered in detail. When the wall effects are accounted for, the present correction scheme reduces the errors in predicting the near-wall particle motion by one order of magnitude smaller values compared to the unbounded correction schemes.

3.1 Introduction

Particle-laden flows are widely encountered in biology, nature and industry. Stroke by embolic particles in brain arteries (Mukherjee *et al.*, 2016), motion of red blood cells and margination of platelets in vessels (Müller *et al.*, 2016), drug delivery, urban pollutant and settling in human respiratory system, spray combustion (Apte *et al.*, 2003), particle-based solar receivers (Pouransari & Mani, 2017), surgical site infection caused by dispersion of squames in the operating rooms (He *et al.*, 2018), sediment transport (Finn *et al.*, 2016); among others are examples of such flows. Understanding the underlying physics of such flows, making predictions without performing expensive experiments, and ultimately optimizing the current systems require accurate predictive modelling tools.

The point-particle (PP) approach (Maxey & Riley, 1983; Maxey *et al.*, 1997) has received much attention in simulating these flows due to its simplicity, affordability and partial accuracy. This approach was initially introduced for modeling dilute particle-laden flows with relatively small size particles that have negligible effects on the background flow. For such a "one-way" coupled flow (Elghobashi, 1991), imposing the no-slip boundary condition on the surface of particles is not needed as the perturbation generated at the particle scale is insignificant. The fluid phase is solved using an Eulerian framework while particles are treated as Lagrangian points in the flow and tracked following the Newton's second law of motion based on the available closures for the fluid forces acting on the particles. Such one-way coupled simulations are mostly used for particle tracking and clustering. Nevertheless, owing to its affordability, this Euler-Lagrange (EL) approach has also been applied to particulate flows with dense loading or those with relatively large size particles wherein the effect of particles on the background flow is inevitable (Squires & Eaton, 1990; Elghobashi & Truesdell, 1993). For such two-way coupled flows, the effect of particles on the carrier phase is modelled by applying the particle reaction force to the background flow through a momentum source term. Using such a simplified point force in modelling the inter-phase interactions, however, could result in some inaccuracies in capturing the experimental observa-

tions (Segura, 2004; Eaton, 2009; Pakseresht *et al.*, 2017) or analytical solutions (Pan & Banerjee, 1996) of particle-laden flows.

One source of inaccuracy is that, the fluid phase equations in this approach are solved for the entire flow field including the volumes occupied by the particles, and the mass displacement of the particles is not accounted for. Several works have shown the considerable effects of this displacement and have argued that this effect should be included in addition to the point-particle force (Ferrante & Elghobashi, 2004; Apte *et al.*, 2008; Cihonski *et al.*, 2013; Pakseresht & Apte, 2019*b*), in order to improve the predictions compared to the experimental observations. The other one, that is the focus of this work, is that the accuracy of PP in predicting the particle force can decay when the two phases are two-way coupled, owing to the disturbance created by the particle force on the background flow. Such a disturbance produces an error in the force calculations since the closure models often rely on the slip velocity computed based on the *undisturbed* fluid flow, which is not readily available in the two-way coupled simulations.

Few schemes have been recently developed as a substitute for the standard PP approach in order to improve the modeling of particle-laden flows. Pan & Banerjee (1996) were the first to develop a velocity-disturbance-model that couples two phases through the velocity field rather than the momentum exchange force. Their model is based upon the Stokes solution for the motion of a particle in a quiescent flow, for which the flow field generated around the particle is analytically known. Accordingly, to couple the two phases and capture the particle's effect on the flow, one could directly enforce this solution to the background flow. Unlike the standard PP approach, this velocity-disturbance-model eliminates any dependency to the undisturbed fluid velocity and results in more accurate inter-phase coupling. Despite its accuracy, it is limited to flows with particles in the Stokesian regime ($Re_p < O(0.1)$). Maxey & Patel (2001) introduced an alternative scheme that approximately satisfies the no-slip boundary condition at the particle surface, that is suitable for particle-laden flows with relatively large particle sizes. In this force-coupling model, the presence of particles on the flow is approximated by a

multipole expansion of a regularized steady Stokes solution. Despite its promising results for unbounded flows, for wall-bounded regimes it requires higher order terms, more than monopole and dipole, in order to accurately capture the wall lubrication effect (Lomholt *et al.*, 2002) which in turn adds more complexity to their formulation. In addition, similar to Pan & Banerjee (1996) scheme, the assumption of Stokesian regime for flow around the particles limits the application of their method to flows where $Re_p < O(0.1)$.

Recently, efforts have been made in order to improve the accuracy of the standard PP approach by retrieving the undisturbed fluid velocity from the available disturbed field. Gualtieri *et al.* (2015) regularized the PP approach for the unbounded flows by deriving analytical equations to remove the self-induced velocity disturbance created by the particles. Their approach requires considerable computational resources to resolve the stencil over which the particle force is distributed using a Gaussian filter function. Horwitz & Mani (2016, 2018) originated a method to obtain the undisturbed velocity based on the enhanced curvature in the disturbed velocity field for particle Reynolds numbers of $Re_p < 10.0$. A C-field library data was built using reverse engineering technique that should be added to the current EL-PP approaches for recovering the undisturbed velocity. Although their model showed excellent agreement in the predictions of particle settling velocity and decaying isotropic turbulence (Mehrabadi *et al.*, 2018), it is limited to (i) the isotropic computational grids, (ii) particle-laden flows with particles with the maximum size of the grid ($\Lambda = d_p/\Delta$) of O(1), where Δ is the grid size and d_p particle diameter, and (iii) the unbounded flows. Ireland & Desjardins (2017) derived an analytical expression for recovering the undisturbed velocity in unbounded flows based on the steady state Stokes solution that was derived as the solution of a feedback force distributed to the background flow using a Gaussian smoothening. Although their model accounts for the mass displacement of the particles, it is limited to unbounded flows with small Re_p.

In a generic approach, Esmaily & Horwitz (2018) originated a correction scheme in which each computational cell is treated as a solid object that is immersed

in the fluid. Each computational cell that is subjected to the two-way coupling force is dragged at a velocity that is identical to the disturbance created by the particle. In their physics-based model, the disturbance of each computational cell created by the particle is obtained by solving the Lagrangian motion of the cell concurrently with the equation of motion of the particle. Although their model was devised to handle (i) relatively large size particles ($\Lambda{>}1$), (ii) isotropic and anisotropic grids, (iii) flows with finite Re_p, and (iv) arbitrary interpolation and distribution functions, it is limited to unbounded flows. Balachandar *et al.* (2019) developed a model based on analytical and empirical equations that correct the PP approach for modelling particle-laden flows with a wide range of particle Reynolds number, $Re_p{<}200$. Following their scheme, analogous model was developed by Liu *et al.* (2019) for retrieving the undisturbed temperature in heated particle-laden flows. Although their velocity and temperature models account for the mass displacement of the particles (similar to Ireland & Desjardins (2017)) and are built for a wide range of particle Reynolds number and Peclet number, they are derived for unbounded flows only, and based on a specific filter function; namely Gaussian, that limits their applicability.

Nearly all available correction schemes have been originated and developed for the unbounded particle-laden flows. Due to the the wide range of wall-bounded applications, developing more general correction schemes that are applicable for flows near solid boundaries is necessary. Pakseresht *et al.* (2019) and Horwitz *et al.* (2019) underscored the need for such general correction schemes while Battista *et al.* (2019) extended their regularized PP scheme (Gualtieri *et al.*, 2015) for a turbulent particle-laden pipe flow. Unique modeling issues arise in wall-bounded particulate flows that need to be addressed in any correction scheme. First, particles near a wall, specially in a turbulent flow, are relatively bigger than the grid size normal to the wall and consequently disturb the flow strongly and anisotrpically. It has been observed that the disturbance created by a particle is proportional to the ratio of its volume to that of the cell (Esmaily & Horwitz, 2018), hence the disturbance of particles near the wall is expected to be strong. Second, the correction

scheme should be able to handle the anisotropic grid resolution typically encountered near the walls in turbulent particle-laden flows. Third, unlike unbounded flows, the disturbance created by a particle near the wall is conceptually asymmetric and should decay faster to the wall, in order to satisfy the no-slip boundary condition. These criteria necessitate the need for a general correction scheme that can capture any type of disturbance in presence or absence of the no-slip walls.

This paper aims to develop such a generic correction scheme that meets the criteria, mentioned above. Such a scheme enables accurate predictions of wall-bounded, particle-laden flows, and will potentially help provide insights into the underlying physics of such flows. In this regard, the correction scheme originated by Esmaily & Horwitz (2018) (hereinafter named as E&H) is generalized and extended to account for the wall effects on the disturbance field in the presence of no-slip boundary conditions. Additional adjustments are made due to the collocated grid arrangement used in this study. The generalized framework can be easily extended to complex arbitrary shaped, unstructured grids (Pakseresht *et al.*, 2012), as well as walls with curvature and surface roughness. The newly developed scheme is general and could be implemented and applied to all types of flows with different grid resolutions, arbitrary interpolation functions and varying particle to grid size. The new approach will be tested on canonical cases for which analytical solutions are available and illustrates the need for such a general correction scheme. How much the disturbance created by particle in the presence of no-slip wall gets deviated from its unbounded counterpart and how this affects the particle's motion and the inter-phase coupling in the presence of no-slip wall are the questions that we address in this paper.

The paper is organized as follows. We describe our correction scheme in section 3.2. Correction factors due to the presence of a no-slip wall are introduced and the model is expanded to a wide range of grid resolutions typically encountered in wall-bounded turbulent particle-laden flows. Section 3.3 validates the model on predicting the velocity of a single particle settling in an unbounded domain. Then, the new model will be tested for velocity of a single particle moving parallel to the

wall at various wall-normal distances. In addition, the perpendicular motion of a particle toward the wall is examined to assess the model for disturbances created in the wall-normal direction. In order to quantify the accuracy of the model for a wide range of applications, different flow parameters and computational grids are studied. Isotropic and anisotropic grid resolutions are investigated to demonstrate the capability of the model for different configurations. In order to illustrate the importance and the need for the present approach, the results are compared with the unbounded version of the present model, wherein wall effects are ignored, as well as the uncorrected scheme. Section 3.4 concludes the paper with final remarks and summary of the work.

3.2   A general correction scheme

In this section, we first introduce the main underlying issue in the two-way coupled point-particle (PP) approach, then present a general methodology to resolve the issue in the presence and absence of the no-slip walls. In the standard PP approach, particles are assumed spherical and subgrid (smaller than the grid resolution), and tracked in a Lagrangian framework using the second law of Newton as,

$$m_p \frac{du_p^{(i)}}{dt} = F^{(i)} + m_p g^{(i)}, \tag{3.2.1}$$

wherein the particle velocity in direction i, $u_p^{(i)}$, with mass of m_p is obtained using the total force of $F^{(i)}$ acting over the particle as well as its weight, $m_p g^{(i)}$. Depending upon the regime under consideration, different forces such as steady stokes drag $(F_d^{(i)})$, shear-induced lift $(F_l^{(i)})$, Magnus effect $(F_m^{(i)})$, buoyancy $(F_b^{(i)})$, added mass $(F_a^{(i)})$, history $(F_h^{(i)})$ and other forces may be included in the calculation of $F^{(i)}$,

$$F^{(i)} = F_d^{(i)} + F_b^{(i)} + F_a^{(i)} + F_h^{(i)} + F_l^{(i)} + F_m^{(i)} + ..., \tag{3.2.2}$$

to accurately capture the motion of the particle (Maxey & Riley, 1983). Most of

these forces are derived for a setting in which the upstream flow field in known and unaffected by the presence of particle. As an example, the steady state Stokes drag force over a sphere with diameter of d_p and in a fluid with dynamic viscosity of μ is

$$F_d^{(i)} = 3\pi\mu d_p \left(u_f^{(i)} - u_p^{(i)} \right), \tag{3.2.3}$$

which is analytically derived based on the relative velocity between the *undisturbed* (upstream) fluid velocity, $u_f^{(i)}$, and the particle velocity of $u_p^{(i)}$. When two-phases are one-way coupled, i.e., the presence of particles do not affect the background flow through the momentum exchange (Elghobashi, 1991), this force is employed for tracking the particle to obtain its velocity and position as a function of time. In such a scenario, the particle force is not exerted to the flow and the fluid phase remains undisturbed. This process yields an accurate (and consistent with the closure model) computation of $u_f^{(i)}$ and thereby Eqs. 3.2.1 and 3.2.3. In contrast, when the two phases are two-way coupled, this force, with the same magnitude and opposite direction, is applied back to the background flow to capture the inter-phase momentum interactions. This inter-phase coupling disturbs the fluid velocity around the particle and the newly disturbed velocity, $u_d^{(i)}$, that is different from the undisturbed velocity, $u_f^{(i)}$, is used in the calculation of the drag force for the next time step. This force computed based on the disturbed fluid velocity is inaccurate and yields erroneous trajectory of the particle as well as the inter-phase momentum interactions. For simple canonical particle-laden flows that are not bounded, this inaccuracy depends on flow parameters such as (i) particle diameter to the grid size ratio (Λ), (ii) the choice of interpolation and distribution functions used in the PP approach, (iii) particle Reynolds number and (iv) particle Stokes numbers (Horwitz & Mani, 2016; Esmaily & Horwitz, 2018). Computing the undisturbed fluid velocity might be easy for some simple flows such as settling of a particle in a quiescent flow, as the unaffected field could be readily obtained from the upstream condition. However, for more complex flows with large number of particles, particularly in wall-bounded regimes, such a naive remedy becomes invalid due to the

fact that the whole flow field is disturbed. This issue necessitates development of a unified framework to accurately recover the undisturbed fluid velocity in general unbounded or wall-bounded particle-laden flows. The basic concept behind development of such a framework is described below.

Since the disturbed fluid velocity in a two-way coupled PP approach arises from a point-force, finding the disturbance created by this force can be used to correct the disturbed flow and obtained the undisturbed fluid velocity. In other words, after a point force is applied to fluid within a computational cell in a discretized domain, what is the cell fluid velocity (let us denote it by $u_c^{(i)}$) generated by this force, and what does it depend upon are the main questions under consideration. The $u_c^{(i)}$ is the velocity that is missing in the traditional two-way coupled PP approaches, and if found, could be added to the disturbed fluid velocity to obtain the undisturbed velocity as

$$u_f^{(i)} = u_d^{(i)} - u_c^{(i)} \tag{3.2.4}$$

Thus, any predictive scheme that can model $u_c^{(i)}$, would be able to accurately recover the undisturbed fluid velocity. The correction scheme presented here is based on a method to predict the velocity of fluid in the computational cell produced by a force applied at its cell center.

To obtain a generalized approach applicable to wide range of unbounded and wall-bounded particle-laden flows with different grid aspect ratios, consider a force of $F^{(i)}$ is applied to fluid at a computational cell in an anisotropic, Cartesian grid, that has an arbitrary size of $[a^{(1)}, a^{(2)}, a^{(3)}]$ and located near a no-slip wall, at a wall-normal distance of $x_c^{(2)}$ as shown in Fig. 3.1. Also, suppose that the force is applied to the center of the computational cell, i.e., is generated by a particle that is at the center of the computational cell. Hereinafter, the superscripts (1) and (3) are employed for streamwise and spanwise directions, respectively, while, (2) denotes the wall-normal direction. Note that here we use anisotropic Cartesian grids for simplicity, but this concept can be easily extended in the future to arbitrary shaped unstructured grids with complex boundary walls as well. Conceptually, the time
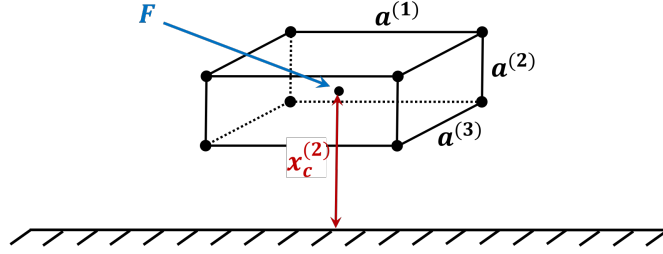
Figure 3.1: A computational cell with an arbitrary size of $[a^{(1)}, a^{(2)}, a^{(3)}]$ and wall-normal distance of $x_c^{(2)}$ that is disturbed by force $\mathbf{F}$.

dependent velocity created by this force could be approximated as

$$u_c^{(i)}(t) \approx f(a^{(1)}, a^{(2)}, a^{(3)}, F^{(i)}, t, x_c^{(2)}) \tag{3.2.5}$$

By varying the grid aspect ratio, the distance to the wall, and the amount of point-force applied, a data-set for the disturbance velocity of the computational cell as a function of time can be generated. Although finding a generic function for this data set may require some advanced data-science techniques, this relationship can be significantly simplified by applying a small force that limits us to the creeping/Stokes flow regime. For a small force and in the steady state condition, the velocity of the computational cell is linearly proportional to the force, i.e., $u_c^{(i)} \propto F^{(i)}$, and one can write it as a function of the cell dimensions and its wall distance, i.e., $u_c^{(i)} = F^{(i)} g(a^{(1)}, a^{(2)}, a^{(3)}, x_c^{(2)})$. This hypothesis is examined to a computational cell with an arbitrary size and situated at a wall distance. A small force is applied to this cell and its velocity as a function of time is measured. Regardless of size and the location of the cell, it is observed that its velocity exponentially accelerates until reaches a terminal velocity, precisely similar to the settling velocity of a spherical particle under gravity and in the presence of a drag force. Motivated by this observation and following Esmaily & Horwitz (2018), we model the computational cell as a solid object that is subjected to the particle force $F^{(i)}$, and dragged through the surrounding computational cells. At steady state, the particle force and the drag force exerted by the surrounding computational cells

balance each other and the computational cell velocity becomes only a function of its size and wall distance. The general form of the model then can be written using a Maxey-Riely equation of motion for the computational cell velocity, including the unsteady effect as,

$$\frac{3}{2}m_c\frac{du_c^{(i)}}{dt} = -3\pi\mu d_c K_t^{(i)}u_c^{(i)} - F^{(i)}, \qquad (3.2.6)$$

where $d_c=\sqrt[3]{(6/\pi)a^{(1)}a^{(2)}a^{(3)}}$ is the volume-equivalent diameter of the computational cell, with mass of $m_c=(\pi/6)\rho_f d_c^3$. The term on the left hand side expresses the unsteady effect of the force on the computational velocity wherein the prefactor $3/2$ captures the added mass effect. The first term on the right hand side of the equation, $3\pi\mu d_c K_t^{(i)}u_c^{(i)}$, is the Stokes drag force acting on the computational cell by its surrounding cells wherein the relative velocity is $-u_c^{(i)}$ as the ambient flow for the disturbance field is at rest. The adjustment to the Stokes drag is expressed by the factor $K_t^{(i)}$ as,

$$K_t^{(i)} = \frac{K_c^{(i)}C_r}{K_p^{(i)}C_t^{(i)}}. \qquad (3.2.7)$$

Here, $K_c^{(i)}$ accounts for non-sphericity of the computational cell and depends on its size and aspect ratio. The factor $K_p^{(i)}$ accounts for wall effects as well as the interpolation and distribution functions typically employed in PP approach. The factor C_r accounts for the non-linear finite force effects whereas $C_t^{(i)}$ considers the limited exposure time of the particle force to the computational cell. These geometric and physics-based factors are defined and explained in details in the following subsection.

3.2.1 Geometric correction factor, K_c

The geometric correction factor, K_c, is obtained based on the fact that a moving solid object in an unbounded flow with a small Reynolds number experiences a constant drag coefficient that is dependent on its shape and geometry (Leith,

1987). Inspired by this, the geometric correction factor to the Stokes drag of the computational cell is conjectured to be a function of its size. In this part, an expression for K_c is derived that is different than the one derived in the E&H work, in order to cover a wider range of grid sizes and aspect ratios, typically encountered in highly turbulent particle-laden channel flows.

The procedure is explained as follows. A sufficiently large computational domain is chosen with a uniform grid resolution of 128^3. Boundary conditions for wall-normal direction are set to be no-slip and slip to enforce wall effects while periodic boundary condition is employed for the other directions of the domain. A small and stationary force, $F_{small}^{(i)}$, that generates a disturbance field with nearly zero Reynolds number, is applied to the center of a computational cell in i direction. Note that the computational cell is located in the middle of a large domain wherein the no-slip boundary conditions have zero effect on the generated disturbance field. At steady state, the velocity of the computational cell is directly measured and $K_c^{(i)}$ is obtained by using Eq. 3.2.6 as,

$$K_{c,measured}^{(i)} = \left| \frac{F_{small}^{(i)}}{3\pi\mu d_c u_c^{(i)}} \right| \tag{3.2.8}$$

with other correction factors being one by definition as the force is small ($C_r=1$), applied only to one cell and sufficiently away from the no-slip wall ($K_p^{(i)}=1$), and has infinite exposure time ($C_t^{(i)}=1$). The procedure is repeated for a wide range of grid size of $0.05\sim a^{(2)}/a^{(1)}\sim1$ and $0.1\sim a^{(3)}/a^{(1)}\sim1$. The choice of grid size and aspect ratio studied here is inspired by the grid resolution of highly turbulent channel flows (Moser *et al.*, 1999). A best fit to the numerically measured data is obtained as,

$$
\begin{aligned}
K_c^{(i)} = {} &0.1705 \exp\left[(\Gamma_{max}^{(i)})^{-0.4005}(\Gamma_{min}^{(i)})^{0.06408}\right](\Gamma_{max}^{(i)})^{0.7058}(\Gamma_{min}^{(i)})^{-0.452} \\
&+ \ln\left[(\Gamma_{max}^{(i)})^{-0.03746}(\Gamma_{min}^{(i)})^{0.2049}\right](\Gamma_{max}^{(i)})^{0.355}(\Gamma_{min}^{(i)})^{0.05338},
\end{aligned}
\tag{3.2.9}
$$
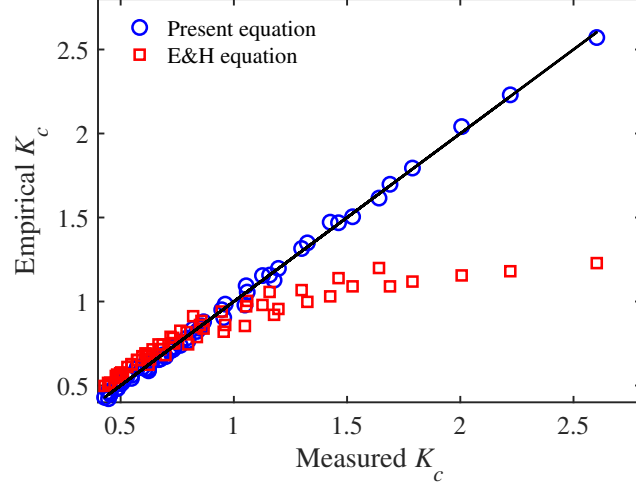
Figure 3.2: Prediction of Eq. 3.2.9 versus numerical measurements of K_c for a wide range of grid sizes typically encountered in wall-bounded turbulent channel flows.

where

$$\Gamma_{max}^{(i)} = \max \left\{ \frac{a^{(j)}}{a^{(i)}}, \frac{a^{(k)}}{a^{(i)}} \right\}, \quad \Gamma_{min}^{(i)} = \min \left\{ \frac{a^{(j)}}{a^{(i)}}, \frac{a^{(k)}}{a^{(i)}} \right\}; \quad j, k \neq i. \qquad (3.2.10)$$

Figure 3.2 shows excellent prediction of the above empirical equation against our numerical measurement for $K_c^{(i)}$. The prediction of the corresponding expression used in E&H is also shown. For the studied range of grid sizes, our new correlation matches with E&H for small $K_c^{(i)}$, but for larger $K_c^{(i)}$ values, which correspond to computational cells with higher aspect ratio, the new correlation matches much better than E&H. In the next part, we show the derivation of wall effects as well as the interpolation effects.

3.2.2 The wall and interpolation effects

The question that arises now is how does the geometric correction factor, $K_c^{(i)}$, change when the computational cell of interest gets closer to the wall? The answer

for this question lies in a new wall adjustment factor on geometric correction factor. In order to answer this question we first look at the near wall motion of a spherical object wherein its drag coefficient changes as a function of wall distance. Goldman *et al.* (1967) derived an analytical equation for the wall-modified drag coefficient of a sphere moving parallel to the wall, while Brenner (1961) using lubrication theory, obtained the corresponding parameter for its normal motion toward the wall. Based on these observations, it is expected that the wall adjustment on the geometric correction factor be dependent on the force direction and increases as wall-normal distance decreases. Having such a direction dependent adjustment is of importance as in wall-bounded particle-laden flows, particles interact with the sweep and burst events near the wall (Righetti & Romano, 2004), thus experiencing different forces in the two directions and disturbing the background flow differently.

Following the procedure described in the previous part for obtaining the $K_c^{(i)}$, its wall adjustment is achieved by applying the point-force at various wall distances. For each wall distance, Eq. 3.2.8 gives rise to a wall-modified geometric correction factor, $K_{c,w}^{(i)}$, that deviates from its unbounded counterpart, $K_c^{(i)}$. The ratio of these two yields a wall adjustment factor as

$$\Psi_k^{(i)} = \frac{K_{c,w}^{(i)}}{K_c^{(i)}}. \tag{3.2.11}$$

This factor approaches unity for cells sufficiently away from the wall (i.e., $K_{c,w}^{(i)} = K_c^{(i)}$) and is greater than one for those near the wall. This procedure is repeated for the studied range of the grid resolutions, for each of which, $\Psi_k^{(i)}$ for various wall distances with both wall-normal as well as parallel forces were measured and tabulated. As explained in Appendix A, for isotropic grid resolution, it is observed that the wall adjustment to the Stokes drag coefficient of a spherical object obtained empirically by Zeng *et al.* (2009) matches our measured data. This expression, however, deviates for highly skewed anisotropic grids, inevitably encountered in the wall-bounded flows. This underscores the need for a more accurate expression that could handle a wide range of grid aspect ratios. The best fit

to our measured data for forces in both parallel and normal directions was found to be,

$$\Psi_k^{(i)} = 1 + \frac{A^{(i)}}{1 + B^{(i)} h_k^{(i)}}, \tag{3.2.12}$$

where $h_k^{(i)}$ is the normalized wall distance of the center of the computational cell of interest as

$$h_k^{(i)} = \begin{cases} \frac{x_k^{(2)}}{a^{(i)}}, & \text{i=1,3} \\ \frac{x_k^{(2)}}{a^{(1)}}, & \text{i=2} \end{cases} \tag{3.2.13}$$

with $x_k^{(2)}$ being the dimensional wall distance of the computational cell, and $A^{(i)}$ and $B^{(i)}$ are dependent on the grid size as,

$$A^{(i)} = \begin{cases} \dfrac{\ln\left(26.31\frac{a^{(3)}}{a^{(1)}}\right)}{\left(0.05761+5.373\left(\frac{a^{(2)}}{a^{(1)}}\right)^{1.057}\right)}, & i = 1 \\[3ex] \dfrac{\ln\left(14.04\frac{a^{(3)}}{a^{(1)}}\right)}{\left(0.06608+5.14\left(\frac{a^{(2)}}{a^{(1)}}\right)^{1.592}\right)}, & i = 2 \\[3ex] \dfrac{\ln\left(26.31\frac{a^{(1)}}{a^{(3)}}\right)}{\left(0.05761+5.373\left(\frac{a^{(2)}}{a^{(3)}}\right)^{1.057}\right)}, & i = 3 \end{cases} \tag{3.2.14}$$

$$B^{(i)} = \begin{cases} \dfrac{\exp\left(-0.02873\frac{a^{(3)}}{a^{(1)}}\right)}{\left(0.00008+0.5601\left(\frac{a^{(2)}}{a^{(1)}}\right)^{1.894}\right)}, & i = 1 \\[3ex] \dfrac{\exp\left(-1.252\frac{a^{(3)}}{a^{(1)}}\right)}{\left(0.01354+3.688\left(\frac{a^{(2)}}{a^{(1)}}\right)^{2.202}\right)}, & i = 2 \\[3ex] \dfrac{\exp\left(-0.02873\frac{a^{(1)}}{a^{(3)}}\right)}{\left(0.00008+0.5601\left(\frac{a^{(2)}}{a^{(3)}}\right)^{1.894}\right)}, & i = 3 \end{cases} \tag{3.2.15}$$

As implied by Eq. 3.2.12, $\Psi_k^{(i)}$ becomes unity when the disturbance occurs sufficiently away from the wall as,
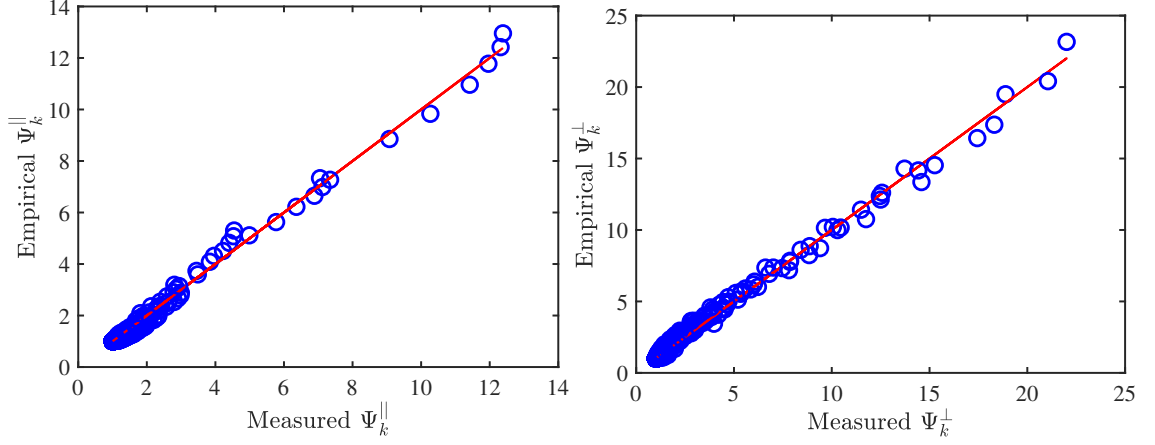
Figure 3.3: Shown are the predictions of Eqs. 3.2.12-3.2.15 and 3.2.17 for parallel forces, i.e., $i=1,3$ (left) and normal forces, i.e., $i=2$ (right) compared to the numerical measurements.

$$\lim_{h_k^{(i)} \to \infty} \Psi_k^{(i)} = 1. \tag{3.2.16}$$

It should be noted that our results show that for disturbances created by the wall-normal force applied to highly skewed grids, i.e., $a^{(2)}/a^{(3)} < 0.5$, $\Psi_k^{(i)}$ for the first computational cell attached to the wall is better predicted by,

$$\Psi_{first,cell}^{(2)} = \frac{\ln\left(25.3\frac{a^{(3)}}{a^{(1)}}\right)}{-0.0007149 + 2.364\left(\frac{a^{(2)}}{a^{(1)}}\right)^{0.7796}}. \tag{3.2.17}$$

Figure 3.3 shows the prediction of $\Psi_k^{(i)}$ using the above equations for both parallel and normal forces. Larger values correspond to the computational cells with high aspect ratio or those situated closer to the wall. Ignoring wall effect on the geometric correction factor and letting $\Psi_k^{(i)}=1$ yields overprediction of the computational velocity of the cell as $u_c^{(i)} \propto (\Psi_k^{(i)} K_c^{(i)})^{-1}$. As shown later, this over prediction becomes remarkable when particles travel very close to the wall which results in erroneous particle trajectory.

So far we considered the disturbance created by a small force that is applied to the center of a computational cell. This condition assumes that the particle force is applied only to a cell that contains the particle. However, in EL-PP simulations, this assumption does not necessarily hold, and the particle force is commonly distributed to the number of computational cells that are located within the stencil of the distribution function. Depending upon their distance from the force, they receive a fraction of this force and get disturbed differently. Now, in the next time step, when the fluid forces are to be computed, a function is similarly employed to interpolate the fluid quantities to the location of particle. During this process, the disturbance created in the surrounding computational cells in the previous time step will enter into the force calculations and depending on the stencil of this function, particle receives different disturbances. To accurately capturing the disturbance that particle receives, these effects must be accounted for in the correction scheme. Esmaily & Horwitz (2018) derived an analytical formulation for these effects for unbounded flows wherein the disturbance around the particle is symmetric. However, near a no-slip wall, the shape and strength of the disturbance field vary and it becomes more asymmetric. Below, we generalize the analytical expression of E&H to account for the no-slip walls and a new analytical expression is derived.

Suppose the particle force, $F_p^{(i)}$, is fed back to the background flow using a distribution function that has a certain bandwidth. Those computational cells that lie within the bandwidth receive a fraction of the force depending on their distance to the particle. Accordingly, the corresponding force that computational cell j receives is expressed as,

$$F_j^{(i)} = \beta_j F_p^{(i)}, \qquad (3.2.18)$$

where β_j is the distribution coefficient (weight) corresponding to the computational cell j. When the particle forces (e.g., the drag that requires fluid velocity) are being calculated, the disturbance field is interpolated to the particle location from the neighbouring cells as,

$$u_c^{(i)} = \sum_{j=1}^{nj} \gamma_j u_{c,j}^{(i)}, \tag{3.2.19}$$

where $u_c^{(i)}$ is the disturbance that particle receives in i direction and γ_j is the interpolation coefficient corresponding to the computational cell j that has computational velocity (disturbance velocity) of $u_{c,j}^{(i)}$. n_j is the total number of adjacent computational cells that are employed for the interpolation. It is imperative to note that unlike staggered grids, in collocated arrangements, γ_j and β_k coefficients are direction independent. The question that arises here is how to compute the computational velocity of the adjacent computational cells, $u_{c,j}^{(i)}$, when they are imposed to a fraction of particle force. A naive way to obtain that, is to simply use Eq. 3.2.6 for each cell with its given force, $F_j^{(i)}$, assuming that the computational cells are independent and only disturbed by their direct forces. In practice, however, this assumption does not hold and each computational cell gets disturbed not only by their direct force but also through the perturbations induced by the adjacent cells. For instance, when the computational cell k is disturbed by its own force, $\beta_k F_p^{(i)}$, the created disturbance velocity in this cell pushes and perturbs the surrounding cells through $\alpha_{kj}^{(i)}$ that is the velocity ratio of cell j generated by perturbation of cell k to that of the computational cell k. This implies the fact that the disturbance created in computational cell, e.g., j, constitutes a combination of the one created by its own direct force and those created by the adjacent cells. Upon finding a closure for $\alpha_{kj}^{(i)}$, a linear superposition is valid if the created disturbance field meets the zero Reynolds number criterion. For unbounded flows and in the limit of zero Reynolds number, Esmaily & Horwitz (2018) showed that $\alpha_{kj}^{(i)}$ can be predicted using the Stokes solution that is the solution for the velocity field generated around a sphere slowly moving in an unbounded quiescent flow as

$$\alpha_{kj}^{(i)} = \frac{3}{4} r_{kj}'^{-1} \left(1 + cos^2\theta_{kj}^{(i)} \right) + \frac{1}{4} r_{kj}'^{-3} \left(1 - 3cos^2\theta_{kj}^{(i)} \right), \tag{3.2.20}$$

where $\theta_{kj}^{(i)}$ is the polar angle between the line passing through the computational
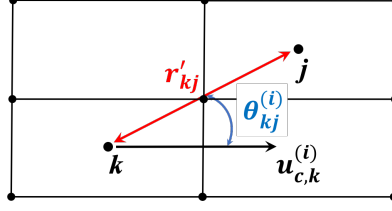
Figure 3.4: Schematic of computational cell k that is disturbed by a small force and has disturbance velocity of $u_{c,k}^{(i)}$ which perturbs the adjacent computational cells through the modelled Stokes solution. r'_{kj} is the normalized distance between cell k and j with polar angle of $\theta_{kj}^{(i)}$ between the line passing through these cells and i direction.

cells k and j and the i direction (Fig. 3.4) and r'_{kj} is the distance between these two cells normalized by the characteristic length of the computational cell. The choice of this equation was inspired by the fact that the computational cell is treated as a solid object that moves in the fluid and consequently disturbs the surrounding fluid in a manner similar to a solid sphere. Using the prediction of this equation and a characteristic length of $0.28d_c$, they showed an excellent agreement with their numerical measurements.

For the collocated grid arrangement used in this study, we found that Stokes solution (Eq. 3.2.20) normalized with a smaller characteristic length of $0.25dc$ better predicts our numerical measurements. This was done by performing measurements similar to the previous parts. A small force in i direction is applied to the computational cell k located in the middle of a sufficiently large periodic box. At steady state, we measure the velocity of the perturbed cell (k) as well as those of its adjacent cells (j). The velocity ratio of these two cells, $u_{c,j}^{(i)}/u_{c,k}^{(i)}$, is $\alpha_{kj}^{(i)}$ by definition. For the sake of clarity, this parameter could be alternatively denoted by b_{lmn} in which the subscript lmn corresponds to the location of cell j, that is $[la^{(1)}, ma^{(2)}, na^{(3)}]$ away from the computational cell k. As an example, b_{100} represents the velocity ratio of cell j to k with j being the immediate cell in the (1) direction and right hand side of the perturbed cell k. Table 3.1 shows the prediction of Eq. 3.2.20 normalized with both $0.25d_c$ and $0.28d_c$ compared to our

numerical measurements on the collocated grid arrangement for different aspect ratios. Better predictions are obtained by the former characteristic length. For the sake of comparison, we have also included the corresponding values of Esmaily & Horwitz (2018) that are based on the staggered grid arrangements, revealing a slight difference between these two arrangements. The difference is justified due to the fact that in collocated arrangements, unlike the face velocity, the cell-centered velocity is not necessarily divergence free, thereby causing small errors in the results compared to those of the staggered arrangements.

$a^{(2)}/a^{(1)}$	$a^{(3)}/a^{(1)}$			b_{000}	b_{100}	b_{010}	b_{110}	b_{001}	b_{101}	b_{011}	b_{111}
1.0	1.0	measured	collocated	1.0	0.31	0.27	0.18	0.27	0.18	0.16	0.14
			staggered	1.0	0.50	0.25	0.24	0.25	0.24	0.15	0.16
		predicted	using $0.25d_c$	1.0	0.45	0.24	0.25	0.24	0.25	0.17	0.18
			using $0.28d_c$	1.0	0.50	0.27	0.27	0.27	0.27	0.19	0.20
1.0	2.0	measured	collocated	1.0	0.41	0.33	0.26	0.19	0.17	0.15	0.14
			Staggered	1.0	0.62	0.33	0.34	0.17	0.18	0.13	0.15
		predicted	using $0.25d_c$	1.0	0.56	0.31	0.31	0.15	0.16	0.13	0.14
			using $0.28d_c$	1.0	0.61	0.35	0.34	0.17	0.18	0.15	0.16
2.0	4.0	measured	collocated	1.0	0.62	0.36	0.34	0.22	0.21	0.18	0.18
			staggered	1.0	0.83	0.31	0.34	0.16	0.17	0.13	0.13
		predicted	using $0.25d_c$	1.0	0.81	0.24	0.25	0.12	0.12	0.10	0.11
			using $0.28d_c$	1.0	0.87	0.27	0.28	0.13	0.13	0.12	0.12

Table 3.1: Measured b_{lmn} values in comparison with the prediction of Eq. 3.2.20 normalized with the characteristic length of $0.25d_c$ and $0.28d_c$. Shown also includes the corresponding measured values from Esmaily & Horwitz (2018) that are based on the staggered grid arrangement.

The next step is answering the question of how does α_{kj} change when the disturbance occurs close to a no-slip wall? One could substitute this parameter with the wall-bounded Stokes solution of a sphere moving in a quiescent flow and near a no-slip wall (O'Neill, 1964, 1967). Although there have been a few methods for simplifying such solution (e.g., Chaoui & Feuillebois (2003)), it is expressed as expansions of spherical harmonics with the coefficients that are obtained iteratively

as the solution of an infinite linear system. This makes the use of wall-bounded Stokes solution computationally expensive for EL approaches.

An alternative remedy is the choice of the "Stokeslet solution" that is the flow field generated by a point force in a quiescent fluid. Direct analytical solutions are available for both unbounded and wall-bounded flows (Blake, 1971) that makes it more desirable and feasible to be implemented in EL approaches. Assuming that the ratio of the wall-bounded to the unbounded Stokes solution, $\alpha_{stk,b}^{(i)}/\alpha_{stk,un}^{(i)}$, approximately equals to the corresponding ratio of Stokeslet solution, $\alpha_{stkl,b}^{(i)}/\alpha_{stkl,un}^{(i)}$, an analytical expression for the wall adjustment to $\alpha_{kj}^{(i)}$ is derived (see Appendix B for the detailed Stokeslet solutions) as,

$$\Phi_{kj}^{(i)} = \frac{(\alpha_{stkl,b}^{(i)})_{kj}}{(\alpha_{stkl,un}^{(i)})_{kj}} = 1 - \left[\frac{\frac{1}{|R_{kj}|} + \frac{(R_{kj}^{(i)})^2}{|R_{kj}|^3} + \frac{2x_k^{(2)}f_{kj}^{(i)}}{|R_{kj}|^6}}{\frac{1}{|r_{kj}|} + \frac{(r_{kj}^{(i)})^2}{|r_{kj}|^3}} \right], \qquad (3.2.21)$$

where,

$$f_{kj}^{(i)} = (-1)^i \left(x_k^{(2)}|R_{kj}|^3 - 3|R_{kj}|(R_{kj}^{(i)})^2 x_k^{(2)} - |R_{kj}|^3 R_{kj}^{(2)} + 3|R_{kj}|(R_{kj}^{(i)})^2 R_{kj}^{(2)} \right) \qquad (3.2.22)$$

$$r_{kj}^{(i)} = (x_j^{(i)} - x_k^{(i)}), \quad |r_{kj}| = \sqrt{\sum_{i=1}^{3}(r_{kj}^{(i)})^2} \qquad (3.2.23)$$

$$R_{kj}^{(i)} = \begin{cases} r_{kj}^{(i)}, & i = 1, 3 \\ r_{kj}^{(2)} + 2x_k^{(2)}, & i = 2 \end{cases}, \quad |R_{kj}| = \sqrt{\sum_{i=1}^{3}(R_{kj}^{(i)})^2} \qquad (3.2.24)$$

and $x_j^{(i)}$ and $x_k^{(i)}$ are the i coordinate of the computational cell j and k, respectively. Note that $\Phi_{kj}^{(i)}$ is not normalized by any characteristic length that makes it general for both staggered and collocated grid arrangements. It is imperative to mention that when the disturbance created by a particle is situated sufficiently away from the wall, both bounded and unbounded Stokeslet solutions become identical and

this parameter becomes unity as

$$\lim_{x_k^{(2)} \to \infty} \Phi_{kj}^{(i)} = 1, \qquad (3.2.25)$$

which makes the model general for capturing the disturbance field created at any wall distance, a common scenario in wall-bounded particulate flows. Knowing the adjacent perturbations, now we can find the computational velocity of each cell and derive the analytical expression for $K_p^{(i)}$ as follows.

For the particle force that is stationary and distributed to its neighbour cells, in the limit of steady state and zero Reynolds number, the computational velocity of cell j is obtained as the superposition of disturbances created by its own force as well as its adjacent cells as expressed below

$$u_{c,j}^{(i)} = \sum_{k=1}^{n_k} \left[\frac{\alpha_{kj}^{(i)} \beta_k \Phi_{kj}^{(i)}}{\Psi_k^{(i)}} \right] \frac{-F_p^{(i)}}{3\pi\mu d_c K_c^{(i)}}, \qquad (3.2.26)$$

where n_k is the total number of computational cells to which the particle force is distributed. In Eq. 3.2.26 and what follows, no implicit summation over repeated indices is implied. Note that we keep the wall adjustment to the geometric correction factor, $\Psi_k^{(i)}$, in the bracket as it varies among the adjacent cells owing to their different wall-normal distances. Knowing the disturbance velocity for the computational cells around the particle, the disturbance velocity seen by the particle is obtained using Eqs. 3.2.19 and 3.2.26 as,

$$u_c^{(i)} = \sum_{j=1}^{n_j} \left[\gamma_j \sum_{k=1}^{n_k} \left[\frac{\alpha_{kj}^{(i)} \beta_k \Phi_{kj}^{(i)}}{\Psi_k^{(i)}} \right] \right] \frac{-F_p^{(i)}}{3\pi\mu d_c K_c^{(i)}}, \qquad (3.2.27)$$

where n_j is the total number of computational cells from which the fluid properties are interpolated to the particle location. The analytical expression for $K_p^{(i)}$ is then derived as

$$K_p^{(i)} = \sum_{j=1}^{n_j} \left[\gamma_j \sum_{k=1}^{n_k} \left[\frac{\alpha_{kj}^{(i)} \beta_k \Phi_{kj}^{(i)}}{\Psi_k^{(i)}} \right] \right].$$
$\qquad(3.2.28)$

In the limit of large wall distances, since both $\Psi_k^{(i)}$ and $\Phi_{kj}^{(i)}$ approach unity, the $K_p^{(i)}$ derived here becomes identical to that derived in E&H. It is crucial to mention that with this formulation all wall adjustments have been accounted for in the derivation of $K_p^{(i)}$.

For cases where only "box filtering" (zeroth order) is utilized, i.e., the particle only disturbs one cell from which the fluid properties are interpolated to the particle too ($n_k=n_j=1$), we have $\gamma_j=\beta_k=\alpha_{kj}^{(i)}=\Phi_{kj}^{(i)}=1$. In this case, $K_p^{(i)}=1/\Psi_k^{(i)}$, wherein subscript k corresponds to the cell in which the particle lies. In such a simple case, $K_p^{(i)}$ becomes only the wall effect on the correction scheme.

3.2.3   Correction for the finite Reynolds number

The Stokes drag used in Eq. 3.2.6 is only valid for disturbances created with zero Reynolds number. To account for the higher Reynolds number effects, a Schiller-Naumann correction factor, analogous to the finite Reynolds number adjustment to the Stokes drag of a sphere (Clift *et al.*, 2005),

$$C_r = 1 + 0.15 Re_c^{0.687} \qquad(3.2.29)$$

can be used (Esmaily & Horwitz, 2018); where, $Re_c=u_c d_c/\nu$ is defined as the Reynolds number of the computational cell based on its velocity and diameter. A wall-modified version of this equation has been empirically derived by Zeng *et al.* (2009), yet our results show that the use of Schiller-Naumann expression (Eq. 3.2.29) still yields better predictions for the studied wall-bounded cases. This expression captures only the change to the Stokes drag for higher Re_c cases, however, the complexity of the asymmetric disturbance field at high Re_c breaks the use of Eq. 3.2.20, and the linear superposition employed in the derivation of Eq. 3.2.28 does not hold anymore. Therefore, it is argued that for high Re_c,

a more elaborate formulation might be required. As explained later, our results illustrate that the current formulation generates reasonable results for cases with Re_c of up to 10. For larger Re_c, Balachandar *et al.* (2019) showed that the need for the correction diminishes owing to the fact that the particle with larger Re_p does not stay in its own disturbance, and in the next time step, it sees a more undisturbed flow for the force calculations. Although this effect is partly captured by introducing a temporal correction factor for finite exposure time, $C_t^{(i)}$, explained in the next part, a comprehensive study on the necessity of the correction scheme for a range of particle Reynolds number is left for future investigations.

3.2.4   Correction for the finite exposure time

A particle moving in the computational domain spends a limited time within each computational cell and disturbs the cell for a finite time. This finite time exposure of particle has to be accounted for in Eq. 3.2.6, separately. The unsteady term in this equation is considered for the unsteady effect of a stationary force and does not include its limited exposure time. To demonstrate the need for this correction factor, consider a high velocity particle whose residency time within the computational cell with diameter of d_c is d_c/u_p, which is much smaller than the response time of the fluid to the particle force, d_c^2/ν, i.e.,

$$\frac{d_c}{u_p} \ll \frac{d_c^2}{\nu} \tag{3.2.30}$$

If particle size is assumed to be in the same order of the computational cell, i.e., $d_p \sim d_c$, then this criterion results in $Re_p \gg 1$. In such scenario, particle passes through the grid quickly with negligible disturbance that obviates any need for the correction. Conversely, for particles with $Re_p \ll 1$, their large exposure time allows them to sufficiently perturb the computational cell which underscores the need for the correction. This effect should be accounted for in Eq. 3.2.6 separately as for cases with $Re_p \gg 1$, this equation yields erroneously large computational velocity, which conceptually should be zero. In order to account for this effect, one could

track the particle within each computational cell and only integrate Eq. 3.2.6 over the period of time that particle spends in the cell and upon its exit the force becomes zero. To avoid the complexity added by this, we use the corresponding correction factor of E&H as,

$$C_t^{(i)} = 1 - \frac{\tau_c^{(i)}}{\Delta t^{(i)}} \left(1 - \exp\left(-\frac{\Delta t^{(i)}}{\tau_c^{(i)}} \right) \right), \qquad (3.2.31)$$

where,

$$\Delta t^{(i)} = \frac{a^{(i)}}{|u_p^{(i)}|} \quad \text{and} \quad \tau_c^{(i)} = \frac{d_c^2}{12\nu K_c^{(i)}}, \qquad (3.2.32)$$

where $\tau_c^{(i)}$ and $\Delta t^{(i)}$ are respectively the computational cell relaxation time and the particle residence time in i direction of the computational cell, respectively. The factor $C_t^{(i)}$ is a time-average of the solution of Eq. 3.2.6 for a small force that is applied on top of a computational cell. Accordingly, for a particle with $Re_p \gg 1$, its exposure time to the cell becomes small, $\Delta t \to 0$ and using Eq. 3.2.31, $C_t^{(i)} \to 0$ which eliminates any need for correction. However, for slow particles ($Re_p \ll 1$), $\Delta t \to \infty$ and $C_t^{(i)} \to 1$ which enforces the correction. In the next part, we combine all these correction factors and explain the steps in order to correct the PP approach.

3.2.5 The correction algorithm

The entire correction scheme reduces to the computation of Eq. 3.2.6 that is solved concurrently with the equation of motion of the particle (Eq. 3.2.1). Although one could simply use any time integration scheme for these two equations, we use an explicit method for the results presented in this work. Therefore, knowing the $u_c^{(i)}$ and $u_p^{(i)}$ from previous time step, the following procedure is used.

1. Compute the disturbed velocity at the location of particle, $u_d^{(i)}$, that is readily available in the standard PP packages.
2. Compute the undisturbed velocity at the location of particle, $u_f^{(i)}$, by using Eq.

3.2.4 and having the computational velocity at the location of particle, $u_c^{(i)}$.

3. Compute the total fluid force exerted at the location of particle, $F^{(i)}$.

4. Update the velocity of particle, $u_p^{(i)}$, using Eq. 3.2.1.

5. Calculate $K_c^{(i)}$ using Eqs. 3.2.9 and 3.2.10 based on the grid size $[a^{(1)}, a^{(2)}, a^{(3)}]$ in which particle is located.

6. Identify the location of surrounding cells to which the particle force is distributed (n_k).

7. Identify the location of surrounding cells from which the fluid quantities are interpolated to the location of particle (n_j).

8. From the location of particle to the above computational cells, calculate r'_{kj} and $\theta_{kj}^{(i)}$ and thereby $\alpha_{kj}^{(i)}$ using Eq. 3.2.20.

9. In the presence of no-slip walls, calculate $\Phi_{kj}^{(i)}$ and $\Psi_k^{(i)}$ based on Eqs. 3.2.12-3.2.15 and Eqs. 3.2.21-3.2.24, respectively.

10. Compute $K_p^{(i)}$, using Eq. 3.2.28 and knowing β_k, γ_j, $\alpha_{kj}^{(i)}$, $\Phi_{kj}^{(i)}$ and $\Psi_k^{(i)}$.

11. Compute Re_c and thereby C_r using Eq. 3.2.29.

12. Compute $\tau_c^{(i)}$ and $\Delta t^{(i)}$ using Eq. 3.2.32 and thereby $C_t^{(i)}$ using Eq. 3.2.31.

13. Compute $K_t^{(i)}$ using Eq. 3.2.7 by knowing $K_c^{(i)}$, $K_p^{(i)}$, C_r and $C_t^{(i)}$.

14. Update $u_c^{(i)}$ using Eq. 3.2.6.

The initial condition for the procedure above is $u_c^{(i)}=0$ corresponding to the undisturbed fluid phase before injecting particles. For isotropic grids, the simplified formulation introduced in Appendix A could be used to compute $\Psi_k^{(i)}$ in the step 9 above. It is imperative to mention that for particle-laden flows wherein the particle time scale is smaller than that of the fluid, sub-cycling for particles' motion is typically performed. Particles are advanced during the frozen flow time scale and then at the end of the sub-cycling their force will be applied to the background flow. For such cases, the correction should be enforced once the sub-cycling is finished as that is when the flow is altered by the presence of particles. In the next section, the results of the present correction scheme are discussed and the accuracy of the scheme is assessed.

3.3   Results

In this section, the present correction scheme is verified by performing several test cases involving unbounded and wall-bounded flows. Different flow parameters and grid aspect ratios are carried out in order to assess the generality and robustness of the model for a wide range of applications. In the first set of computations, we start with settling velocity of a particle in an unbounded flow wherein the wall effects do not appear and the model for the collocated arrangements is validated against the analytical solution. In the second set of test cases, the model is validated for velocity of a particle settling parallel and close to a no-slip wall. Test cases at different wall distances, ranging from near to sufficiently away from the wall, are performed to test the model for possible situations that happen in particle-laden flows. Different grid aspect ratios representative of typical turbulent channel flows are used in these tests. In the third set of assessments, the model will be employed to freely falling motion of a particle normal to the wall. The grid resolution for all cases was set to be 128^3 as it was found to be sufficient to produce the results that are grid independent.

The three shared non-dimensional flow parameters among cases are those defined based on the Stokes flow in an unbounded configuration. The first one is the Stokes parameter, St, defined as the ratio of the particle relaxation time, τ_p, to the fluid time scale, τ_f, as,

$$St = \frac{\tau_p}{\tau_f}, \tag{3.3.1}$$

where,

$$\tau_p = \frac{\rho_p d_p^2}{18\mu}, \tag{3.3.2}$$

and,

$$\tau_f = \frac{\min\left(a^{(i)}\right)^2}{\nu}, \tag{3.3.3}$$
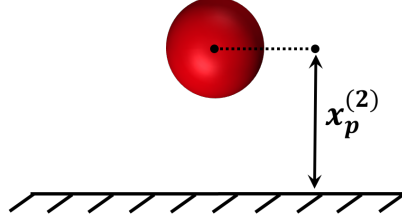
Figure 3.5: Particle located at wall distance of $x_p^{(2)}$ near a no-slip wall.

The second parameter is the particle Reynolds number as,

$$Re_p^{Stk} = \frac{|\mathbf{u}_s^{Stk}|d_p}{\nu}, \tag{3.3.4}$$

where,

$$\mathbf{u}_s^{Stk} = (1 - \rho_f/\rho_p)\,\tau_p\mathbf{g}, \tag{3.3.5}$$

is the particle settling velocity under gravity, $\mathbf{g}$, in an unbounded Stokes flow with ρ_f and ρ_p being the fluid and particle densities, respectively. The third parameter that has three components as the ratio of particle diameter to the grid size is

$$\Lambda^{(i)} = \frac{d_p}{a^{(i)}}. \tag{3.3.6}$$

For wall-bounded test cases, another non-dimensional parameter that is the normalized wall distance from the bottom of particle is defined as (see Fig. 3.5)

$$\delta_p = \frac{x_p^{(2)}}{d_p} - 0.5, \tag{3.3.7}$$

wherein $x_p^{(2)}$ is the wall distance from the center of particle. It should be noted that in wall-bounded cases, since the particle drag coefficient changes due to the presence of wall, its actual Reynolds number then differs from its unbounded counterpart expressed by Eq. 3.3.4.

For the first and second test cases, we evaluate the accuracy of the model based on the errors in the settling, drifting and total velocities of the particle compared

to their reference values. Accordingly, the particle velocity, $\mathbf{u}_p(t)$, is decomposed into two components; parallel and perpendicular to the reference velocity of $\mathbf{u}_r$. The parallel component is expressed as,

$$\mathbf{u}_p^{\|} = \frac{\mathbf{u}_r \cdot \mathbf{u}_p(t)}{|\mathbf{u}_r|^2} \mathbf{u}_r, \tag{3.3.8}$$

while the perpendicular component is obtained by,

$$\mathbf{u}_p^{\perp} = \mathbf{u}_p(t) - \mathbf{u}_p^{\|}. \tag{3.3.9}$$

The errors in these two velocity components are then calculated based on the following metrics,

$$e^{\|} = \frac{\overline{\mathbf{u}_p^{\|}(t).\mathbf{u}_r}}{|\mathbf{u}_r|^2} - 1; \tag{3.3.10}$$

$$e^{\perp} = \frac{\overline{|\mathbf{u}_p^{\perp}(t)|}}{|\mathbf{u}_r|}, \tag{3.3.11}$$

where, overbar $\overline{()}$ denotes the time averaging. Finally, error in the total velocity compared to the reference velocity is obtained as,

$$e = \frac{\overline{|\mathbf{u}_p(t) - \mathbf{u}_r|}}{|\mathbf{u}_r|}. \tag{3.3.12}$$

The reference velocity, $\mathbf{u}_r$, is the settling velocity of particle that is defined differently for each case depending on the corresponding drag coefficient.

3.3.1 Settling particle in an unbounded flow

In the test cases here, we first validate the present correction scheme for the unbounded flows in order to assess the new presented $K_c^{(i)}$ equation and the new characteristic length employed for normalization of Eq. 3.2.20. Settling velocity of a particle in an unbounded periodic domain is performed. For the results of this part,

we neglect the wall effects by setting $\Psi_k^{(i)}=\Phi_{kj}^{(i)}=1$. For all test cases, a particle that is initially stationary, $u_p^{(i)}=0$, thus $u_c^{(i)}=0$, and located in an unbounded flow settles under gravity and in the presence of the stokes drag force. Following the advice by Horwitz & Mani (2016), gravity vector is chosen as $\mathbf{g}=(1, (1+\sqrt{5})/2, \exp(1))/|\mathbf{g}|$ so that particle sweeps through different locations among its adjacent computational cells ensuring that the model is capable of handling any arbitrary positioning of particle. The particle equation of motion in a quiescent fluid is then written as

$$\frac{d\mathbf{u}_p}{dt} = \left(1 - \frac{\rho_f}{\rho_p}\right)\mathbf{g} - \frac{f}{\tau_p}\mathbf{u}_p \qquad (3.3.13)$$

where f corresponds to any adjustment factor to the Stokes drag coefficient that is unity for the studied cases in this part. Accordingly, the analytical solution for the particle velocity for Stokes flow is obtained as

$$\mathbf{u}^{Stk}(t) = \mathbf{u}_s^{Stk}\left(1 - \exp(-\frac{t}{\tau_p})\right) \qquad (3.3.14)$$

where $\mathbf{u}_s^{Stk}$ is the settling velocity as provided in Eq. 3.3.5 and serves as the reference velocity. Table 3.2 shows six different cases with various flow parameters and grid aspect ratios for all which the error in settling velocity of the particle without the correction is remarkably large. Errors in settling, drifting and total velocities of the particle predicted with and without the present correction scheme are compared. Additionally, the corresponding values from E&H are listed for comparison. In general, the present scheme reduces the errors with the same order of magnitude as E&H, however, for cases with large size particles such as case U02, the embedded error in the collocated arrangement that appears in the computation of Eq. 3.2.20 inevitably yields larger values compared to the staggered arrangement. It is worth mentioning that the time step used for the computations of the current cases is half of those reported in Horwitz & Mani (2016) so that the Peclet number of $Pe=6\nu_f\Delta t/\min(a^{(i)})^2=0.18$ as well as particle Courant number of $CFL_p=\Delta t/\tau_p=0.003$ are satisfied.

Figure 3.6 shows the particle velocity of case U01 as a function of time with

Case	Re_p^{Stk}	St	$\Lambda^{(1)}$	$\Lambda^{(2)}$	$\Lambda^{(3)}$	uncorrected			E&H			present model		
						$e^\parallel$	$e^\perp$	e	$e^\parallel$	$e^\perp$	e	$e^\parallel$	$e^\perp$	e
U01	0.1	10.0	1.0	1.0	1.0	78.94	0.074	78.94	0.83	0.44	1.00	0.59	0.74	1.05
U02	0.1	10.0	5.0	5.0	5.0	392.14	0.25	392.14	1.70	5.20	7.50	-1.98	7.40	10.97
U03	0.1	10.0	5.0	0.5	0.5	57.40	7.98	57.96	-2.00	1.80	2.90	-3.91	2.07	4.59
U04	0.1	10.0	4.0	2.0	0.2	51.22	10.65	51.32	-3.50	6.00	7.30	-4.62	2.61	5.70
U05	0.5	10.0	1.0	1.0	1.0	68.64	0.08	68.64	4.30	2.00	4.70	4.83	2.29	5.35
U06	0.1	0.25	1.0	1.0	1.0	78.73	0.57	78.73	0.43	0.86	1.40	-0.1	1.86	2.85

Table 3.2: Listed are the percentage errors for settling, drifting and total velocity of a particle settling in an unbounded domain. Results with and without the present correction scheme are compared with the corresponding values from E&H. Various cases with different particle diameter to gird sizes, Λ, particle Reynolds numbers, Re_p, and particle Stokes numbers, St, are shown for validation.

and without the correction scheme. As illustrated, the present correction scheme produces excellent result compared to the reference velocity.

3.3.2 Settling particle parallel to the wall

As the first step toward validating wall effects in the present correction scheme, velocity of a particle settling parallel to a no-slip wall is tested at different wall distances. In order to illustrate the need for the present scheme, results with and without accounting for $\Psi_k^{(i)}$ and $\Phi_{kj}^{(i)}$ in the formulation are compared against the reference. As listed in Tab. 3.3, different flow parameters, grid aspect ratios and particle to grid sizes are carried out to assess the capability of the model for a wide range of applications. Similar to the preceding section, the errors in settling, drifting and total velocities of the particle are measured and compared among different schemes. For the studied cases, a particle that is initially located at a normalized wall gap, δ_p, released to reach its settling velocity under a gravity vector of $\mathbf{g}=(\exp(1), 0, (1+\sqrt{5})/2)/|\mathbf{g}|$ that guarantees the particle's motion on a plane parallel to the wall. In reality, the particle experiences a lateral force (Vasseur & Cox, 1977; Takemura & Magnaudet, 2003), yet in this study other directions are neglected in order to isolate the parallel motion. The particle's equation of motion
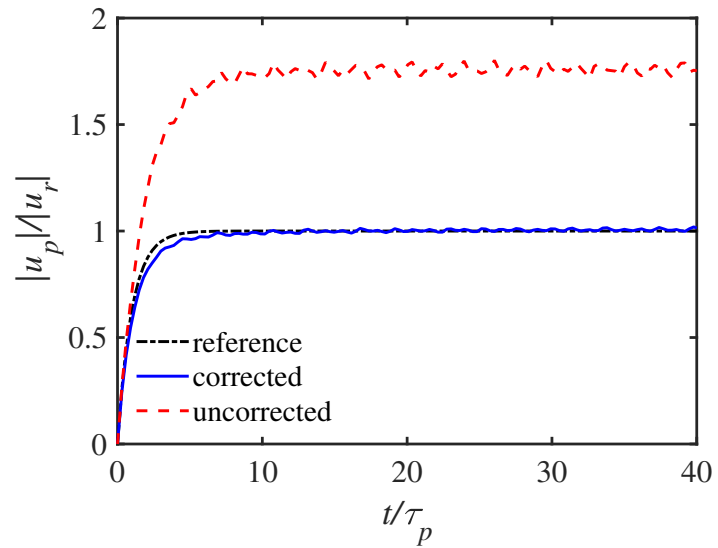
Figure 3.6: Plotted is the velocity of a settling particle as a function of time in an unbounded domain. Analytical solution (dash-dotted black), prediction of the present correction scheme (solid blue) as well as the uncorrected scheme (dashed red) are compared. The reference velocity, u_r, used for normalization is the particle settling velocity in Stokes flow given by Eq. 3.3.5. Results pertain to case U01 from Tab. 3.2.

in the presence of wall follows Eq. 3.3.13 with the correction factor of f that is employed based on the work of Zeng *et al.* (2009). In their work, an empirical drag coefficient is derived as a function of normalized wall gap, δ_p, and the relative Reynolds number, Re_p, for a spherical object moving parallel to the wall and in a quiescent flow as,

$$C_d^{w,\|} = \frac{24}{Re_p} f^{\|}(\delta_p, Re_p), \tag{3.3.15}$$

where $f^{\|}(\delta_p, Re_p)$ is the correction factor to the Stokes drag including two terms as

$$f^{\|}(\delta_p, Re_p) = f_1^{\|}(\delta_p) f_2^{\|}(\delta_p, Re_p), \tag{3.3.16}$$

where,

$$f_1^{\|}(\delta_p) = \left[1.028 - \frac{0.07}{1 + 4\delta_p^2} - \frac{8}{15} \log\left(\frac{270\delta_p}{135 + 256\delta_p}\right)\right], \tag{3.3.17}$$

$$f_2^{\|}(\delta_p, Re_p) = \left[1 + 0.15\left(1 - \exp\left(-\sqrt{\delta_p}\right)\right) Re_p^{\left(0.687 + 0.313 \exp\left(-2\sqrt{\delta_p}\right)\right)}\right]. \tag{3.3.18}$$

$f_1^{\|}(\delta_p)$ captures the wall effects on the Stokes drag for zero Re_p that becomes unity for large δ_p, recovering the Stokes drag coefficient. $f_2^{\|}(\delta_p, Re_p)$, however, handles the wall-modified finite Reynolds number effects to the Stokes drag that converts to the Standard Schiller-Naumman correction factor (Clift *et al.*, 2005) when particle travels sufficiently away from the wall.

For the first cases studied in this part, Re_p is very small, thus only $f_1^{\|}(\delta_p)$ holds and the particle velocity is directly solved as,

$$\mathbf{u}^{w,\|}(t) = \mathbf{u}_s^{w,\|}\left(1 - \exp\left(-\frac{t}{\tau_p} f_1^{\|}(\delta_p)\right)\right) \tag{3.3.19}$$

where, $\mathbf{u}_s^{w,\|}$ is the particle settling velocity in parallel motion to the wall and in

the limit of $Re_p{\sim}0$ as,

$$\mathbf{u}_s^{w,||} = \left(1 - \frac{\rho_f}{\rho_p}\right) \frac{\tau_p \mathbf{g}}{f_1^{||}(\delta_p)} \tag{3.3.20}$$

Based on this drag formulation, the actual particle relaxation time in the presence of wall then becomes,

$$\tau_p^{w,||} = \frac{\tau_p}{f_1^{||}(\delta_p)} \tag{3.3.21}$$

Results based on the prediction of different schemes are compared with the reference given by Eq. 3.3.20. Following the metrics presented in the preceding section, the errors in settling, drifting and total velocities are measured. Table 3.3 shows these errors for the studied cases of this part which includes five sets, each of which has six cases corresponding to settling at different normalized wall gaps. Results with and without the wall correction factors on the correction scheme, $\Psi_k^{(i)}$ and $\Phi_{kj}^{(i)}$, are compared together with those of the uncorrected scheme to quantify the need for the wall-modified corrections scheme. For all the sets studied in this part, the particle Reynolds number of $Re_p^{Stk}{=}0.1$ and Stokes number of $St{=}10$ that are based on unbounded parameters, are kept constant. In practice, however, the actual particle Reynolds number decreases when it gets closer to the wall owing to the larger drag and this effect is studied separately in the next part.

Sets A and B correspond to isotropic grid configuration with two different particle diameter to grid sizes, whereas the rest, C-F, pertain to anisotropic grids with various aspect ratios. The grid resolution used in the latter are those commonly encountered in the turbulent channel flows. The first observation from Tab. 3.3 is that the errors for the uncorrected scheme is significantly large for all cases, necessitating the need for correcting the Point-Particle approach even in the presence of a no-slip wall. In addition, consistent with observation of E&H, the error in uncorrected results increases proportional to $(\Lambda^{(1)}\Lambda^{(2)}\Lambda^{(3)})^{1/3}{\propto}d_p/d_c$. As an example, the error in total velocity of the uncorrected scheme for case C1 is two order of magnitude smaller than that of case B1 wherein the volume ratio of particle to

the grid is much greater.

In the first place, one could correct the PP results with the unbounded version of the present correction scheme wherein wall effects are ignored, i.e., $\Psi_k^{(i)}=\Phi_{kj}^{(i)}=1$. As listed in Tab. 3.3, for wall distances very close to the wall, such as $\delta_p=0.05$ and 0.5, the unbounded version under predicts the particle velocity with negative errors on the same order of magnitude as the uncorrected scheme. These large errors in the near wall results are due to the overprediction in the computations of the disturbance velocity of the unbounded correction scheme, while particle in practice receives much smaller u_c from the background flow near the no-slip boundary. When particle gets away from the wall, however, the predicted disturbance field using unbounded version becomes more accurate and reduces the errors significantly (see cases at $\delta_p=\infty$).

When wall effects are accounted for in the correction scheme, the asymmetry pattern is captured which results in excellent predictions. For the cases considered, the errors reduce to one order of magnitude smaller values when the wall-modified correction scheme is applied. For example, in case A1, the total error of 91.42% in particle settling velocity predicted by the unbounded correction scheme reduces to 6.03% when wall effects are accounted for. Additionally, for particles travelling far away from the wall wherein the symmetric disturbance field is expected, the wall-modified and unbounded versions of the present correction scheme both yield nearly identical results. This shows the superiority of the former to the latter for general particle-laden flows. Figure 3.7 illustrates the results of these two versions on the particle velocity of case A as a function of time. The erroneous results of the unbounded version for near wall motions is improved by including wall effects in the correction scheme.

The results presented in the previous part were obtained for $Re_p<0.1$, while in the wall-bounded particle-laden flows, typically a wider range of Re_p exists. In this part, the present model is tested for a range of Re_p up to 10 by performing similar computations to the previous part. Table 3.4 lists the studied cases for this part that are similar to case E1 of Tab. 3.3, yet with different Stokes and parti-

Case	δ_p	$\Lambda^{(1)}$	$\Lambda^{(2)}$	$\Lambda^{(3)}$	uncorrected			corrected using unbounded model			corrected using wall-modified model		
					$e^\parallel$	$e^\perp$	e	$e^\parallel$	$e^\perp$	e	$e^\parallel$	$e^\perp$	e
A1	0.05	1.0	1.0	1.0	125.82	0.17	125.82	-86.82	21.42	91.42	5.37	2.23	6.03
A2	0.5	1.0	1.0	1.0	59.16	0.095	59.16	-35.08	1.37	35.12	4.86	0.57	4.91
A3	1.0	1.0	1.0	1.0	103.12	0.073	103.12	-19.67	1.16	19.72	4.29	0.76	4.38
A4	1.5	1.0	1.0	1.0	66.12	0.073	66.12	-13.81	0.66	13.84	4.06	0.46	4.10
A5	2.0	1.0	1.0	1.0	102.96	0.06	102.96	-10.02	0.87	10.08	2.08	0.72	2.24
A6	∞	1.0	1.0	1.0	69.19	0.05	69.19	0.74	0.45	0.95	1.0	0.44	1.14
B1	0.05	5.0	5.0	5.0	745.72	0.54	745.72	-102.6	142.86	212.04	-3.02	13.66	19.50
B2	0.5	5.0	5.0	5.0	437.08	0.28	437.08	-31.02	20.99	42.67	4.51	6.96	11.16
B3	1.0	5.0	5.0	5.0	589.81	0.16	589.8	-22.48	10.12	28.80	-4.17	9.77	17.54
B4	1.5	5.0	5.0	5.0	390.42	0.22	390.42	-10.43	6.02	15.35	4.78	5.58	10.01
B5	2.0	5.0	5.0	5.0	554.19	0.15	554.19	-9.99	8.89	20.14	-0.59	9.08	16.06
B6	∞	5.0	5.0	5.0	353.79	0.2	353.79	0.35	5.01	9.16	0.83	4.85	8.97
C1	0.05	0.1	1.0	0.2	7.91	0.17	7.91	-33.79	2.12	33.87	0.58	0.33	0.67
C2	0.5	0.1	1.0	0.2	5.59	0.25	5.59	-18.12	1.14	18.16	1.03	0.32	1.08
C3	1.0	0.1	1.0	0.2	9.82	0.46	9.83	-11.47	0.78	11.51	1.29	0.53	1.40
C4	1.5	0.1	1.0	0.2	8.93	0.58	8.95	-11.27	0.62	11.29	0.71	0.59	0.93
C5	2.0	0.1	1.0	0.2	11.98	0.77	12.01	-7.55	0.42	7.57	0.55	0.65	0.86
C6	∞	0.1	1.0	0.2	14.88	1.09	14.92	-2.16	0.25	2.19	-1.89	0.25	1.92
D1	0.05	0.5	5.0	1.0	106.87	7.99	107.17	-69.94	3.33	70.02	-3.04	7.25	8.40
D2	0.5	0.5	5.0	1.0	82.44	7.69	82.80	-44.12	1.03	44.15	-12.55	4.7	13.45
D3	1.0	0.5	5.0	1.0	95.70	8.00	96.04	-16.49	1.93	16.64	-4.21	2.72	5.05
D4	1.5	0.5	5.0	1.0	82.49	7.24	82.81	-20.79	1.17	20.84	-9.87	2.14	10.23
D5	2.0	0.5	5.0	1.0	94.04	7.12	94.31	-9.59	0.84	9.64	-0.78	1.58	3.13
D6	∞	0.5	5.0	1.0	79.99	5.95	80.21	-10.84	1.01	10.92	-9.53	0.99	9.63
E1	0.05	0.3	6.0	0.6	42.99	2.14	43.05	-43.24	2.93	43.34	-0.69	1.54	1.71
E2	0.5	0.3	6.0	0.6	50.17	3.78	50.31	-21.67	0.9	21.69	-3.15	1.34	3.45
E3	1.0	0.3	6.0	0.6	49.20	4.28	49.39	-16.29	0.14	16.29	-4.33	1.40	4.58
E4	1.5	0.3	6.0	0.6	48.27	4.34	48.47	-12.23	0.91	12.28	-4.43	1.77	4.88
E5	2.0	0.3	6.0	0.6	56.16	5.08	56.39	-9.27	0.65	9.29	-3.47	1.2	3.68
E6	∞	0.3	6.0	0.6	53.61	4.05	53.77	-5.47	0.23	5.48	-4.41	0.31	4.42
F1	0.05	0.6	12.0	1.2	113.56	8.25	113.86	-50.01	1.61	50.03	-4.82	4.09	6.52
F2	0.5	0.6	12.0	1.2	121.47	11.00	121.97	-19.90	1.18	19.94	-3.06	3.01	4.44
F3	1.0	0.6	12.0	1.2	113.10	9.81	113.53	-12.64	1.51	12.74	-3.03	2.47	4.2
F4	1.5	0.6	12.0	1.2	108.30	8.8	108.66	-10.05	1.25	10.13	-3.48	1.86	4.27
F5	2.0	0.6	12.0	1.2	105.95	8.24	106.27	-8.19	1.01	8.26	-3.28	1.44	3.82
F6	∞	0.6	12.0	1.2	100.45	7.42	100.72	-6.05	0.72	6.10	-4.12	0.90	4.27

Table 3.3: Tabulated are the percentage errors in the simulated velocity of a single particle settling parallel to a wall under gravity and at different normalized wall gaps. Different sets of computations including various types of grid aspect ratio as well as particle diameter to the grid size, $\Lambda^{(i)}$ are studied. For each set, different wall distances of δ_p, is examined to study the error in the settling velocity, $e^\parallel$, drifting velocity, $e^\perp$, and the overall error, e. Flow parameters are kept constant in all cases with Stokes number of St=10 and unbounded particle Reynolds number of Re_p^{Stk}=0.1. The results of the present wall-modified correction scheme is compared with its unbounded counterpart as well as the classical uncorrected point-particle approach.
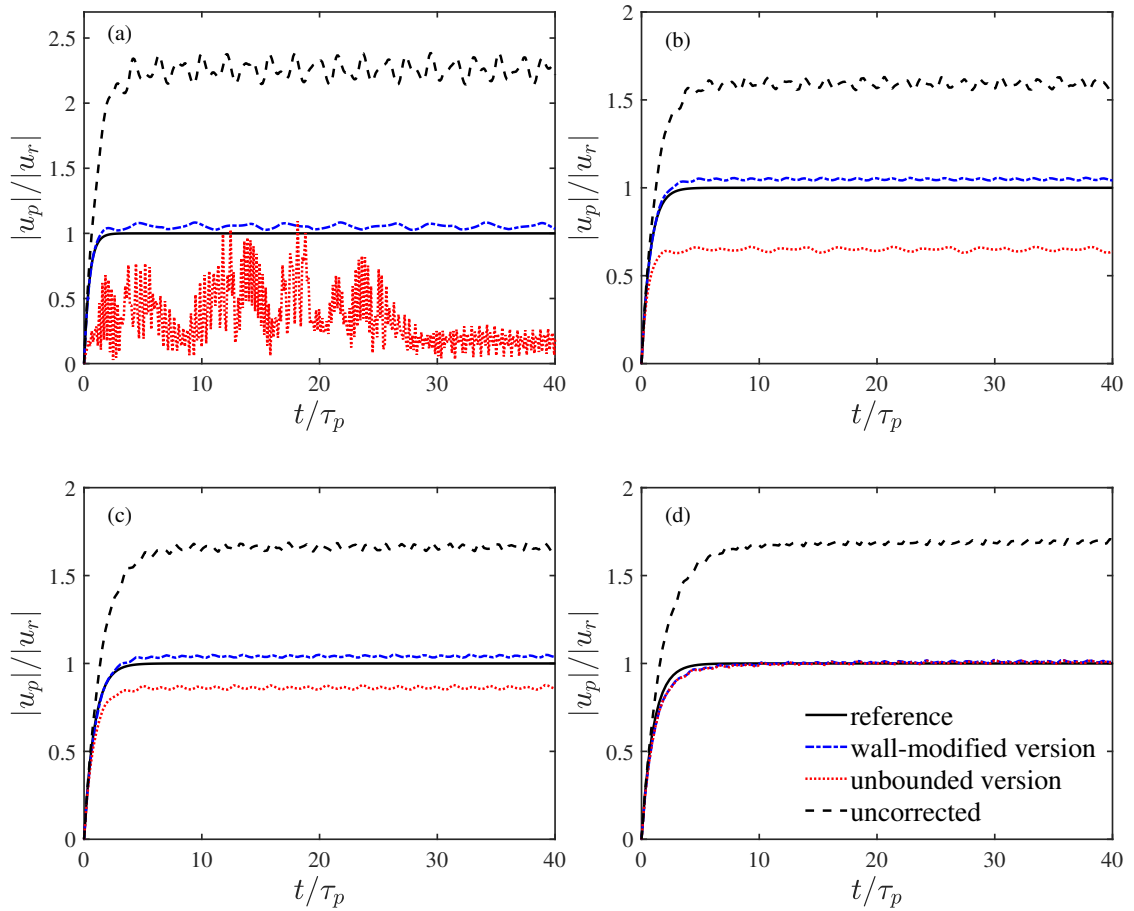
Figure 3.7: Shown are velocity of a particle settling under gravity parallel to a wall at different wall distances of (a): δ_p=0.05, (b): δ_p=0.5, (c): δ_p=1.5 and (d): δ_p=∞. Results of the present scheme with wall-modified version (dash-dotted blue), unbounded version (dotted red) and uncorrected scheme (dashed black) are all compared against the reference velocity (solid black). These results are based on case A of Tab. 3.3.

cle Reynolds numbers. Unlike the previous part, the reported particle Reynolds number here is based on its actual velocity and defined by $Re_p = Re_p^{Stk}/f^{\|}(\delta_p, Re_p)$ which varies from 0.044 to 10. For all cases, settling is performed at $\delta_p = 0.05$ for which the deviation between unbounded and wall-modified correction schemes of the previous part was found to be significant. For studied cases here, the whole terms in Eq. 3.3.18 hold and we use first order forward Euler finite difference scheme to solve Eq. 3.3.8 and obtain its reference velocity as a function of time.

As shown in Tab. 3.4, the error in uncorrected scheme is reduced as Re_p increases which is in line with the observations of the preceding works (Horwitz & Mani, 2018; Balachandar *et al.*, 2019). This is conceptually justified due to the fact that, unlike particles with small Re_p, higher Reynolds number particles move faster and stay less in their own disturbance field created in the previous time step. Although this diminishes the need for the correction, the error of approximately 30% that pertains to the case with $Re_p = 10$ (the largest studied Re_p), is still considerable. As listed in Tab. 3.4, the present wall-modified correction scheme reduces the errors by approximately one order of magnitude for cases with $Re_p < 10$ and results in better predictions compared to the unbounded version wherein the wall effects are ignored.

It should be emphasized that the present model is constructed based on the small Re_p assumption. Although the finite Re_p effects are partially accounted for through the factor C_r (Eq. 3.2.29), a more elaborate formulation is required to improve the accuracy of the model for $Re_p > 10$. For such cases, the assumption of symmetric Stokes solution is not valid anymore and the linear superposition of the perturbations caused by neighbour cells used in the derivation of K_p may be broken, that are left for future investigations. Similar observations were achieved by Horwitz & Mani (2018) wherein they showed that their unbounded correction scheme that was developed based on small Re_p, is still reliable for cases with Re_p of 10 with errors in settling velocity of 10%. Concerning the Stokes number effects, our results show insignificant changes to the prediction of the present model for the studied range of this parameter ($3 < St < 30$).

Case	Re_p	St	uncorrected			corrected using unbounded version			corrected using wall-modified version		
			$e^{\parallel}$	$e^{\perp}$	e	$e^{\parallel}$	$e^{\perp}$	e	$e^{\parallel}$	$e^{\perp}$	e
R1	0.044	3.0	32.94	1.64	32.99	-41.59	2.77	41.68	-3.10	0.77	3.20
R2	0.044	10.0	40.80	2.02	40.85	-41.58	2.84	41.68	-2.74	0.86	2.88
R3	0.044	30.0	61.31	3.09	61.38	-47.91	3.63	48.05	-6.75	1.23	6.87
R4	0.5	3.0	50.95	2.60	51.02	-48.35	3.99	48.52	-4.11	1.43	4.66
R5	0.5	10.0	53.11	2.68	53.18	-49.24	3.74	49.41	-1.86	1.31	2.78
R6	0.5	30.0	52.43	2.62	52.50	-47.14	3.07	47.26	-1.46	1.24	2.11
R7	5.0	3.0	39.62	1.77	39.66	-26.45	2.34	26.58	2.76	1.11	3.18
R8	5.0	10.0	39.77	1.76	39.81	-26.18	2.40	26.31	2.96	1.10	3.23
R9	5.0	30.0	39.90	1.76	39.94	-26.16	2.37	26.27	3.04	1.10	3.24
R10	10.0	3.0	33.56	1.26	33.59	-17.60	2.23	17.77	5.25	0.76	5.31
R11	10.0	10.0	34.06	1.27	34.09	-17.45	2.26	17.60	5.45	0.76	5.50
R12	10.0	30.0	33.92	1.26	33.94	-17.39	2.27	17.54	5.40	0.74	5.45

Table 3.4: The effects of particle Reynolds number, Re_p, and particle Stokes number, St, on the velocity of a single particle settling parallel and close to a wall at δ_p=0.05 are shown. The anisotropic grid resolution of case E from Tab. 3.3 with $\mathbf{\Lambda}$=[0.3, 6.0, 0.6] is employed for all cases. The wall-modified and unbounded versions of the present correction scheme are compared together and against the uncorrected PP approach in terms of the error in settling velocity, $e^{\parallel}$, drifting velocity, $e^{\perp}$ and total velocity, e.

3.3.3   Free falling particle normal to the wall

This section verifies the present model for capturing the disturbance field in the wall-normal motion of particles, as commonly encountered in wall-bounded particle-laden flows. The free falling motion of a particle normal to the wall is considered as a test case for this part. In such scenario, a particle falls under gravity and its drag coefficient increases as it approaches to the wall, owing to the wall lubrication effects. Gondret *et al.* (1999) observed that depending on the particle Stokes number, it could either sit on the wall if $St<20$ or hit the wall and re-bound if $St>20$. To eliminate the particle-wall collision and isolate the particle-fluid interaction only, we perform the first situation wherein the particle is supposed to retard and sit on the wall. Accordingly, the Stokes number of $St=10$ is chosen for all the studied cases of this part.

Brenner (1961) derived an exact solution for the wall adjustment to the drag coefficient of a particle in normal motion to the wall which has small Reynolds number of $Re_p<0.1$. In their work, a corresponding asymptotic solution was also obtained that matches their exact solution for the normalized wall gaps of $\delta_p>1.38$. For $\delta_p<1.38$, Cox & Brenner (1967) achieved an asymptotic solution that combined with the one obtained by Brenner (1961) are used in this work for the wall adjustment drag coefficient of a particle in normal motion toward the wall. This adjustment is expressed as

$$f^{\perp}(\delta_p) = \begin{cases} 1 + \left(\frac{0.562}{1+2\delta_p}\right) & \text{for} \quad \delta_p > 1.38 \quad \text{(Brenner, 1961)} \\ \frac{1}{2\delta_p}\left(1 + 0.4\delta_p \log\left(\frac{1}{2\delta_p}\right) + 1.94\delta_p\right) & \text{for} \quad \delta_p < 1.38 \quad \text{(Cox \& Brenner, 1967)} \end{cases}$$

$$(3.3.22)$$

Figure 3.8 compares these asymptotic solutions to the exact solution of Brenner (1961). Based on the adjustment factor provided by Eq. 3.3.22, the particle equation of motion (Eq. 3.3.13) is solved for the reference velocity using a first order forward Euler finite difference scheme. For all the studied cases, the particle is initially stationary and located at the normalized wall gap of $\delta_p=7$ and falls
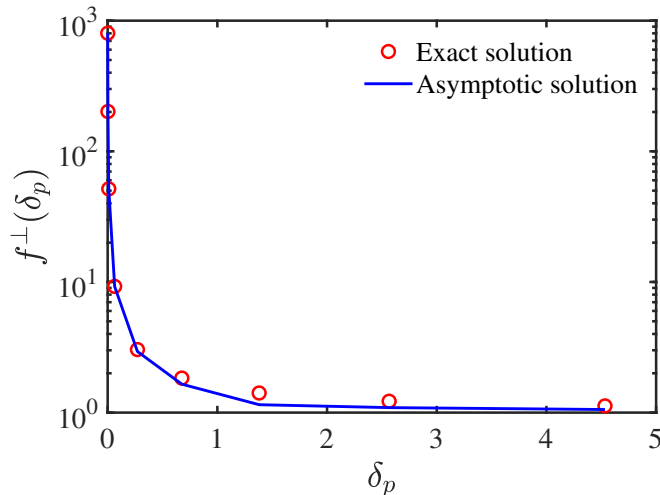
Figure 3.8: Shown is the wall adjustment to the drag coefficient of a particle in wall-normal motion. Exact solution of Brenner (1961) is shown along with the asymptotic solution provided by Brenner (1961) and Cox & Brenner (1967), given in Eq. 3.3.22.

under gravity. Similar to the preceding section, results of the wall-modified and unbounded versions of the present correction scheme are compared with those of the uncorrected approach. Studied cases are listed in Tab. 3.5 that are carried out using both isotropic and anisotropic grids. A range of particle Reynolds number of $0.04 < Re_p < 10$ and Stokes number of $3 < St < 30$ are used for each grid resolution. For each case, the total time that particle requires to reach the normalized wall gap of $\delta_p = 0.5$ is computed and compared against the corresponding reference value, t_{ref}. The deviation of each scheme from the reference is quantified based on the following metric

$$e = \frac{t - t_{ref}}{t_{ref}} \tag{3.3.23}$$

As Tab. 3.5 shows, without correcting the PP approach, the considerable and negative errors for each case imply that particle sees a smaller drag force due to the disturbance created in the background flow, accelerates faster and reaches the wall-gap of interest quicker. However, when the PP is corrected using the

Case	Re_p^{Stk}	St	$\Lambda^{(1)}$	$\Lambda^{(2)}$	$\Lambda^{(3)}$	uncorrected e	corrected using unbounded version e	corrected using wall-modified version e
N1	0.1	3.0	1.0	1.0	1.0	-30.55	32.30	-6.05
N2	0.1	10.0	1.0	1.0	1.0	-24.37	23.86	-4.77
N3	0.1	30.0	1.0	1.0	1.0	-15.09	10.13	-2.79
N4	5.0	10.0	1.0	1.0	1.0	-2.30	0.97	-0.07
N5	10.0	10.0	1.0	1.0	1.0	-1.37	0.62	0.02
N6	0.1	3.0	0.3	6.0	0.6	-9.62	4.95	-2.88
N7	0.1	10.0	0.3	6.0	0.6	-9.61	5.04	-2.75
N8	0.1	30.0	0.3	6.0	0.6	-9.57	4.78	-2.87
N9	5	10.0	0.3	6.0	0.6	-1.80	0.72	-0.24
N10	10	10.0	0.3	6.0	0.6	-0.73	0.52	0.1

Table 3.5: Errors calculated in the prediction of particle's wall-normal motion. Two sets of grid aspect ratio with various particle Reynolds numbers and Stokes numbers are performed. For each case, the error in the time that particle requires to reach the normalized wall gap of δ_p=0.5 is computed based on the wall-modified and unbounded versions of the present correction scheme in comparison with that of the uncorrected scheme.

present wall-modified correction scheme, it reduces the errors and results in better prediction for the particle trajectory and velocity. Although the errors obtained based on the unbounded version of the correction scheme are still better than the uncorrected approach, the superiority of the wall-modified version on other schemes is observed in this case as well.

Figure 3.9 shows the prediction of different schemes on the particle velocity and trajectory of case N2 from Tab. 3.5. The reference velocity used for normalization is based on Eq. 3.3.5 that pertains to the Stokes settling velocity of a particle in an unbounded domain. As illustrated, the wall-modified version of the present model captures quite well the accurate trajectory and velocity of the particle whereas the unbounded scheme hinders the particle settling due to the overprediction in the disturbance field. Results in this part along with the observation of the previous parts underscore the need for accounting for the wall effects in capturing the disturbance field and having a general correction scheme that could be applied to all
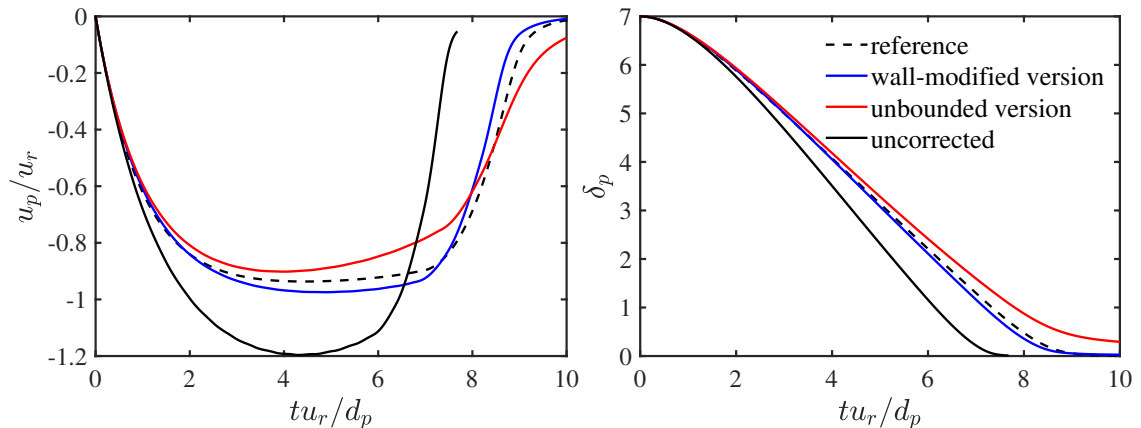
Figure 3.9: Shown are the normalized velocity (left) and normalized wall-gap (right) of a particle settling normal to a wall predicted by the wall-modified and unbounded versions of the present correction scheme. Results are compared with the uncorrected scheme as well as the reference. Results here pertain to the case N2 from Tab. 3.5.

types of particle-laden flows in the presence and absence of no-slip boundaries.

3.4   Conclusion

Modeling two-way coupled Euler-Lagrange (EL) particle-laden flows using point-particle (PP) approach can result in erroneous predictions due to an issue that arises in the calculation of fluid forces acting on the particles. The available closures for force calculations are all based on the undisturbed fluid velocity, which by definition is the fluid velocity not influenced by the presence of particles. In the two-way coupled computations, however, the particle reaction force disturbs the fluid velocity around the particle and using such a disturbed velocity for force calculations in the next time step yields inaccurate inter-phase interactions and wrong predictions. More importantly, depending on whether the particle is travelling near a no-slip boundary or in an unbounded domain, its disturbance in the background flow can be different in terms of shape and strength, and can also be asymmetric.

In this paper, we presented a general correction scheme for EL-PP approaches to recover the undisturbed fluid velocity from the available disturbed field in the presence and absence of the no-slip walls. In the present velocity correction approach, the disturbance created by a particle in a computational cell that carries the particle is obtained by finding the response of the cell (its velocity) to the particle force. Analogous to the motion of a solid object, the disturbance velocity of the computational cell is obtained by treating the computational cell as a solid object that is subjected to the particle force and dragged through the adjacent computational cells (Esmaily & Horwitz, 2018). Knowing these two forces, the disturbance velocity of the cell is solved using a Maxey-Riley equation of motion for the computational cell. The model is general and can be used for (i) unbounded and wall-bounded regimes, (ii) isotropic and anisotropic grid resolutions, (iii) particles bigger than the grid size, (iv) arbitrary interpolation and distribution functions, and (v) flows with finite particle Reynolds number.

An empirical expression was obtained for the drag coefficient of the computational cell ($K_c^{(i)}$) that is applicable for a wide range of grid aspect ratios, typically encountered in the particle-laden turbulent channel flows. The new expression, obtained based on the employed collocated grid arrangement, is a function of the grid size. Just as a slowly moving solid particle in a quiescent fluid influences the near field through Stokes solution, the particle force at a computational cell perturbs the surrounding cells. It was shown that for the employed collocated grid arrangement, Stokes solution normalized by the characteristics length scale of $0.25d_c$ results in accurate predictions for the disturbance field created in the surrounding cells in comparison with the numerical measurements.

Wall effects in the model were taken into account through two different factors; (i) $\Psi_k^{(i)}$ and (ii) $\Phi_{kj}^{(i)}$. The first pertains to the wall modification to the drag coefficient of the computational cell near a no-slip boundary, analogous to the near wall motion of a solid object. Two components for this parameter were obtained for the disturbances created in parallel and wall-normal directions. For isotropic grid, it was shown that the wall adjustment to the drag coefficient of a solid sphere

moving near a no-slip wall, empirically derived by Zeng *et al.* (2009), can be an excellent choice for $\Psi_k^{(i)}$. However, for anisotropic grids owing to their large aspect ratios, this expression does not hold, and a new fitted expression was obtained that covers a wide range of grid sizes and aspect ratios. The second parameter, $\Phi_{kj}^{(i)}$, was introduced to capture the wall effect on the Stokes solution of the computational cell. It was shown that perturbation created at neighbouring cells by a computational cell that is exposed to the particle force differs in shape and strength as the cell becomes closer to a no-slip wall. It was argued that one could directly use the wall-modified Stokes solution instead of its unbounded counterpart, however, due to the complexity and expense embedded in the implementation and solution of the wall-modified version, Stokeslet solution was suggested as the second wall adjustment factor. In that regard, we kept the Stokes solution in the formulation, while its wall effect was accounted for by multiplying this solution by the ratio of the wall-bounded to the unbounded Stokeslet solutions, defined as $\Psi_k^{(i)}$. Our results showed that the choice of this ratio yields in good predictions with small errors.

An unbounded version of the present model can be obtained by ignoring wall effects, i.e., letting $\Psi_k^{(i)}{=}\Phi_{kj}^{(i)}{=}1$ in the formulation, that can be used in particle-laden flows without no-slip boundary conditions. To verify the collocated adjustments made in the formulation, the unbounded version of the scheme was first tested for settling of a particle in an unbounded domain and results were compared with those reported in Esmaily & Horwitz (2018). For the different studied flow and grid parameters, it was shown that the model using the collocated grid arrangement accurately captures the settling velocity of the particle with a few percent errors.

To assess the model for wall-bounded applications, settling of a particle parallel to a no-slip wall was performed at various wall-normal distances. Consistent with the observation of Esmaily & Horwitz (2018), the error in the uncorrected particle velocity was observed to be a function of particle's diameter to the grid size, (d_p/d_c). Correcting the PP approach with the current model, however, cap-

tured the disturbance field at all wall distances and significantly reduced the errors in the predicted particle velocity by accurately recovering the undisturbed field. Furthermore, it was observed that ignoring the wall effects in the formulation for wall-bounded flows, i.e., assuming $\Psi_k^{(i)}=\Phi_{kj}^{(i)}=1$, results in large errors that are in the same order of magnitude of the uncorrected scheme, particularly in the near wall motions. As particle gets away from the wall, however, the effects of wall diminish and the formulation approaches the unbounded version.

Tests performed for a range of $0<Re_p<10$ revealed the fact that the error in the uncorrected settling velocity decreases as Re_p increases, consistent with the observation of Balachandar *et al.* (2019). This is justified due to the fact that particles with large Re_p do not stay in their own disturbance, created in the previous time step, and this alleviates the need for the correction. Nevertheless, the relatively small errors associated with large Re_p cases was still lowered using the present correction scheme.

The last test cases were carried out on the free falling motion of a particle in the wall-normal direction. It was shown that the particle's velocity in the uncorrected scheme is erroneously overpredicted which makes the particle hit the wall earlier than it would in reality. When the PP approach is corrected with the present model, however, it recovers the undisturbed velocity at any wall distance and captures the particle's velocity and trajectory more accurately. Tests performed for this part with different grid configurations and flow parameters showed the superiority of the present model to the uncorrected and unbounded correction schemes.

The present correction scheme is general, cost-efficient and accurate that can be easily implemented in EL-PP packages to study a wide range of particulate flows with and without the no-slip boundaries. We conjecture that this scheme could help improve the investigations and the state-of-the-art of the wall-bounded particle-laden flows wherein the lack of accuracy of the standard uncorrected PP approaches has been widely observed. For such flows, the proposed correction scheme can significantly improve the predictive capability of point-particle method

approaching those of the particle-resolved methods at significantly lower computational cost.

Appendix A. A simplified equation for $\Psi_k^{(i)}$ on isotropic grids

A simplified expression for $\Psi_k^{(i)}$ that is only applicable for isotropic grids is introduced here. The new equation denoted by Ψ_k^{iso} is obtained based on the work of Zeng *et al.* (2009). In their work, an expression using fully resolved direct numerical simulation, was empirically derived for the wall adjustment to the drag coefficient of a solid sphere in parallel motion to a no-slip wall. Our results show that their wall adjustment expression matches our measured values for the wall adjustment to the drag coefficient of isotropic computational cells. Accordingly, the new equation for $\Psi_k^{(i)}$ that is only applicable for isotropic computational cells is introduced based on their empirical expression as

$$\Psi_k^{iso} = \left(1.028 - \frac{0.07}{1 + 4\delta_k^2} - \frac{8}{15} \log \left(\frac{270\delta_k}{135 + 256\delta_k} \right) \right), \qquad (3.4.1)$$

where

$$\delta_k = x_k^{(2)}/(0.5d_c) - 0.5, \qquad (3.4.2)$$

and $x_k^{(2)}$ is the wall-normal distance of the center of the computational cell k, normalized by its equivalent radius of $0.5d_c$. The choice of these two parameters $(x_k^{(2)}$ and $0.5d_c)$ are slightly changed compared to the original formulation of Zeng *et al.* (2009) in order to produce better predictions. It is also imperative to mention that Eq. 3.4.1 covers a wide range of wall distances and approaches unity when the computational cell is sufficiently away from the wall. Figure 3.10 shows the predictions of this equation for both parallel and normal directions compared to the measured values. It should be emphasized that unlike the predictive capability of the equation above for the uniform grid resolutions, it deviates significantly for anisotropic grids with high aspect ratios.
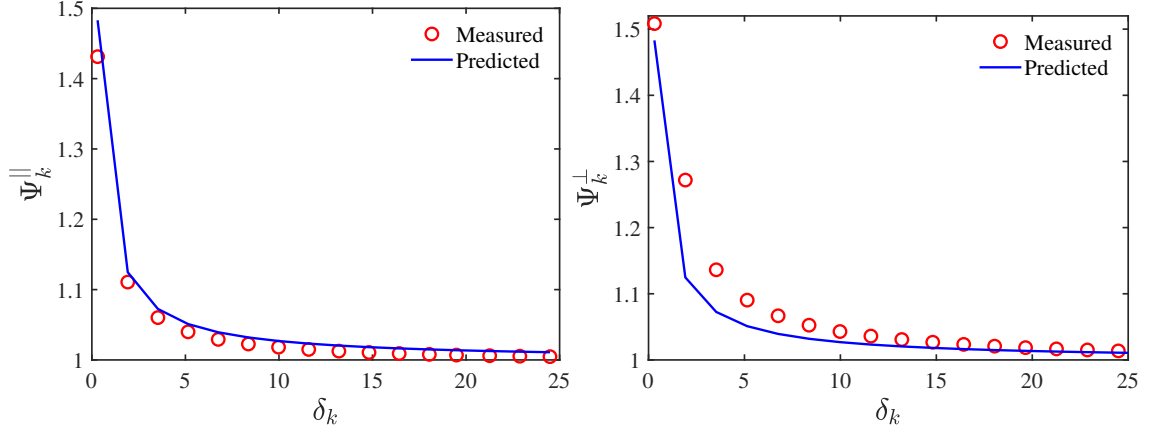
Figure 3.10: Shown are the predictions of Eq. 3.4.1 for the wall adjustment to the drag coefficient of an isotropic computational cell compared to the measured values for parallel (left) and perpendicular (right) forces to the wall.

Appendix B. Stokeslet solutions

In this Appendix, the wall-bounded and unbounded Stokeslet solutions used in the derivation of $\Phi_{kj}^{(i)}$ in section 3.2, are explained in detail. The unbounded Stokeslet solution that is the flow generated by a point force in an unbounded quiescent fluid with dynamic viscosity of μ is expressed as (Blake, 1971)

$$u_{stkl,un}^{(i)} = \frac{F^{(j)}}{8\pi\mu}\left(\frac{\delta_{ij}}{|r_{kj}|} + \frac{r_{kj}^{(i)}r_{kj}^{(j)}}{|r_{kj}|^3}\right) \tag{3.4.3}$$

where

$$r_{kj}^{(i)} = (x_j^{(i)} - x_k^{(i)}), \quad |r_{kj}| = \sqrt{\sum_{i=1}^{3}(r_{kj}^{(i)})^2} \tag{3.4.4}$$

and $u^{(i)}$ is the i component of velocity created at the location of $(x_j^{(1)}, x_j^{(2)}, x_j^{(3)})$ by the point force, $F^{(j)}$, exerted in j direction and located at $(x_k^{(1)}, x_k^{(2)}, x_k^{(3)})$. δ_{ij} is the Kronecker delta which is unity for $i=j$ and zero otherwise. Similar to this, the wall-bounded Stokeslet solution for a point force that is applied near a no-slip

wall is expressed as (Blake, 1971)

$$
\begin{aligned}
u_{stkl,b}^{(i)} =& \frac{F^{(j)}}{8\pi\mu} \left[\left(\frac{\delta_{ij}}{|r_{kj}|} + \frac{r_{kj}^{(i)}r_{kj}^{(j)}}{|r_{kj}|^3} \right) - \left(\frac{\delta_{ij}}{|R_{kj}|} + \frac{R_{kj}^{(i)}R_{kj}^{(j)}}{|R_{kj}|^3} \right) + \right. \\
& \left. 2x_k^{(2)} \left(\delta_{jm}\delta_{ml} - \delta_{j3}\delta_{3l} \right) \frac{\partial}{\partial R_{kj}^{(l)}} \left(\frac{x_k^{(2)}R_{kj}^{(i)}}{|R_{kj}|^3} - \left(\frac{\delta_{i3}}{|R_{kj}|} + \frac{R_{kj}^{(i)}R_{kj}^{(2)}}{|R_{kj}|^3} \right) \right) \right]
\end{aligned}
\tag{3.4.5}
$$

where

$$
R_{kj}^{(i)} = \begin{cases} r_{kj}^{(i)}, & i = 1, 3 \\ r_{kj}^{(2)} + 2x_k^{(2)}, & i = 2 \end{cases} \quad , \quad |R_{kj}| = \sqrt{\sum_{i=1}^{3} (R_{kj}^{(i)})^2}
\tag{3.4.6}
$$

and $x_k^{(2)}$ is the wall distance at which the force is applied. The rest of parameters are similar to those of the unbounded Stokeslet solution.

Acknowledgments

Chapter 4   Modeling a particle-laden turbulent channel flow using a corrected point-particle approach

Pedram Pakseresht and Sourabh V. Apte

Abstract

Modeling sediment-laden turbulent channel flow using Euler-Lagrange (EL) point-particle (PP) approach is challenging due to the disturbance created by the relatively large size particles in the near wall region of the channel. The accuracy of this approach depends on accurate estimation of fluid forces acting on the particles which are in turn based on the *undisturbed* fluid velocity at the location of particle. When the fluid and particle phases are two-way coupled, the particle reaction force disturbs the background flow at the location of particle, and using such a disturbed fluid velocity for force computations results in erroneous predictions. Such a disturbance becomes larger as the particles gets bigger than the local grid size, a scenario that typically happens in the near wall region of the highly turbulent channel flows. In this paper, large eddy simulations (LES) coupled with PP approach is employed for modeling the sediment-turbulence interactions in a horizontal channel flow with Re_τ=583.3. In order to accurately obtain the fluid forces acting on the particles, the PP approach is corrected by the recently developed correction scheme of Pakseresht et al. (JCP, 2020). It is shown that the standard PP approach (uncorrected), wherein the undisturbed fluid velocity is not available, fails in capturing the experimental observations with flow remains nearly unchanged of presence of particles. However, when this approach is corrected and undisturbed fluid velocity is recovered, most of the experimental observations are achieved, revealing the importance of the undisturbed field in force computations. An increase in the friction velocity due to presence of particles is captured in consistent with the corresponding experiment. Damping in the outer layer as well as enhancing in the inner layer of the fluid mean velocity are both captured with the corrected PP approach. In line with the experimental observations, enhancing in the turbulence intensities as well as sweep and ejection events in the near wall region are all observed, as well.

4.1   Introduction

Interaction of small particles with wall-bounded turbulence is widely encountered in environmental phenomena such as sediment transport within rivers as well as industrial applications, e.g., pneumatic transport of granular materials, among others. Accurate modeling of these flows is of paramount importance in order to better understand the interaction of particle and turbulence, make robust predictions without performing expensive experiments and ultimately optimize the devices wherein these flows occur. Of specific interest is the interaction of sediment particles with turbulence in a horizontal channel flow wherein a unique configuration exists. Due to the normal alignment of the gravity to the flow direction, inertial sediments tend to accumulate near the bed with relative large size compared to the local fluid length scale. Point-Particle (PP) approach has received much attention in modeling of this flow due to its affordability, simplicity and partial accuracy. In this approach, the fluid phase is solved using an Eulerian framework while sediment are treated as Lagrangian subgrid points in the flow and tracked following the Newton's second law of motion based on the available closures for the fluid forces acting on the point-particles.

For two-way coupled regimes, wherein each phase affects the other Elghobashi (1991), the effect of particles on the carrier phase is modelled by applying the particle reaction force to the background flow through a momentum source term. Using such a simplified point force in modelling the inter-phase interactions, however, could result in some inaccuracies in capturing the experimental observations of particle-laden turbulent channel flows.

Coleman (1986) and Lyn (1988) observed a damping in the whole fluid velocity profile due to the presence of particles in the flow. They explained two mechanisms for such a damping; (i) roughness at the bed as well as (ii) local interaction of suspended particles and turbulence. Rogers & Eaton (1991) found similar flattening in the fluid mean velocity of a particle-laden flow over a flat plat due to the interaction of particles and turbulence near the wall. Best *et al.* (1997) and Muste & Patel (1997) observed the same reduction and claimed that this damping

is only attributed to the roughness at the bed. Following their work, Kulick *et al.* (1994) found insignificant effect of particles on the mean fluid flow in a vertical channel flow. In such a configuration, the gravity is align with the main flow and the near wall concentration of particles is lower than the horizontal channel flows, hence reduction in the interaction of particles and near wall turbulence. Kaftori *et al.* (1995) observed that such a reduction in the fluid mean velocity can only occur when there is a significant concentration of neutrally buoyant particles near the wall.

In addition to these observations, Kiger & Pan (2002) showed that in the presence of dilute loading of particles ($O(10^{-4})$) in a horizontal turbulent channel flow, the dimensional fluid mean velocity is slightly damped in the outer layer. However, unlike the outer layer, a 7% increase in the friction velocity (the velocity representing the near wall shear stress) was observed in their work. Although they did not directly measure flow quantities near the bed, such an increase in their calculated friction velocity could indirectly reveal a potential enhancement in their near wall fluid velocity. Following these observations, they argued that the damping phenomenon becomes stronger when such a larger friction velocity is used for normalizing the fluid velocity profile. In other words, they claimed that the main reason behind damping is attributed to the increase in friction velocity than the local interaction of particles and turbulence in the outer layer.

Righetti & Romano (2004) investigated the effect of sediment particles on the dynamics and structure of the near wall region of a highly turbulent channel flow ($Re_\tau=730\sim811$) with measurement down to viscous sublayer ($y^+=3$). In their work and consistent with the preceding works, damping in the outer layer was observed while for the first time, they reported an enhancement in the near wall fluid velocity profile. Their experiments with different size particles showed dependency of the damping on the size of particles with large size particles affecting the fluid phase stronger. In line with Kiger & Pan (2002), the higher friction velocity due to presence of particles was also observed in their measurements. Muste *et al.* (2009) showed that the damping effect is more related to the interaction

of particles and the near wall turbulence structure than the equivalent roughness created by particles at the wall. This observation was found by increasing the flow Reynolds number so that no streak is formed on the bed which obviates the possibility of the effect of roughness to the damping. They also reported that friction velocity remains almost identical as the clear case, although that contradicts their observation on the enhancing mean fluid velocity in the near wall region. Beside from these observations on the mean fluid velocity across the boundary layer, a difference between velocity of particle and fluid phases is observed in most of the experimental works with fluid to be faster in the outer layer while slower in the inner layer. Similar observations were obtained in the work of Yu *et al.* (2014).

Turbulence modulation due to presence of particles has also been observed. Kulick *et al.* (1994) found a damping in the vertical velocity fluctuations in vertical turbulent channel flow. Kiger & Pan (2002); Righetti & Romano (2004) observed a damping in both streamwise and vertical fluctuations of the outer layer whereas the latter found an increase in the corresponding parameters in the near wall region. In addition, Righetti & Romano (2004) revealed an enhancing in the near wall turbulence coherent structure and found that the main mechanism in such a damping and enhancing is mostly related to the burst and sweep events in the near wall, the mechanism that was later on observed by Muste *et al.* (2009) as well.

Whether these experimental observations can be captured by the PP approach has been an open question in the field. McLaughlin (1989) and Pedinotti *et al.* (1992) were the first groups that performed particle-laden vertical channel flow using Direct Numerical Simulation (DNS) one-way coupled with the PP approach to investigate the segregation and preferential concentration of particles in a vertical turbulent channel flow. Rouson & Eaton (2001) used the same formulation to perform the experimental work of Kulick *et al.* (1994) with a smaller Reynolds number to investigate the preferential concentration and evaluate statistics that were unavailable experimentally. Wang & Squires (1996) performed Large Eddy Simulations (LES) one-way coupled with PP approach to predict the experimental work of Kulick *et al.* (1994). Streamwise particle fluctuation relative to the fluid

was correctly predicted in their work. Observations on the preferential concentration were also similar to those found in the experiments of Fessler *et al.* (1994). Yamamoto *et al.* (2001) carried out LES two-way coupled with PP approach to simulate the particle-turbulence interactions in a vertical channel flow with $Re_\tau = 644$. Several discrepancies between their numerical results and the experiment of Kulick *et al.* (1994) are observed. Profile of particle mean velocity is over predicted in their computations while better results for the stremawise and wall-normal particle velocity fluctuations were observed. Concerning the fluid phase, the damping in the streamwise fluid velocity fluctuation was not predicted for large size particles, and they found that the turbulence modification is only captured for small Stokes number particles. Segura (2004) in a comprehensive study using LES and PP approach performed computations corresponding to the experiments of Paris & Eaton (2001) and Benson & Eaton (2003) for smooth and rough walls, respectively. For dilute regimes, they showed that LES coupled one-way with PP was able to adequately predict particle motion for smooth wall boundary conditions, however, there were some discrepancy for rough walls. For higher mass loading, they showed that two-way coupled LES with PP was not able to accurately predict turbulence modifications measured in the corresponding experiment. They found that artificially increasing the mass loading of particles by a factor of 10 could show minimal change in the gas-phase mean streamwise velocity and predict the non-uniform turbulence attenuation and the Reynolds stress profile measured by the experiment. Vreman (2007) performed simulations of a vertical air-solid pipe flow using DNS coupled with PP, some of the discrepancies reported in Yamamoto *et al.* (2001) between numerical results and experiment were also revealed in their work.

In nearly all predictions using PP approach, some discrepancy has been observed in comparison to the experimental works. Of importance is the prediction of horizontal channel flow due its unique configuration. In such a flow, depending on flow Reynolds number and the near wall grid resolution, particles become relatively large in that region and the point-particle assumption does not hold any-

more Eaton (2009); Balachandar (2009). Therefore, using such a simplified model results in some inaccuracies in capturing the experimental observations (Segura, 2004; Eaton, 2009; Pakseresht *et al.*, 2017).

One source of inaccuracy is that, the fluid phase equations in this approach are solved for the entire flow field including the volume occupied by the particles, and the mass displacement of the particles is not taken into account. Several works have shown the considerable effects of this displacement and have argued that this effect should be included in addition to the point-particle force (Ferrante & Elghobashi, 2004; Apte *et al.*, 2008; Cihonski *et al.*, 2013; Pakseresht & Apte, 2019*b*), in order to improve the predictions. The other one, is that the accuracy of PP in predicting the fluid forces acting on the particles can decay when the two phases are two-way coupled. Typical force closure models require the *undisturbed* fluid velocity for accurate estimation of fluid forces, however, in the two-way coupled regimes, the particle reaction force disturbs the background flow and results in a disturbed fluid velocity at the location of particles. Then, using such a disturbed field for force computations produces erroneous results and large deviations in the inter-phase predictions. As the size of particle becomes bigger, these deviations in the prediction and inter-phase interactions become larger too.

Recently, efforts have been made in order to improve the accuracy of the standard PP approach by retrieving the undisturbed fluid velocity from the available disturbed field. Gualtieri *et al.* (2015) regularized the PP approach for the unbounded flows by deriving analytical equations to remove the self-induced velocity disturbance created by the particles. Their approach requires considerable computational resources to resolve the stencil over which the particle force is distributed using a Gaussian filter function. Horwitz & Mani (2016, 2018) originated a method to obtain the undisturbed velocity based on the enhanced curvature in the disturbed velocity field for particle Reynolds numbers of Re_p<10.0. A C-field library data was built using reverse engineering technique that should be added to the current EL-PP approaches for recovering the undisturbed velocity. Although their model showed excellent agreement in the predictions of particle settling velocity

and decaying isotropic turbulence (Mehrabadi *et al.*, 2018), it is limited to (i) the isotropic computational grids, (ii) particle-laden flows with particles with the maximum size of the grid ($\Lambda=d_p/\Delta$) of O(1), where Δ is the grid size and d_p particle diameter, and (iii) the unbounded flows. Ireland & Desjardins (2017) derived an analytical expression for recovering the undisturbed velocity in unbounded flows based on the steady state Stokes solution that was derived as the solution of a feedback force distributed to the background flow using a Gaussian smoothening. Although their model accounts for the mass displacement of the particles, it is limited to unbounded flows with small Re_p.

Esmaily & Horwitz (2018) originated a correction scheme in which each computational cell is treated as a solid object that is immersed in the fluid. Each computational cell that is subjected to the two-way coupling force is dragged at a velocity that is identical to the disturbance created by the particle. In their physics-based model, the disturbance of each computational cell created by the particle is obtained by solving the Lagrangian motion of the cell concurrently with the equation of motion of the particle. Although their model was devised to handle (i) relatively large size particles ($\Lambda>1$), (ii) isotropic and anisotropic grids, (iii) flows with finite Re_p, and (iv) arbitrary interpolation and distribution functions, it is limited to unbounded flows. Balachandar *et al.* (2019) developed a model based on analytical and empirical equations that correct the PP approach for modelling particle-laden flows with a wide range of particle Reynolds number, $Re_p<200$. Although their model account for the mass displacement of the particles (similar to Ireland & Desjardins (2017)) and is built for a wide range of particle Reynolds number, they are derived for unbounded flows only, and based on a specific filter function; namely Gaussian, that limits their applicability.

Battista *et al.* (2019) extended their regularized PP scheme for a turbulent particle-laden pipe flow and Pakseresht *et al.* (2019) and Horwitz *et al.* (2019) underscored the need for correction schemes that are applicable for wall-bounded flows. In a generic model, Pakseresht *et al.* (2020) developed a correction scheme that is applicable for unbounded and wall-bounded flows. It handles highly skewed

anisotropic grids that is used for high resolution of turbulent channel flows near the wall.

In this work, the recently developed correction scheme by Pakseresht *et al.* (2020) is employed to regularize the PP approach to perform a sediment-laden horizontal turbulent channel flow. We show that the standard PP approach fails in capturing the particle-turbulence interactions that are experimentally observed in the literature. It will be shown that, however, when the PP is corrected and the undisturbed fluid velocity is recovered at the location of particles, most of the experimental observations, such as damping in the outer layer as well as enhancing in the inner layer are accurately captured.

The rest of paper is arranged as follows. Section 4.2 describes the mathematical formulation of EL point-particle approach modified with the mass displacement effects of particles. The correction scheme for PP approach is explained briefly. Section 4.3 validates the LES and the employed grid resolution for a clear turbulent channel flow without particles. Results are compared with the experiment of Kiger & Pan (2002) and DNS of Moser *et al.* (1999). In the same section, LES coupled with PP approach with and without the correction scheme are performed to simulate the horizontal turbulent particulate channel flow of Kiger & Pan (2002). With such a comparison, the need for correcting the standard PP approaches in modeling particle-laden channel flows is highlighted. Section 4.4 concludes the paper with final remarks and summary of the work.

4.2 Methodology

An EL approach is used wherein the continuity and momentum equations for the fluid phase are solved on a fixed Eulerian framework using LES formulation while particles are assumed subgird and modelled as Lagrangian points. Particles are tracked using Newton's second law of motion and the fluid forces acting on the particles are computed based on the available closures. The inter-phase interactions are performed using two different approaches: (i) the standard two-way coupling and (ii) the volumetric two-way coupling (Pakseresht & Apte, 2019b). In the first,

two phases are coupled through the momentum exchange reaction forces while in the latter, in addition to the momentum exchange force, the mass displacement effects of particles on the carrier phase are taken into account. In order to accurately predict the particle reaction forces to the background flow, our recently developed correction scheme (Pakseresht *et al.*, 2020) is employed to recover the undisturbed fluid velocity at the location of particles. Details of different approaches and the corresponding formulations are given in the following section.

4.2.1   Carrier phase formulation

In order to account for the mass displacement effects of particles on the background flow, volume-averaged continuity and momentum equations are used for the fluid phase as expressed in Eq. 4.2.1 and 4.2.2, respectively (Anderson & Jackson, 1967; Dukowicz, 1980; Joseph *et al.*, 1990)

$$\frac{\partial}{\partial t}(\rho_f \theta_f) + \frac{\partial}{\partial x_j}(\rho_f \theta_f u_j) = 0, \tag{4.2.1}$$

$$\frac{\partial}{\partial t}\left(\rho_f \theta_f u_i\right) + \frac{\partial}{\partial x_j}\left(\rho_f \theta_f u_i u_j\right) =$$
$$-\frac{\partial P}{\partial x_i} + \frac{\partial}{\partial x_j}\left[2\mu_f\left(\frac{1}{2}\left(\frac{\partial u_i}{\partial x_j} + \frac{\partial u_j}{\partial x_i}\right) - \frac{1}{3}\delta_{ij}\frac{\partial u_k}{\partial x_k}\right)\right] + \rho_f \theta_f g_i + F_{i,p \rightarrow f}, \tag{4.2.2}$$

where g_i is the gravitational acceleration, μ_f, ρ_f, θ_f, and u_f are dynamic viscosity, density, volume fraction, and velocity of the fluid phase, respectively. Fluid volume fraction in each computational cell is calculated as $\theta_f{=}1{-}\theta_p$, where θ_p corresponds to the volume fraction of particles occupying the computational cell. The particle force per unit volume, $F_{i,p \rightarrow f}^t$, is the particle reaction force that is equal and opposite to the particle surface forces exerting by the fluid phase on them. Since the zero-Mach number variable density equations account for the volumetric displacement of the carrier phase as well as point-particle forces, thus the interphase coupling is named volumetric two-way coupling (V2W). Setting $\theta_f{=}1$ in the

Abbreviation	Coupling type	$F_{i,p\to f}$	Volumetric displacement effects
S2W	Standard two-way coupling	Yes	No
V2W	Volumetric two-way coupling	Yes	Yes

Table 4.1: Terminologies used for different couplings in EL formulations.

above formulation, the standard two-way coupling (S2W) is recalled in which the displacement effects are neglected. Table 4.1 describes these inter-phase couplings. It should be noted that throughout the paper the two-way terminology is only used for the inter-phase coupling, while in the computations reported here, the inter-particle collision is employed, as well.

For LES, the equations above are spatially filtered using Favre (density-weighted) averaging (e.g., $\overline{\rho\theta u}=\overline{\rho\theta}\widetilde{u}$) where the filtering operation is denoted by an overbar and density-weighted Favre averaging by a tilde (Moin & Apte, 2006). The governing equations for LES of particle-laden turbulent flow then become

$$\frac{\partial}{\partial t}\left(\overline{\rho_f\theta_f}\right) + \frac{\partial}{\partial x_j}\left(\overline{\rho_f\theta_f}\widetilde{u}_j\right) = 0 \tag{4.2.3}$$

$$\frac{\partial}{\partial t}\left(\overline{\rho_f\theta_f}\widetilde{u}_i\right) + \frac{\partial}{\partial x_j}\left(\overline{\rho_f\theta_f}\widetilde{u}_i\widetilde{u}_j\right) = -\frac{\partial\widetilde{P}}{\partial x_i} + \frac{\partial}{\partial x_j}\left(2\overline{\mu_f\theta_f}\widetilde{S}_{ij}\right) - \frac{\partial q_{ij}^{r,vol}}{\partial x_j} + \overline{\rho_f\theta_f}g_i + F_{i,p\to f} \tag{4.2.4}$$

where,

$$\widetilde{S}_{ij} = \frac{1}{2}\left(\frac{\partial\widetilde{u}_i}{\partial x_j} + \frac{\partial\widetilde{u}_j}{\partial x_i}\right) - \frac{1}{3}\delta_{ij}\frac{\partial\widetilde{u}_k}{\partial x_k}. \tag{4.2.5}$$

Here, $\overline{\rho_f\theta_f}$ is the filtered density modified by local volume fraction. $\widetilde{u}_i$, $\widetilde{P}$ and $\widetilde{S}_{ij}$ are the Favre-averaged velocity field, pressure and rate of strain respectively.

The additional term in the momentum equation containing $q_{ij}^{r,vol}$, represents the subgrid-scale stress in the volumetric coupling formulation and is modeled

using the dynamic Smagorinsky (Germano *et al.*, 1991; Moin *et al.*, 1991). The unclosed term in Eq. 4.2.4 is modeled using the gradient-diffusion hypothesis with eddy-viscosity as

$$q_{ij}^{r,vol} = \overline{\rho_f \theta_f}(\widetilde{u_i}\widetilde{u_j} - \widetilde{u_i u_j}) = 2\mu_t \widetilde{S}_{ij} - \frac{1}{3}\overline{\rho_f \theta_f}q^2 \delta_{ij} \qquad (4.2.6)$$

where $\frac{1}{2}\rho_f\theta_f q^2$ is the subgrid kinetic energy and the eddy viscosity, μ_t, is calculated as

$$\mu_t = C_\mu \overline{\rho_f \theta_f}\Delta^2 |\widetilde{S}| \quad ; \quad \Delta = V_{cv}^{1/3} \quad ; |\widetilde{S}| = \left(\widetilde{S}_{ij}\widetilde{S}_{ij}\right)^{1/2} \qquad (4.2.7)$$

where V_{cv} is the volume of the cell and the model constant, C_μ, is evaluated dynamically (Pierce & Moin, 1998). Note that in the volumetric coupling formulation the subgrid effects of fluid displacement are also present in the subgrid model. For the standard two-way coupling the subgrid-scale stress term, $q_{ij}^{r,2w}$, is simply obtained by setting $\theta_f=1$ in the Eq. 4.2.6-4.2.7.

4.2.2   Dispersed phase formulation

Point-particle approach (Maxey & Riley, 1983) is used for the motion of particles wherein particles are assumed subgrid and tracked using the Newton's second law of motion as

$$\frac{d\mathbf{x}_p}{dt} = \mathbf{u}_p \qquad (4.2.8)$$

$$m_p \frac{d\mathbf{u}_p}{dt} = \mathbf{F}_g + \mathbf{F}_{pr} + \mathbf{F}_d + \mathbf{F}_{l,Saff} + \mathbf{F}_{am} \qquad (4.2.9)$$

where $\mathbf{x}_p$ and $\mathbf{u}_p$ are the respective position and velocity vector of each individual particle with mass of m_p. Equation 4.2.9 shows all possible forces such as weight, $\mathbf{F}_g$, dynamic pressure-gradient force, $\mathbf{F}_{pr}$, shear induced lift force (Saffman, 1965), $\mathbf{F}_{l,Saff}$, as well as added mass force (Auton, 1983), $\mathbf{F}_{am}$. It has been observed that the Basset history force does not remarkably affect the motion of particles in the

presence of the steady drag force (Maxey & Riley, 1983; Bagchi & Balachandar, 2003); therefore, this force is excluded in this study. All aforementioned forces are given as follows

$$\mathbf{F}_g = (\rho_p - \overline{\rho_f})\vartheta_p \mathbf{g} \quad ; \quad g = -9.81 m/s^2 \tag{4.2.10}$$

$$\mathbf{F}_{pr} = -\vartheta_p \nabla \overline{P}_{f|p} \tag{4.2.11}$$

$$\mathbf{F}_{l,Saff} = m_p C_l \frac{\overline{\rho_f}}{\rho_p} \left(\widetilde{\mathbf{u}}_{f|p} - \mathbf{u}_p \right) \times (\nabla \times \widetilde{\mathbf{u}}_f)_{|p} \quad ; \quad C_l = \frac{1.61 \times 6}{\pi d_p} \sqrt{\frac{\mu_f}{\overline{\rho_f}} |\, (\nabla \times \widetilde{\mathbf{u}}_f)_{|p}\, |} \tag{4.2.12}$$

$$\mathbf{F}_{am} = m_p C_{am} \frac{\overline{\rho_f}}{\rho_p} \left(\frac{D\widetilde{\mathbf{u}}_{f|p}}{Dt} - \frac{d\mathbf{u}_p}{dt} \right) \quad ; \quad C_{am} = 0.5 \tag{4.2.13}$$

$$\mathbf{F}_d = m_p \frac{C_d}{\tau_p} \left(\widetilde{\mathbf{u}}_{f|p} - \mathbf{u}_p \right) ; \quad C_d = (1 + 0.15 Re_p^{0.687}) \tag{4.2.14}$$

where, $\tau_p = (\rho_p d_p^2)/(18\mu_f)$ and $Re_p = \overline{\rho_f}|\mathbf{u}_{rel}|d_p/\mu_f$ are the respective particle relaxation time and particle Reynolds number. D/Dt and d/dt denote the time derivative following the fluid (material derivative) and particle phases, respectively (Maxey & Riley, 1983).

The closures used for force calculations of Eq. 4.2.9 rely on the undisturbed fluid velocity at the location of particles. This is by definition the velocity that is not influenced by the presence of particles, which is no longer available when two phases are two-way coupled. In order to obtain such a velocity, our recently developed correction scheme (Pakseresht et al., 2020) is employed to recover the undisturbed velocity from the available disturbed flow flied. It should also be mentioned that the undisturbed velocity has to be based on the unfiltered velocity field, while in LES simulations, this is the filtered fluid velocity that is available. Although particles are indirectly affected by the SGS model used for fluid phase,
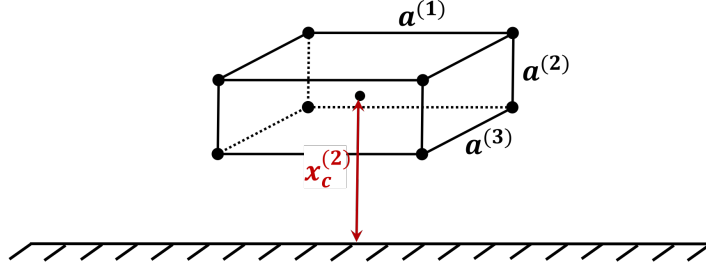
Figure 4.1: A computational cell with dimensions of $[a^{(1)}, a^{(2)}, a^{(3)}]$ in streamwise, wall-normal and spanwise directions, respectively. The cell is located at a wall-normal distance of $x_c^{(2)}$.

further investigations on the need for particle SGS model (Marchioli, 2017) is left for future investigations.

4.2.3 Correction scheme

The undisturbed fluid velocity at the location of a particle is recovered by obtaining the response of the computational cell to the particle force located in the cell. The velocity generated by this force is the disturbance created in the cell and that is the missing velocity in the standard PP approaches. If accurately predicted, this velocity recovers the undisturbed fluid velocity from the available disturbed field. The newly developed general correction scheme of Pakseresht *et al.* (2020) is used that captures the disturbance created by particles in the presence and absence of no-slip walls. In such a generic model, the disturbance is predicted by modelling the computational cell with dimensions of $[a^{(1)}, a^{(2)}, a^{(3)}]$ (see Fig. 4.1) as a solid object that is subjected to the particle force and is dragged through the surrounding computational cells. Using a Maxey-Riley equation of motion for the computational cell, the disturbance created by the particle's force, $u_c^{(i)}$, is computed as

$$\frac{3}{2}m_c\frac{du_c^{(i)}}{dt} = -3\pi\mu d_c K_t^{(i)} u_c^{(i)} - F^{(i)}, \tag{4.2.15}$$

where $d_c = \sqrt[3]{(6/\pi)a^{(1)}a^{(2)}a^{(3)}}$ is the volume-equivalent diameter of the computational cell with mass of $m_c = (\pi/6)\rho_f d_c^3$. The term on the left hand side expresses the unsteady effect of the force on the computational velocity wherein the prefactor $3/2$ captures the added mass effect. The first term on the right hand side of the equation, $3\pi\mu d_c K_t^{(i)} u_c^{(i)}$, is the Stokes drag force acting on the computational cell by its surrounding cells wherein the relative velocity is $-u_c^{(i)}$ as the ambient flow for the disturbance field is at rest. The adjustment to the Stokes drag is expressed by the factor $K_t^{(i)}$ as,

$$K_t^{(i)} = \frac{K_c^{(i)} C_r}{K_p^{(i)} C_t^{(i)}}. \qquad (4.2.16)$$

Here, $K_c^{(i)}$ accounts for non-sphericity of the computational cell while $K_p^{(i)}$ accounts for wall effects as well as the interpolation and distribution functions. The factor C_r accounts for the non-linear finite force effects whereas $C_t^{(i)}$ considers the limited exposure time of the particle force to the computational cell. These physics-based factors are defined and explained in the following.

Geometric correction factor, $K_c^{(i)}$

The geometric correction factor, $K_c^{(i)}$, accounts for non-sphericity of the computational cell and depends on its size and aspect ratio as

$$
\begin{aligned}
K_c^{(i)} = 0.1705 \exp &\left[(\Gamma_{max}^{(i)})^{-0.4005} (\Gamma_{min}^{(i)})^{0.06408} \right] (\Gamma_{max}^{(i)})^{0.7058} (\Gamma_{min}^{(i)})^{-0.452} \\
&+ \ln \left[(\Gamma_{max}^{(i)})^{-0.03746} (\Gamma_{min}^{(i)})^{0.2049} \right] (\Gamma_{max}^{(i)})^{0.355} (\Gamma_{min}^{(i)})^{0.05338},
\end{aligned} \qquad (4.2.17)
$$

where

$$\Gamma_{max}^{(i)} = \max\left\{ \frac{a^{(j)}}{a^{(i)}}, \frac{a^{(k)}}{a^{(i)}} \right\}, \quad \Gamma_{min}^{(i)} = \min\left\{ \frac{a^{(j)}}{a^{(i)}}, \frac{a^{(k)}}{a^{(i)}} \right\}; \quad j, k \neq i. \qquad (4.2.18)$$
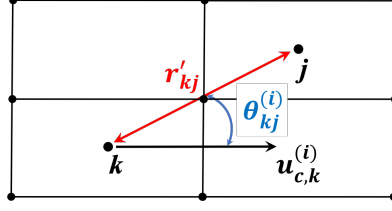
Figure 4.2: Schematic of computational cell k that is disturbed by a small force and has disturbance velocity of $u_{c,k}^{(i)}$ which perturbs the adjacent computational cells through the modelled Stokes solution. r_{kj}' is the normalized distance between cell k and j with polar angle of $\theta_{kj}^{(i)}$ between the line passing through these cells and i direction.

Wall effects and interpolation effects, $K_p^{(i)}$

The factor $K_p^{(i)}$ accounts for the wall effects on the disturbance field as well as the choice of arbitrary interpolation and distribution functions typically employed in the point-particle approach. This correction factor is analytically derived and expressed as

$$K_p^{(i)} = \sum_{j=1}^{n_j} \left[\gamma_j \sum_{k=1}^{n_k} \left[\frac{\alpha_{kj}^{(i)} \beta_k \Phi_{kj}^{(i)}}{\Psi_k^{(i)}} \right] \right] \qquad (4.2.19)$$

wherein, γ_j and β_k are the interpolation and distribution coefficients pertain to the surrounding computational cells of j and k, respectively. n_j is the number of computational cells from which the fluid properties are interpolated to the particle's location, while n_k denotes the total number of adjacent cells to which the particle's force is distributed. Parameter $\alpha_{kj}^{(i)}$ is the Stokes solution that models the perturbation induced at cell j by the disturbance created at cell k as

$$\alpha_{kj}^{(i)} = \frac{3}{4} r_{kj}'^{-1} \left(1 + cos^2 \theta_{kj}^{(i)} \right) + \frac{1}{4} r_{kj}'^{-3} \left(1 - 3cos^2 \theta_{kj}^{(i)} \right), \qquad (4.2.20)$$

where $\theta_{kj}^{(i)}$ is the polar angle between the line passing through the computational cells k and j and the i direction and r_{kj}' is the distance between these two cells normalized by the characteristic length of the computational cell, $0.25d_c$ (see Fig.

4.2). Wall effects are accounted for through the correction factors of $\Psi_k^{(i)}$ and $\Phi_{kj}^{(i)}$. The first one is the wall adjustment to the geometric correction factor of $K_c^{(i)}$ as expressed below

$$\Psi_k^{(i)} = 1 + \frac{A^{(i)}}{1 + B^{(i)} h_k^{(i)}}, \tag{4.2.21}$$

where $h_{c,k}^{(i)}$ is the normalized wall distance of the center of the computational cell k obtained by

$$h_{c,k}^{(i)} = \begin{cases} \frac{x_c^{(2)}}{a^{(i)}}, & \text{i=1,3} \\ \frac{x_c^{(2)}}{a^{(1)}}, & \text{i=2} \end{cases} \tag{4.2.22}$$

with $x_c^{(2)}$ being the dimensional wall distance of the computational cell (see Fig.4.1), and $A^{(i)}$ and $B^{(i)}$ are wall-distance dependent coefficients given as,

$$A^{(i)} = \begin{cases} \dfrac{\ln\left(26.31\frac{a^{(3)}}{a^{(1)}}\right)}{\left(0.05761+5.373\left(\frac{a^{(2)}}{a^{(1)}}\right)^{1.057}\right)}, & i = 1 \\[4mm] \dfrac{\ln\left(14.04\frac{a^{(3)}}{a^{(1)}}\right)}{\left(0.06608+5.14\left(\frac{a^{(2)}}{a^{(1)}}\right)^{1.592}\right)}, & i = 2 \\[4mm] \dfrac{\ln\left(26.31\frac{a^{(1)}}{a^{(3)}}\right)}{\left(0.05761+5.373\left(\frac{a^{(2)}}{a^{(3)}}\right)^{1.057}\right)}, & i = 3 \end{cases} \tag{4.2.23}$$

$$B^{(i)} = \begin{cases} \dfrac{\exp\left(-0.02873\frac{a^{(3)}}{a^{(1)}}\right)}{\left(0.00008+0.5601\left(\frac{a^{(2)}}{a^{(1)}}\right)^{1.894}\right)}, & i = 1 \\[4mm] \dfrac{\exp\left(-1.252\frac{a^{(3)}}{a^{(1)}}\right)}{\left(0.01354+3.688\left(\frac{a^{(2)}}{a^{(1)}}\right)^{2.202}\right)}, & i = 2 \\[4mm] \dfrac{\exp\left(-0.02873\frac{a^{(1)}}{a^{(3)}}\right)}{\left(0.00008+0.5601\left(\frac{a^{(2)}}{a^{(3)}}\right)^{1.894}\right)}, & i = 3 \end{cases} \tag{4.2.24}$$

The second parameter, $\Phi_{kj}^{(i)}$, accounts for the wall effects on the Stokes solution and is analytically derived as

$$\Phi_{kj}^{(i)} = 1 - \left[\frac{\frac{1}{|R_{kj}|} + \frac{(R_{kj}^{(i)})^2}{|R_{kj}|^3} + \frac{2x_k^{(2)} f_{kj}^{(i)}}{|R_{kj}|^6}}{\frac{1}{|r_{kj}|} + \frac{(r_{kj}^{(i)})^2}{|r_{kj}|^3}} \right], \tag{4.2.25}$$

where,

$$f_{kj}^{(i)} = (-1)^i \left(x_k^{(2)} |R_{kj}|^3 - 3|R_{kj}|(R_{kj}^{(i)})^2 x_k^{(2)} - |R_{kj}|^3 R_{kj}^{(2)} + 3|R_{kj}|(R_{kj}^{(i)})^2 R_{kj}^{(2)} \right) \tag{4.2.26}$$

$$r_{kj}^{(i)} = (x_j^{(i)} - x_k^{(i)}), \quad |r_{kj}| = \sqrt{\sum_{i=1}^{3} (r_{kj}^{(i)})^2} \tag{4.2.27}$$

$$R_{kj}^{(i)} = \begin{cases} r_{kj}^{(i)}, & i = 1, 3 \\ r_{kj}^{(2)} + 2x_k^{(2)}, & i = 2 \end{cases}, \quad |R_{kj}| = \sqrt{\sum_{i=1}^{3} (R_{kj}^{(i)})^2} \tag{4.2.28}$$

and $x_j^{(i)}$ and $x_k^{(i)}$ are the i coordinate of the computational cell j and k, respectively.

Correction for the finite Reynolds number, C_r

The Stokes drag used in Eq. 4.2.15 is only valid for disturbances created with zero Reynolds number. To account for the higher Reynolds number effects, a Schiller-Naumann correction factor, analogous to the finite Reynolds number adjustment to the Stokes drag of a sphere (Clift *et al.*, 2005),

$$C_r = 1 + 0.15 Re_c^{0.687} \tag{4.2.29}$$

is used, where $Re_c = u_c d_c / \nu$ is defined as the Reynolds number of the computational cell based on its diameter and disturbance velocity.

Correction for the finite exposure time, $C_t^{(i)}$

A particle moving in the computational cell spends a limited time within that cell and disturbs it for a finite time. The correction factor of $C_t^{(i)}$ accounts for this finite exposure time of the particle to the computational cell and expressed as below

$$C_t^{(i)} = 1 - \frac{\tau_c^{(i)}}{\Delta t^{(i)}} \left(1 - \exp\left(-\frac{\Delta t^{(i)}}{\tau_c^{(i)}} \right) \right),$$ (4.2.30)

where,

$$\Delta t^{(i)} = \frac{a^{(i)}}{|u_p^{(i)}|} \quad \text{and} \quad \tau_c^{(i)} = \frac{d_c^2}{12\nu K_c^{(i)}},$$ (4.2.31)

where $\tau_c^{(i)}$ and $\Delta t^{(i)}$ are respectively the computational cell relaxation time and the particle residence time in i direction of the computational cell, respectively.

4.2.4 Collision modeling

Inter-particle and wall-particle collisions play crucial roles in dynamics of the turbulent channel flows in addition to the inter-phase momentum coupling. In order to model the collision in a physically realistic way, soft–sphere Discrete Element Model (DEM) based on work of Cundall & Strack (1979) is employed here. Collision force, $\mathbf{F}_{cl,ij}$, generated by two particles undergoing collision is modeled by considering the overlap between particle-particle as a linear-damper system with spring constant (stiffness parameter), k_{cl}, and damping constant, η_{cl}, as

$$\mathbf{F}_{cl,ij} = \begin{cases} -k_{cl}\delta_{ij}\mathbf{n}_{ij} - \eta_{cl}\mathbf{u}_{ij} & \text{for:} |\Delta\mathbf{x}_{ij}| < 0.5\,(d_{p,i} + d_{p,j}) + \alpha \\ 0 & \text{Otherwise} \end{cases}$$ (4.2.32)

where,

$$\delta_{ij} = 0.5\,(d_{p,i} + d_{p,j}) - |\mathbf{x}_{p,i} - \mathbf{x}_{p,j}|, \tag{4.2.33}$$

and $\Delta\mathbf{x}_{ij}{=}\mathbf{x}_{p,i}{-}\mathbf{x}_{p,j}$, $\mathbf{u}_{ij}{=}\mathbf{u}_{p,i}{-}\mathbf{u}_{p,j}$ and $\mathbf{n}_{ij}$ is the normal vector between two particles of i and j with position, diameter and velocity of $\mathbf{x}_p$, d_p and $\mathbf{u}_p$, respectively. Also, α is the radius of influence adjusted linearly as a function of collision CFL number in line with Capecelatro & Desjardins (2013). The damping parameter, η_{cl}, is computed as (Patankar & Joseph, 2001b)

$$\eta_{cl} = \frac{-2\ln(e)\,\sqrt{m_{ij}k_{cl}}}{\sqrt{\pi^2 + \ln^2(e)}}, \tag{4.2.34}$$

where restitution coefficient, e, is taken to be 0.65 in line with Finn et $al.$ (2016) and $m_{ij}{=}m_i m_j/(m_i{+}m_j)$ is the reduced mass of colliding particles.

The stiffness parameter could be calculated directly from the Young's and shear modulus of a material (Tsuji et $al.$, 1992); however, this would result in small collision events and expensive EL simulations. In order to avoid this, lower values are commonly employed in the presence of dominant drag force. For the computations of the current work, the stiffness parameter is chosen based on the work of (Finn et $al.$, 2016) wherein extensive test cases were performed to obtain the proper collision parameters for the flow properties similar to the studied case here.

4.2.5   Numerical algorithm

The variable density zero-Mach number equations presented above are solved using a pressure-based, second-order, fractional time stepping scheme on a collocated grid arrangement. Details on this numerical method can be found in Finn et $al.$ (2011); Shams et $al.$ (2011). In this scheme, the velocity, pressure and volume fraction of the fluid phase are stored at the centroid of the control volumes. Using the disturbance field, u_c, from previous time step, the undisturbed fluid velocity at the location of particles is recovered and the particle forces are computed based on this velocity. Particles are then advanced using a forward Euler approximation with

subcycling within each flow time step (Δt_f) in order to resolve their time scale (Δt_p). Point-particle forces are applied back to the cells in which they are located, and the undisturbed velocity for the next time step is explicitly computed using a froward Euler scheme. Knowing the new location of particles, the volume fraction for both phases are computed and stored at the cell centres. Given the volume fraction variations, the eddy viscosity, μ_t, is modified based on these variations through $\overline{\rho_f \theta_f}$ in order to account for their effects in the subgrid scales (Eq. 4.2.7). Knowing the volume fraction of each cell as well as particle reaction forces, the cell-centred velocities, $\overline{\rho_f \theta_f \widetilde{u}_i}$, are advanced by solving the momentum equation as a predictor step. The predicted velocities are interpolated to the faces and then projected to satisfy the continuity constraint. Projection yields the pressure potential at the cell centres, and its gradient is used to correct the cell and face-normal velocities. It should be mentioned that for disturbance field, initial value of zero is set as particles do not perturb the background flow before injection into the flow. For interpolation and distribution processes, a trilinear function is employed wherein two computational cells in the immediate distance to the particle's center are used in each direction.

4.3   Results

The numerical scheme described above without the correction scheme has been extensively applied to and validated for different flows (Shams *et al.*, 2011; Finn *et al.*, 2011; Cihonski *et al.*, 2013; Pakseresht *et al.*, 2014, 2015, 2016; Finn *et al.*, 2016; Pakseresht *et al.*, 2017; He *et al.*, 2018; Pakseresht & Apte, 2019*b*). In addition, the present correction scheme has also been validated for some canonical test cases of a settling particle in the presence and absence of the no-slip boundaries (Pakseresht *et al.*, 2020). In this work, we first validate the numerical scheme for a clear turbulent channel flow and results are compared against the experimental work of Kiger & Pan (2002) as well as the Direct Numerical Simulation (DNS) of Moser *et al.* (1999). Once the scheme is validated for a clear flow, the corresponding experimental particle-laden turbulent channel flow of Kiger & Pan (2002) is

simulated using the LES coupled with PP approach. Results with and without the correction scheme on the PP approach are compared together to identify the need for such a correction in two-way coupled EL-PP approaches.

4.3.1 Numerical simulation setup

The turbulent channel flow is simulated using a Cartesian structured grid in a rectangular computational domain. Periodic boundary condition is employed for the streamwise and spanwise directions whereas the no-slip boundary condition is enforced for the wall-normal direction. Flow parameters are chosen based on the experimental work of Kiger & Pan (2002) with Reynolds number of Re_τ=583.33 that is defined based on the friction velocity of the unladen case, u_τ=2.8$\times 10^{-2} m/s$, and the channel half-width of δ=0.02m. Moser *et al.* (1999) provided a reference for the domain size and grid resolution for DNS of turbulent channel flows at different Reynolds numbers. For the LES computations, we use their advised DNS domain size based on our studied Reynolds number. For the grid resolution, however, a coarser spacing (nearly half of the DNS) is chosen that was found to sufficiently reproduce the flow statistics. The employed grid resolution and the domain size are provided in Tab.4.2 with the corresponding DNS values from Moser *et al.* (1999). In this table, L_x, L_y and L_z are the respective domain size in streamwise, wall-normal and spanwise directions, while N_x, N_y and N_z denote the number of grids in the corresponding directions. Although the Reynolds number used in our LES computations is slightly smaller than the corresponding DNS, we conjecture that this difference does not make significant changes on the results and its effect is minimal. Uniform grid resolution is used for both streamwise and spanwise directions whereas a non-uniform spacing with stretching toward the center of the channel is utilized for the wall-normal direction. With this configuration, the first grid is put at y^+<1 to ensure that LES sufficiently resolves the viscous sublayer.

For all cases, the parabolic velocity profile for the laminar channel flow is initially prescribed with an imposed noise on top, in order to trigger the turbulent flow. For deriving the flow in the periodic domain, a body force is required, that

Simulation	Re_τ	L_x	L_y	L_z	$N_x \times N_y \times N_z$	Δx^+	Δz^+	Δy_c^+
DNS	587.19	$2\pi\delta$	2δ	$\pi\delta$	$384 \times 257 \times 384$	9.7	4.8	7.2
LES	583.33	$2\pi\delta$	2δ	$\pi\delta$	$192 \times 128 \times 192$	19.09	9.95	20.64

Table 4.2: Domain size and grid resolution employed in the LES simulations. The corresponding DNS values from Moser *et al.* (1999) is also provided.

is typically enforced based on either (i) constant mass flow rate or (ii) constant pressure gradient. In this work, the former is used which applies a volumetric force to the entire domain to ensure that the mass flow rate is kept constant at each time step. Once conditions become stable, wall-normal profile of the results are collected based on time-averaging as well as homogeneous averaging in the streamwise and spanwise directions. For particle-laden cases, after flow has become statistically stable, particles are randomly injected into the domain and once the new condition is stable, then the corresponding results are gathered. Total number of particles required for the injection is calculated based on the given volume loading, α_v, particle's diameter, d_p, (see Tab. 4.5) and the domain volume as

$$N_P = \frac{6\alpha_v L_x L_y L_z}{\pi d_P^3} \tag{4.3.1}$$

Throughout the paper, results are normalized with the characteristic scales in the wall units. Friction velocity, $u_\tau = \sqrt{\tau_w/\rho_f}$, and characteristic length of $\mu/(\rho u_\tau)$ are used for normalizing the respective velocities and lengths. Since u_τ varies among the cases, therefore, for each case, its computed value from that case is employed.

4.3.2   Unladen turbulent channel flow

The unladen turbulent channel flow corresponding to the experimental work of Kiger & Pan (2002) with the flow parameters listed in Tab. 4.4 is performed in this part as a validation study. Figure 4.3 shows wall-normal profile of the LES results

Unladen channel flow	$u_\tau (cm.s^{-1})$
DNS	2.8
PIV	2.8
LES	2.8

Table 4.3: Friction velocity computed based on LES of unladen turbulent channel flow. The corresponding DNS value by Moser *et al.* (1999) and PIV by Kiger & Pan (2002) are provided, as well.

on the mean velocity, streamwise r.m.s., wall-normal r.m.s. and Reynolds shear stress in comparison with the experiment as well as the DNS of Moser *et al.* (1999). A good agreement with both DNS results and the experiment is achieved for the mean and streamwise r.m.s. velocities. However, for Reynolds shear stress as well as the wall-normal r.m.s. velocity, a deviation in the experimental data from both LES and DNS is noticeable that could be justified due to the uncertainty of the experiment. Overall, the LES results obtained for the unladen turbulent channel flow validate our numerical scheme and ensure the sufficiency of the employed grid resolution for the particle-laden simulations of the next part. In addition, as listed in Tab. 4.3, the computed friction velocity in LES agrees quite well with the corresponding values by DNS and PIV.

Parameter	value
Fluid density, ρ_f $(kg.m^{-3})$	998
Fluid viscosity, μ $(Pa.s)$	0.95808×10^{-3}
Channel half-width, δ (m)	0.02
Friction velocity, u_τ $(m.s^{-1})$	2.8×10^{-2}
Bulk velocity, U_b $(m.s^{-1})$	0.5202
Reynolds number based on friction velocity, $Re_\tau = \rho u_\tau \delta / \mu$	583.33
Reynolds number based on bulk velocity, $Re_b = \rho U_b \delta / \mu$	10837.5

Table 4.4: Flow parameters for unladen turbulent channel flow simulations.
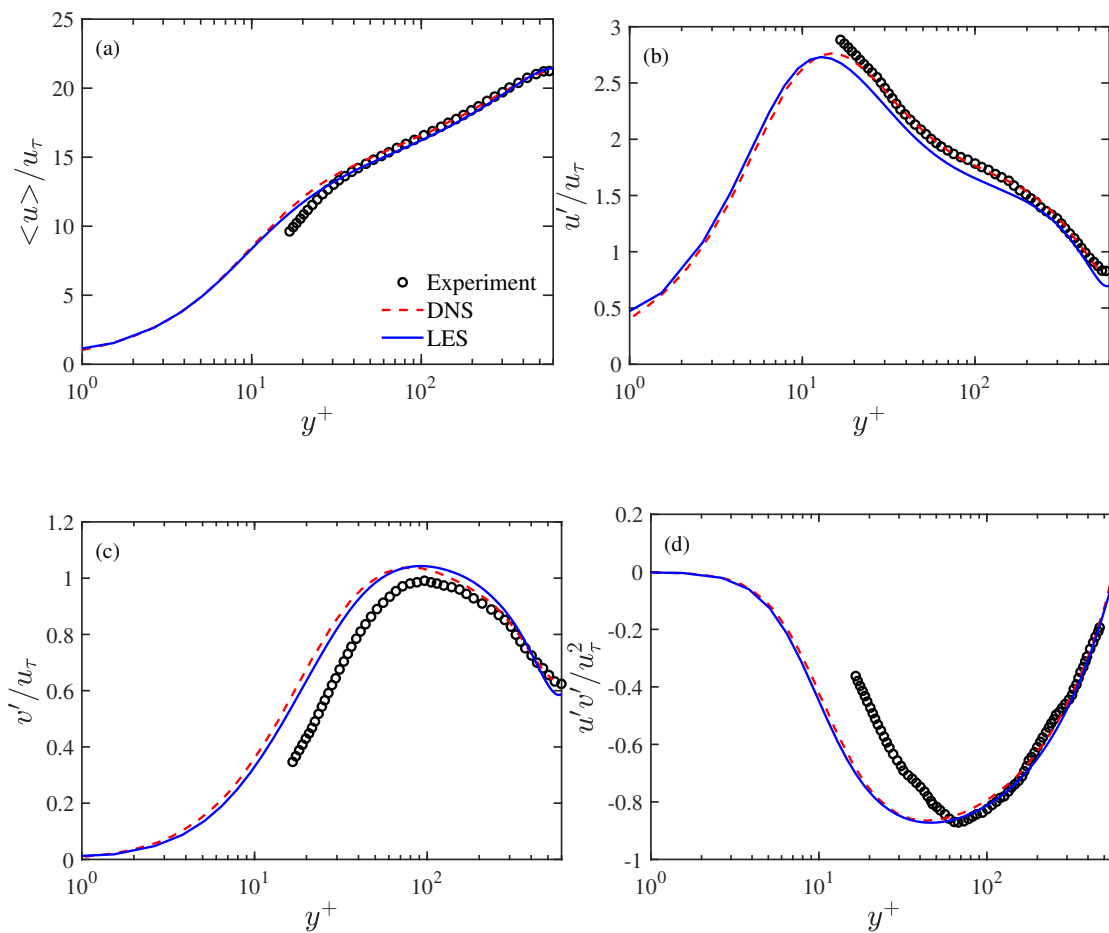
Figure 4.3: Comparison of LES results with DNS of Moser *et al.* (1999) as well as experimental PIV data of Kiger & Pan (2002). Shown are (a) Mean velocity, (b) streamwise r.m.s. velocity, (c) wall-normal r.m.s. velocity, and (d) Reynolds shear stress.

Parameter	value
Particle diameter, d_p (μm)	195
Particle density, ρ_p $(kg.m^{-3})$	2600
Average volume loading, α_v	2.27×10^{-4}
Average mass loading, α_m	6×10^{-4}
Particle Stokes relaxation time, $\tau_p=\rho_p d_p^2/18\mu$ (ms)	5.73
Bulk Stokes number, $St_b=\tau_p U_b/h$	0.15
Wall Stokes number, $St_\tau=\tau_p \rho u_\tau^2/\mu$	5.37

Table 4.5: Particle parameters for particle-laden turbulent channel flow simulations.

Particle-laden channel flow	$u_\tau(cm.s^{-1})$
PIV	2.99
Uncorrected LES-PP	2.8
Corrected LES-PP	2.98

Table 4.6: Friction velocity computed based on laden LES simulations with and without the correction scheme. The corresponding DNS value by Moser *et al.* (1999) and PIV value by Kiger & Pan (2002) are also provided.

4.3.3 Particle-laden turbulent channel flow

In this part, particle-laden turbulent channel flow is simulated using LES coupled with PP approach. Particles with diameter of d_p=200 and density of ρ_p=2600 (see Tab. 4.5) are injected into the already stationary unladen turbulent channel flow with Re_τ=583.33. Results with and without the correction scheme on the PP formulation are compared against the corresponding experimental work of Kiger & Pan (2002). To the best of our knowledge, no DNS data is available for such a high turbulent particle-laden channel flow, therefore, we only compare our LES results with the corresponding experiment. In order to drive the flow in laden cases, we use the same mass flow rate as the unladen case, consistent with the procedure employed in the experiment.

It is imperative to note that the predictions with and without the mass displacement effect of particles show nearly identical results, revealing the fact that the standrad and volumetric couplings almost produce similar results. This can be justified when the current study is compared with that of Pakseresht & Apte (2019b) wherein they found that for particle-laden jet flows with volume loadings of or greater than 5%, the displacement effect tends to become important. In the current channel flow, the maximum concentration of 3% occurring near the wall (that is smaller than their threshold) could justify the potential reason behind that. Although for lighter-than-fluid bubble-laden flows, Ferrante & Elghobashi (2004, 2005) observed that the displacement effect makes significant changes for a similar configuration, for the studied heaver-than-fluid particles of the current wok, no difference between these two formulations was observed. Therefore, for the rest of this paper, we only use the standard two-way coupling wherein the spatio-temporal variations of the local fluid volume fraction are ignored, and the inter-phase interactions are only enforced through the particle reaction force.

As the first step, the friction velocity of each case is computed and compared with that of the experiment. As listed in Tab. 4.6, an increase in this parameter is experimentally observed due to the presence of particles in the flow. Such an increase in the near wall dynamics is reasonably well predicted using the corrected PP approach. However, the uncorrected PP fails in capturing that enhancement and nearly produces the similar friction velocity as the unladen case. The increase in friction velocity reveals an enhancement in the near wall dynamics that is in line with the work of Righetti & Romano (2004) wherein measurements were performed down to $y^+=1$ and such an enhancement in both mean and r.m.s. velocities of the fluid phase was observed. In their work, this enhancement was speculated to be due to the rolling and sliding of particles near the wall which would generate a slip-like boundary condition. Based on the present observation here using the correction scheme, however, it can be argued that such an enhancement is mostly attributed to the particles' reaction force than their rotation as in our numerical scheme the effect of particles' rotation on the background flow is not explicitly enforced.

Further insight into the effect of the corrected PP on the flow is obtained by looking at the statistics of the flow such as mean, r.m.s., as well as quadrant analysis, as explained in detail below.

Mean velocity

The effect of particles on the mean velocity is investigated in this part. Figure 4.4 shows the dimensional and non-dimensional mean velocities of both phases computed based on the present LES-PP and compared with the corresponding experiment. Results with and without the correction scheme are depicted. It can be be inferred from the experiment that a slight damping in the fluid mean velocity of the laden case is noticeable in comparison with its unladen counterpart. However, the damping becomes more noticeable in the normalized velocities, owing to the larger friction velocity measured in the laden case. Similar observation is shown in our corrected PP results while the uncorrected PP fails in capturing any effect of particles on the fluid mean velocity. This shows that using the undisturbed fluid velocity in force computations increases the fluid forces acting on the particles as well as the particle reaction forces, hence stronger inter-phase coupling and more influence on the background flow. Ignoring such a correction and using the disturbed fluid velocity, however, produces weak inter-phase interactions that do not alter the flow and results in nearly identical unladen fluid velocity with no damping effect. Concerning the particle phase mean velocity, reasonable agreement is observed based on both approaches with slight underprediction in the results of the corrected PP scheme. The difference between two schemes could potentially lie in the range of accuracy of the correction scheme as well as the uncertainty of the experiment.

The mechanism behind damping and enhancing in the respective outer and inner layers can be related to the velocity difference between the phases. As shown in Fig. 4.5, there is a lag in particle velocity compared to the fluid phase in the outer layer. Particles with lower velocity in this region push back the flow, hence damping in the fluid mean velocity. In the near wall region, however, particles
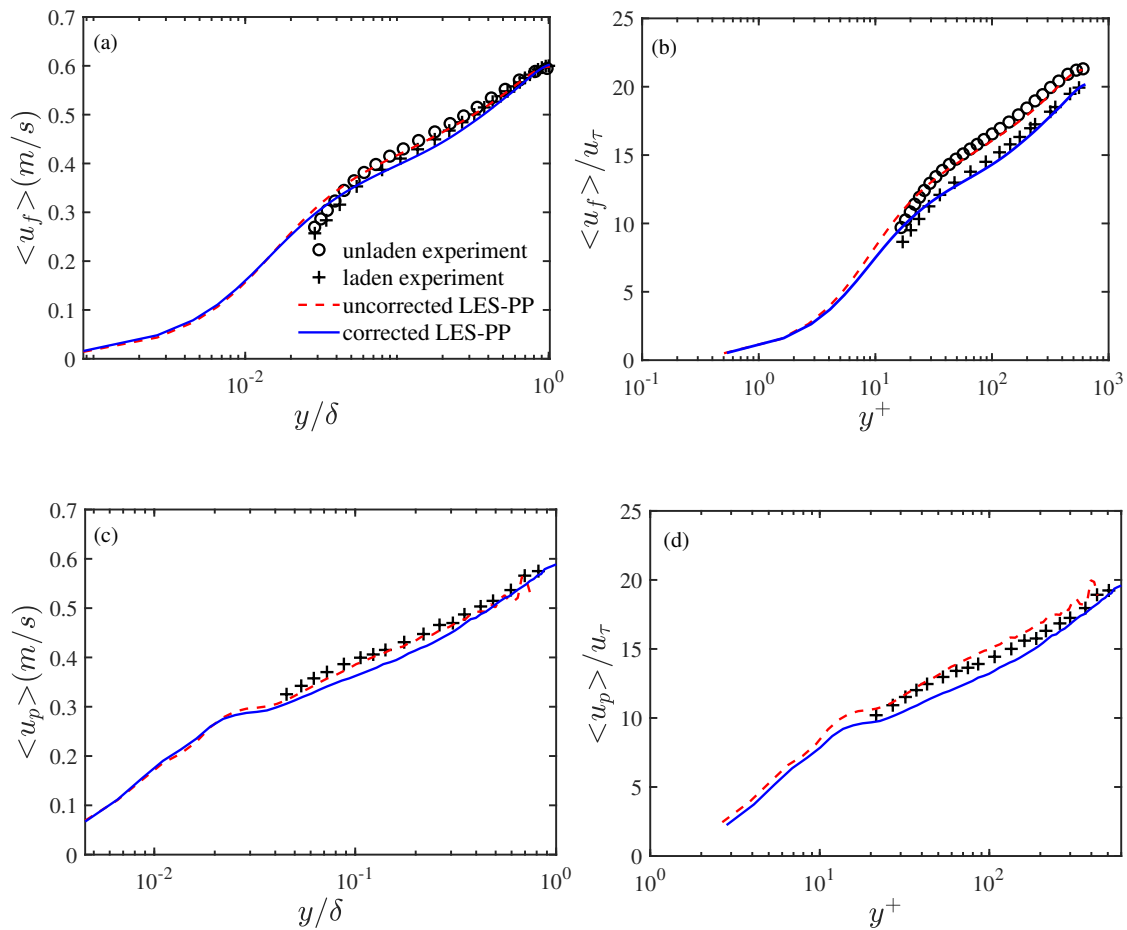
Figure 4.4: Shown are mean velocities of the fluid (a and b) and particle (c and d) phases in comparison with the corresponding experiment of Kiger & Pan (2002). Both dimensional and non-dimensional velocities are plotted for each phase.
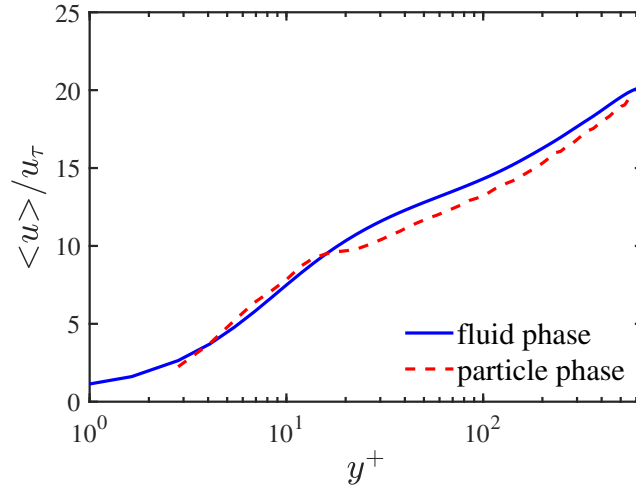
Figure 4.5: Mean velocity of both phases across the channel, predicted by the corrected PP.

have higher velocity than the fluid phase and this could potentially enhance the velocity of the fluid phase. The predicted lag and lead in the particle velocity profile in the respective outer and inner layers are consistent with the observation of experimental works.

Turbulence intensities

In this part, the effect of particles on the turbulence intensities of the flow is considered. Normalized streamwise and wall-normal fluid velocity fluctuations are shown in Fig. 4.6. Results with and without the correction scheme are compared to the corresponding experiment. For sake of comparison, the unladen results by LES are shown as well. It is important to mention that the experimental data is only available for $y^+>10$ as near wall region was not measured in their work, however, we qualitatively compare the results of this part with the experiment of Righetti & Romano (2004) for the near wall region. As implied by Fig. 4.6, without correcting the PP approach, particles do not affect the streamwise fluid velocity fluctuation and results are almost the same as the unladen case, in line

with the prediction of the fluid mean velocity. However, when the PP is corrected, the shape and structure of the turbulence intensity in the outer layer matches that of the experimental data, although slight overprediction is noticeable. Concerning the near wall region, an increase is observed compared to the unladen case which is not captured by the uncorrected PP. Such an enhancing in the inner layer is in consistent with the observations of Righetti & Romano (2004). Regarding the wall-normal turbulence intensity, the uncorrected PP produces some enhancing near the wall which become much stronger when this approach is corrected. Overprediction in the outer layer of channel is also observed for this direction when the corrected scheme is used. The overprediction in the turbulence intensities could be justified due to some reasons. First, Pakseresht *et al.* (2020) showed that even though the correction scheme reduces the error to one order of magnitude smaller values, it still produces few percent errors. Second, particles near the wall experience higher relative velocity, hence higher particle Reynolds number ($Re_p\sim10$). For such a case, the correction scheme needs further adjustments to accurately capture the Re_p effect. Overall, results here show that the corrected PP approach is able to capture the enhancement in the dynamics of the near wall region, however, better experimental measurements are required for this region for the sake of comparison.

Near wall turbulence structure

In order to better study the effects of particles on the damping and enhancing observations, a quadrant analysis of the Reynolds stress is performed in this part (Lu & Willmarth, 1973). The average contribution to the Reynolds stress of the ith quadrant on the plane forming by streamwise and wall-normal components of fluid velocity fluctuation ($u'v'$) is evaluated as

$$Q_i = \lim_{T\to\infty} \frac{1}{T_i} \int_0^T u'v'_{i(t)}dt, \quad i = (1,2,3,4), \tag{4.3.2}$$

where $u'v'_{i(t)}$ is the contribution of the Reynolds stress to the ith quadrant, T_i is the time spent within each quadrant itself and T is the total average time. Figure 4.7
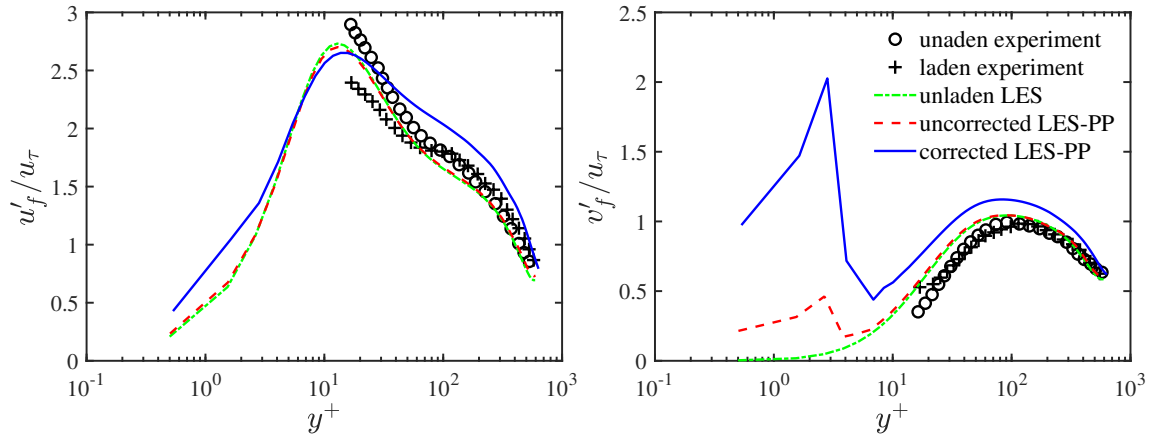
Figure 4.6: streamwise and wall-normal components of r.m.s. velocity for fluid phase. LES-PP results with and without the correction scheme are compared with the corresponding experiment. The unladen LES results are shown as well.

shows each of the quadrant for the fluid phase. Results based on the corrected and uncorrected PP approach are compared against the unladen case. For this part, there is no available experimental data from Kiger & Pan (2002), however, the corresponding parameters of Righetti & Romano (2004) are qualitatively compared with the predicted results. As illustrated, for all quadrants, an enhancing in the inner layer is observed that is consistent with the observation of Righetti & Romano (2004). In particular, close to the wall, the second ($u'<0$, $v'>0$) and fourth ($u'>0$, $v'<0$) quadrant events have intensities more than two times larger than the unladen case, precisely in consistent with the observation of Righetti & Romano (2004). Additionally, the zigzag pattern illustrated in the near wall region of each quadrant event follows those of the experiment. When uncorrected scheme is used, however, no enhancing in the quadrant events is observed with results being nearly identical to the unladen case.

The observations in this work show the importance of the undisturbed fluid velocity in estimation of fluid forces acting on the particles. For particles that are smaller than the grid size, their disturbance becomes negligible and using the uncorrected PP approach might be sufficient. On the contrary, when size of the

particles becomes bigger than the grid size, e.g., the near wall configuration of the channel flow, then their disturbance becomes larger and one needs to account for that in the force computations.

4.4   Conclusion

In this work, a large eddy simulation (LES) coupled with point-particle (PP) approach was performed to study the interaction of sediment particles and turbulence in a horizontal channel flow in a dilute loading of 2.27×10^{-4}. In this approach the fluid phase is solved on a fixed Eulerian framework while particles are treated as subgrid points and tracked using the Newton's second law of motion. The fluid forces acting on the particles are computed based on the available closures for drag, lift, added mass and etc. These forces are derived based on the slip velocity that is dependent on the undisturbed fluid velocity at the location of particles. When the two phases are two-way coupled, such an undisturbed field becomes unavailable due to the disturbance created by the particles reaction force and using the disturbed fluid velocity for force computations results in erroneous predictions.

In this work, in order to recover the undisturbed field from the available disturbed fluid velocity, the correction scheme recently developed by Pakseresht *et al.* (2020) was employed to regularize the standard PP approach. This scheme was build in features to handle particle-laden flows with no-slip walls as well as those wherein the computational grid resolution is anisotropic. In order to account for mass displacement of particles on the background flow, the spatio-temporal variations in the volume fraction of the fluid phase were accounted for in both continuity and momentum equations.

It was shown that the standard uncorrected PP approach coupled with LES fails in capturing the experimental observations of the sediment-laden channel flow. Results obtained based on this formulation were almost identical to the unladen case, revealing the fact that particles in the uncorrected scheme do not alter the background flow. It was argued that the use of disturbed fluid velocity for force calculations on the particles results in such erroneous predictions as when the
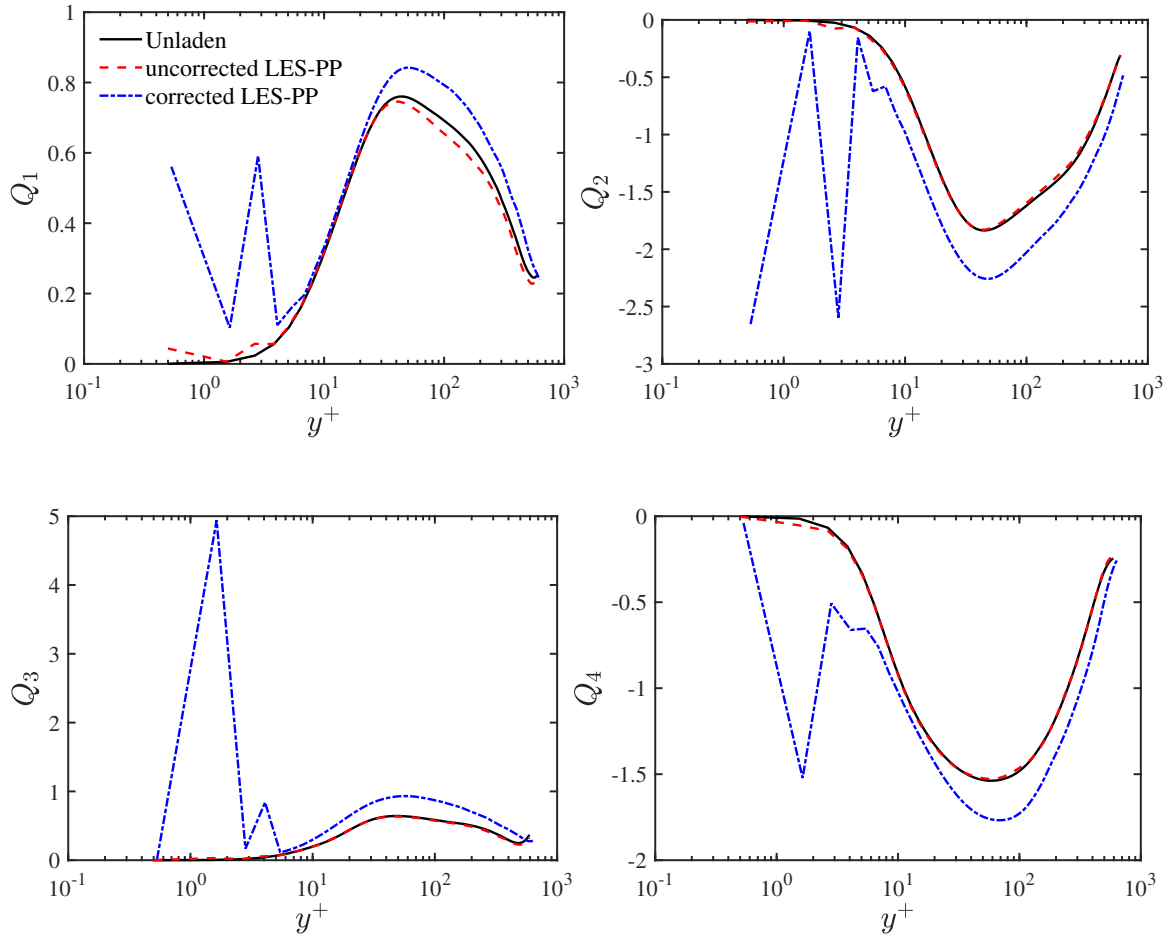
Figure 4.7: Quadrant events computed based on the LES-PP with and without the correction scheme compared with those of the unladen case.

PP approach was corrected with the correction scheme, most of the experimental observations were captured.

Increase in the friction velocity as well as in the near wall mean velocity of the fluid phase were both captured in line with the experimental observations. Additionally, damping in the outer layer of the fluid mean velocity, that is widely observed in the experimental works, was captured by the corrected PP approach. Consistent with the experiment of Kiger & Pan (2002), it was argued that the main mechanism behind damping is due to the normalization of the fluid mean velocity by a larger friction velocity obtained in the particle-laden case. In other words, the dimensional fluid velocity by itself is slightly damped due to the interaction of particles and turbulence in the outer layer. However, when it is normalized by the near wall scale, which has higher velocity, a stronger damping is observed. Consistent with the available experiments, a lag and lean in the particle mean velocity compared to the fluid phase were observed in the respective outer and inner layers of the channel using the prediction of the corrected PP approach. It was argued that the slight damping and enhancing in the dimensional fluid velocity are attributed to such a lag and lead in velocities of both phases. Slower-than-fluid particles in the outer layer push back the fluid phase while faster-than-fluid particles increase the velocity of the fluid phase in the inner layer.

Turbulence intensities in both streamwise and wall-normal directions showed an enhancing in the inner layer of the channel consistent with the observations of Righetti & Romano (2004). Similar enhancing was observed in the quadrant events of the Reynolds stress, while insignificant difference between the results of the uncorrected PP and unladen case was found, showing the negligible effect of particles on the flow in the uncorrected scheme. For very close to the wall regions, ejections and sweep events were both enhanced with two times larger values than the unladen case, consistent with the experimental observations. Despite the promising predictions, an overprediction in the outer layer of the results for turbulence intensities as well as quadrant events were observed. It was argued that such an overprediction could be attributed to either the embedded error in the

correction scheme (even few percent) or the experimental uncertainty. Regarding the former, the correction scheme is built upon the slow particle motions ($Re_p \sim 0.1$) whereas in the current channel flow, particles near the wall could experience larger particle Reynolds number on the order of $Re_p \sim 10$ for which further refinements in the correction scheme are necessary.

As a result, we conclude that using the uncorrected PP approaches for modeling the sediment-laden channel flows produces erroneous predictions and fails in capturing the effect of sediment particles on the flow. Promising results obtained using the corrected PP approach necessitates a need for using the velocity correction schemes along with the PP approach. This is required to accurately recover the undisturbed fluid velocity that is needed for the force computations. It should be noted that such a correction scheme should be able to handle the unique configuration of wall-bounded turbulent channel flows, wherein no-slip boundary condition as well as anisotropic grid resolutions with high aspect ratios are inevitable. We conjecture that the corrected PP framework used in this work could help improve the investigations and the state-of-the-art of the wall-bounded particle-laden flows wherein the lack of accuracy of the standard uncorrected PP approaches has been widely observed.

Acknowledgments

Chapter 5   Modelling drop deformation effect in Euler-Lagrange prediction of liquid jet in cross flow

Pedram Pakseresht and Sourabh V. Apte

Abstract

Accurate prediction of spray atomization process using an Euler-Lagrange (EL) approach requires accounting for the deformation of droplets, that is typically neglected in modeling such flows. Before atomization happens, liquid droplets undergo deformation due to the interaction of aerodynamic force, surface tension and viscous forces. In this work, droplet deformation effect is quantified by considering different models and comparing them against experimental data. Different breakup regimes are studied in order to identify the best model for each regime. The shape deformation effect is isolated by performing a single droplet injected into the cross flow with flow conditions similar to the bag-type breakup. A significant deviation in the motion of droplet is observed compared to a case where deformation is neglected.

5.1   Introduction

Liquid spray atomization plays an important role in analyzing the combustion process. A standard modeling approach is to split the process into two steps: primary followed by secondary atomization. Traditionally, the spray dynamics is modeled using an EL point-particle/parcel approach where liquid droplets are assumed subgrid as point droplets and their motion is captured by laws for drag, lift, added mass, and pressure forces. Their effect on the carrier phase is then modeled through two-way coupling of mass, momentum, and energy exchange (Dukowicz, 1980).

When a droplet is exposed to a high velocity gaseous phase, it undergoes deformation and distortion due to the balance between aerodynamic pressure force, surface tension and viscous dissipation forces. This effect which is typically neglected in the standard EL approaches could ultimately change the breakup process such as breakup time as well as size and velocity of the product drops. However, modeling such an effect and coming up with a unique predictive tool for all type of

breakup regimes is challenging. Taylor (1963) suggested an analogy between the oscillating and distorting droplet and a spring-mass system. In this analogy, the surface tension is analogous to the restoring force of the spring and the aerodynamic pressure force is analogous to the the external force on the mass. O'Rourke & Amsden (1987) added the liquid viscosity as a damping force to this model and modified it as Taylor Analogy Breakup (TAB) model which predicts the breakup process as well. In this spring-dashpot-mass system, forces are assumed to act on the center of droplet in order to model its oscillation and deformation. Since droplet is distorted at both north and south equators, therefore the idea of having forces act on the center of droplet was corrected by Clark (1988) in an energy conserved based formulation. In this modified model, each droplet consists of two half drops where forces act on the center of mass of each half. This results in two spring-dashpot-mass system for the given condition. Since Clark's model was linearized and the effect of non-linear deformation particularly for the large magnitudes was lost, Ibrahim *et al.* (1993) improved their model to account for the non-linear effects in large deformations. Three dimensional nature of distorting drop is accounted for by conserving the drop volume instead of area leading to a new Droplet Deformation breakup (DDB) model.

Park *et al.* (2002) improved the original TAB model by modifying the aerodynamic pressure force. This was performed by taking into account the size variation in the projected area of the drop during deformation which was neglected in the original TAB model. Wang *et al.* (2014) developed a model for Bag-Type Breakup (BTB) based on a modified version of the model that was put forth by Detkovskii & Frolov (1994) wherein kinetic energy of drop is assumed negligible for low Weber number deformations. In their formulation, the expression of deformation was moved to the center of half-drop due to Hill-vortex formation around this point. Similar to Clark (1988) and Ibrahim *et al.* (1993), all forces are applied to the center of mass of half drop. Surface tension is decomposed into two positive and negative parts where the former tends to flatten and the latter restores the drop, respectively. The extension of their model for higher Weber number cases, i.e.,

Multimode Bag (MMB) breakup regime includes the kinetic energy of the droplet Wang *et al.* (2015).

Sor & García-Magariño (2015) in the context of ice accretion modified the DDB model by Ibrahim *et al.* (1993) by taking into account the accurate calculation of surface tension force. In addition, the instantaneous velocity of the droplet is employed in the deformation model rather than a constant upstream velocity. Furthermore, the center of mass of a half ellipsoid was chosen rather than that of half of sphere. Better predictions on the deformation of a droplet impinging on an airfoil were observed compared to the traditional models, e.g., TAB, Clark's and DDB models.

In this work, the deformation effect of droplets in a liquid jet in cross flow is planned for investigation. Different deformation models are investigated by assessing their predictive capabilities for a wide range of Weber numbers and breakup regimes typically observed in sprays. Drop deformation in bag, multimode, transition and shear breakup regimes are all examined to identify a proper model for each regime. These models are deemed to apply to a real atomizing jet in cross flow. However, as a first step in studying the deformation effects, a single liquid droplet injected into a cross flow is examined where the flow parameters are similar to a bag-type breakup condition. It is conjectured that accounting for drop deformation is necessary for accurately modeling liquid jet in cross flow.

5.2 Mathematical description

Different modeling approaches on the droplet deformation are explained and compared here. For each model the normalized equations with $y=y/r_o$ and $t=tu_\infty/r_o$ are provided. Deformation equation in the TAB model is expressed as follows

$$\frac{d^2y}{dt^2} + \frac{5N}{ReK}\frac{dy}{dt} + \frac{8}{WeK}y = \frac{2}{3K} \qquad (5.2.1)$$

where $N=\mu_l/\mu_g$, $K=\rho_l/\rho_g$, $Re = \rho_g ur/\mu_g$ and $We=\rho_g u^2 r/\sigma$ are viscosity ratio, density ratio, Reynolds and Weber numbers of drop, respectively. The improved

TAB model developed by Park *et al.* (2002) in which the aerodynamic force modified during deformation process is obtained as

$$\frac{d^2y}{dt^2} + \frac{5N}{ReK}\frac{dy}{dt} + \frac{1}{K}y\left(\frac{8}{We} - 2C_F - 0.5C_F\right) = \frac{2C_F}{K} \tag{5.2.2}$$

where $C_F=4/19$ is chosen such that the critical Weber number, i.e., $We_{crt}=6$ is met. DDB model by Ibrahim *et al.* (1993) and its modified version by Sor & García-Magariño (2015) are given below. These two models are different in calculation of surface area as well as the center of mass of half drop. The latter leads to different constant c values of $3\pi/4$ and $8/3$ for DDB and its modified version, respectively.

$$\frac{d^2y}{dt^2} + \frac{4N}{ReK}\frac{1}{y^2}\frac{dy}{dt} + \frac{3c}{4KWe}\frac{dA_s}{da} = \frac{3}{8K}c_p \tag{5.2.3}$$

where c_p is the pressure coefficient in order to take into account the variations in the gas pressure acting on the droplet surface during deformation. This parameter could be adjusted based on any available experimental data or accurate fully resolved DNS results. dA_s/da for both models is given based on the following expression. Despite the original DDB wherein a simplified version of this parameter was used, its accurate calculation is employed in the modified DDB by Sor & García-Magariño (2015).

$$\frac{dA_s}{da} = \begin{cases} 4a - \frac{4}{a^5\epsilon}\ln\left(\frac{1+\epsilon}{1-\epsilon}\right) + \frac{3}{a^{11}\epsilon}\left[\frac{2}{\epsilon(1-\epsilon^2)} - \frac{1}{\epsilon^2}\ln\left(\frac{1+\epsilon}{1-\epsilon}\right)\right] & \text{Modified DDB} \\ 4a(1 - 2(a)^{-6}) & \text{DDB} \end{cases} \tag{5.2.4}$$

where $a=cy$ is the normalized major semi-axis of the half drop and $\epsilon=\sqrt{1-a^{-6}}$. The deformation model in BTB model developed by Wang *et al.* (2014) is expressed as

$$\frac{dy}{dt} = \frac{yC_L}{(KN)^{1/3}}\left(\frac{C_d}{2} - \frac{2C_f}{We}\left[a^{-1} + a^5 - 2a^{-4}\right]\right) \tag{5.2.5}$$

where $C_L=C_{d,sph}=0.45$ to account for changes in the pressure on drop surface

during deformation from sphere to disk. Comparing with experiments, C_f=1/600 was obtained to be the best to close the model Wang *et al.* (2014). The drag coefficient, C_d, is obtained as

$$C_d = \begin{cases} C_{d,sph} & \text{for} \quad (We < 10) \\ 2.1 - 13.63/We^{0.95} & \text{for} \quad (We \geq 10) \end{cases} \tag{5.2.6}$$

The MMB model by Wang *et al.* (2015) is expressed as

$$\frac{d^2y}{dt^2} = \frac{12N}{KRe}\left[-\frac{1}{y}\frac{dy}{dt} + \frac{C_L}{(KN)^{1/3}}\left(\frac{C_d}{2} - \frac{2C_f}{We}\left[a^{-1} + a^5 - 2a^{-4} \right] \right) \right] \tag{5.2.7}$$

where C_f=0.005 and C_d is achieved similar to Eq. 5.2.6 while C_L is obtained as following

$$C_L = \begin{cases} C_\mu(360 - 413.We^{-0.057}) & (15 < We \leq 40) \\ C_\mu[18.72\exp(5.29\times 10^{-3}We) \\ \quad + 0.1125\exp(5.8\times 10^{-2}We)] & (40 < We \leq 80) \end{cases} \tag{5.2.8}$$

where

$$C_\mu = 7.024\times 10^{-3}Oh^{-4/3}K^{-1/3} \tag{5.2.9}$$

and Ohnesorge number, $Oh=\mu_l/\sqrt{\rho_l d_0 \sigma}$. Note that in the two last models (BTB and MMB) unlike others, the Weber and Reynolds numbers are calculated based on diameter of drop.

5.3   Results and Discussion

The deformation effect on the dynamics of a liquid droplet is studied in this part. It is widely observed that in a spray atomization process, depending on the Weber and Ohnesorge numbers, droplets undergo different phases in terms of deforma-

Case	Re	We	Oh	N	K
Bag	3323.16	13.5	1.88×10^{-3}	47.9	789
Mult. bag	5161.93	18	1.4×10^{-3}	47.9	789
Transition	8794.4	52.6	1.4×10^{-3}	47.9	789
Shear	12235.69	101	1.4×10^{-3}	47.9	789

Table 5.1: Different breakup regimes based on the experimental work of Krzeczkowski (1980).

tion and breakup Krzeczkowski (1980); Hsiang & Faeth (1992). For $We<1$, no deformation occurs while drops experience non-oscillatory or oscillatory deformation for $1<We<10$. Increasing Weber number further results in more distortion which in turn depending on Weber number, one of the bag, multimode, transition or shear breakup takes place Hsiang & Faeth (1992). Moreover, it is observed that deformation in each breakup regime is quite different Krzeczkowski (1980).

There have been several models predicting the deformation, yet having a model being capable for all regimes is challenging. In this part, the capability of all available models are compared together against the experimental data of Krzeczkowski (1980) in order to identify the best possible model for each breakup regime. Bag, multimode bag, transition and shear breakup regimes corresponding to the experiment are listed in Tab. 5.1.

Deformation models were solved numerically using fourth order Runge-kutta method. Note that the ratio of drop diameter to its initial value, a/r_o, is defined differently among models. In TAB and its modified version, $a/r_o=1+0.5y$ whereas in other models $a/r_o=cy$. As shown in Fig. 5.1 and 5.2, the MMB model by Wang et $al.$ (2015) predicts better deformation among others where a good agreement with experiment is achieved. TAB and DDB models and their modifications fail in predicting the large deformation involve in these cases. The modified TAB model by Park et $al.$ (2002) predicts the deformation better than TAB and DDB, however, it underpredicts for $t>100$. Accordingly, it can be inferred that the MMB model developed by Wang et $al.$ (2015) would be suitable for deformation
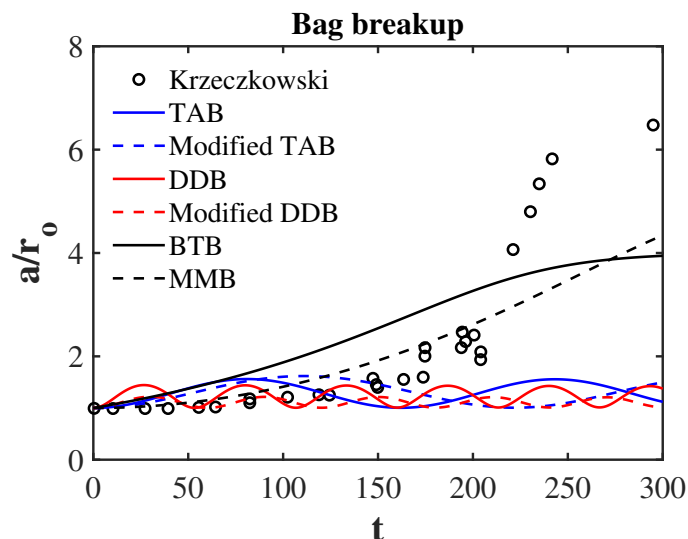
Figure 5.1: Drop deformation in bag breakup regime based on different models compared to the experiment

modeling of a droplet in bag and multimode bag breakup regimes. Regarding the transition regime shown in Fig. 5.3, both TAB and DDB models show better agreement with the experiment whereas BTB, MMB and modified TAB models all together overpredict the large deformations, i.e., $t>80$. For shear-type breakup regime as plotted in Fig. 5.4, the modified TAB model enormously over predict the experimental observation and does not follow the experimental trend. In addition, as mentioned in their work, both BTB and MMB models are suited for bag breakup regime and applying them to shear regime is naive Wang *et al.* (2014, 2015). Both TAB and DDB models are within the range of experiment for shear breakup regime, however, the downward trend observed in the experiment is only captured in the DDB model and its modification by Sor & García-Magariño (2015). This shows that for shear breakup regime, one can employ the energy based deformation model by Ibrahim *et al.* (1993). It is worth mentioning that the robustness and predictive capability of these models would be verified better if they were compared with more experimental data in each regime.

Moreover, as observed by Sor & García-Magariño (2015), the pressure term may
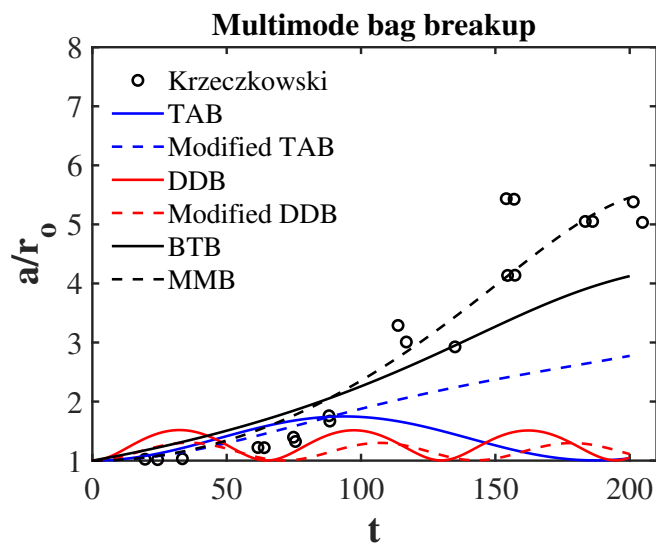
Figure 5.2: Drop deformation in multimode bag breakup regime based on different models compared to the experiment
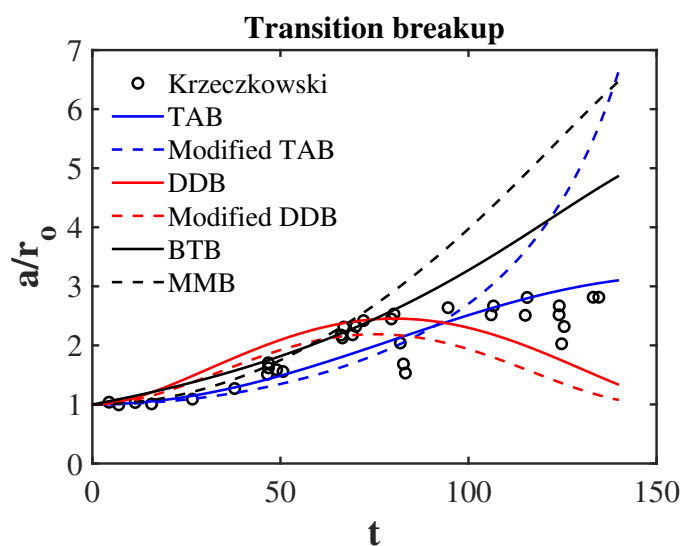
Figure 5.3: Drop deformation in transition breakup regime based on different models compared to the experiment
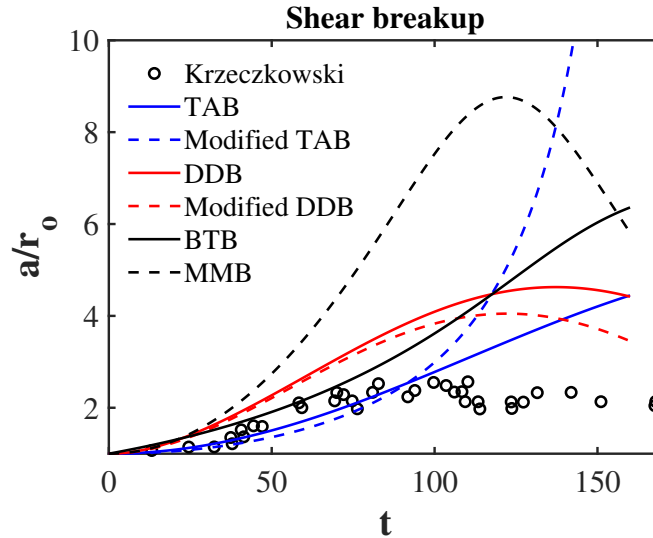
Figure 5.4: Drop deformation in shear breakup regime based on different models compared to the experiment

vary during deformation and this can be accounted for by introducing a pressure coefficient, C_p. They found C_p=0.93 to better predict the corresponding experiment in the context of ice accretion, however, this may change for different flow and regimes. The effect of this parameter on the deformation of a droplet in the shear breakup regime is shown in Fig. 5.5. c_p=0.7 gives rise to better results for this regime revealing the fact that further modifications and tuning are required for this model and the assumption of having constant pressure on drop surface might be invalid.

It should be mentioned that these models have to be implemented for real cases where more accurate Reynolds and Weber numbers are used rather than the constant values typically employed in the literature. However, depending on the drop relaxation and deformation time scales, one can estimate whether drop is displaced significantly during deformation. For cases where deformation occurs much faster than its displacement, then assuming a constant slip velocity during deformation would be acceptable. For a real spray case where different Weber and Reynolds numbers exist, a strategy would be required in order to switch between these mod-
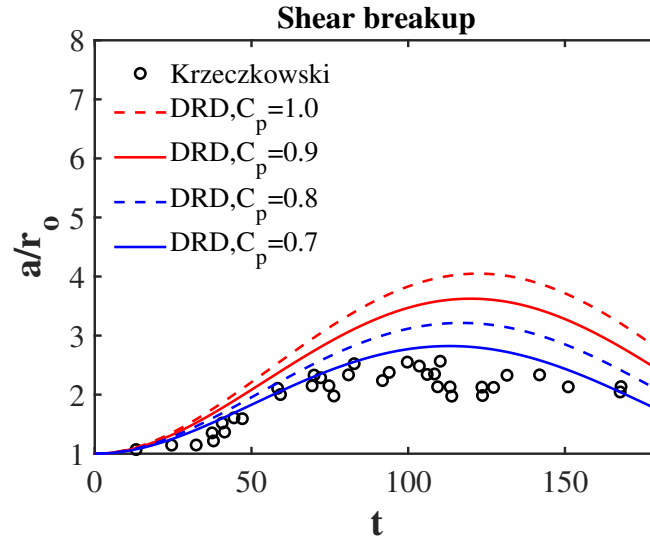
Figure 5.5: Effect of pressure coefficient on the prediction of DDB model

els. Therefore, employing one model may result in inaccurate deformation results and its consequence effects on breakup.

These models are intended to be tested on a case wherein series of liquid drops are injected into a cross flow and they undergo deformation before breakup occurs. As an initial test case, in order to isolate the deformation effect, a single liquid droplet is injected into a uniform flow with parameters similar to bag breakup regime. Due to the small volume loading of the drop, one-way coupling is chosen and the volumetric displacement effect for this case is conjectured to be insignificant. Hsiang & Faeth (1992) observed that drag coefficient increases linearly from sphere to disk during deformation process if internal circulation is negligible. This shows that deformation has a direct influence on the dynamics of the drop through its modified drag coefficient. Liu *et al.* (1993) obtained a linear relation for drag coefficient as a function of deformation parameter based on TAB model as

$$C_d = C_{d,sph}(1 + 2.632y) \tag{5.3.1}$$

while Liang *et al.* (2017) derived a power law relation for this coefficient as

$$C_d = 0.7y^{0.516} + 0.47 \tag{5.3.2}$$

In order to couple the deformation and its effect on the motion of a single droplet injected into the cross flow, cases with and without the deformation effect on the drag are compared. Bag-type breakup condition of Tab. 5.1 is examined before breakup occurs (t<300). Fig. 5.6 shows the results with modified drag coefficient based on the above formulations. As shown, a significant deviation is observed in the motion of droplet relative to the case where deformation is not accounted for. This could potentially alter the breakup process and affect the size and velocity of the product drops after breakup and disintegration takes place. In our future investigations, the deformation effects on the trajectory of series of liquid drops injected into the cross flow will be examined where a combination of different models will be employed to more accurately capture these effects. In addition, the effect of internal circulation, which is conjectured to decrease the drag coefficient, is deemed for further investigations.
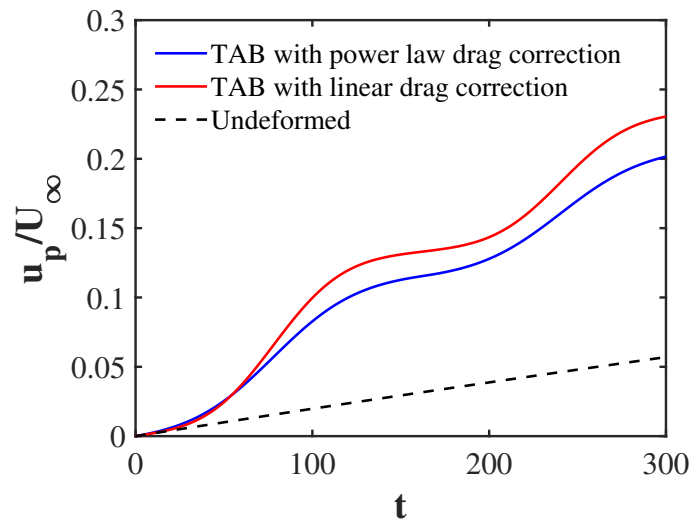
Figure 5.6: Drop deformation effect on the motion of a liquid droplet in a bag-type breakup regime

5.4   Conclusions

Different deformation models were tested against the available experimental data to identify the most accurate model for each breakup regime. It was observed that the MMB model predicts the best for bag and multimode bag breakup regimes while the original TAB agreed well with the experiment in the transition regime. The modified DDB model with a modified pressure coefficient was observed to match the data very well. It was conjectured that a hybrid model based on combination of these models is required for real spray atomization flows wherein a wide range of Weber numbers and breakup regimes exist. In order to isolate the deformation effects, as a first step, a single droplet injected into the cross flow was investigated. It was observed that accounting for deformation effect results in a significant increase in the velocity of droplet. Accordingly, we hypothesize that if deformation effect is systematically extended to the dense liquid jet in cross flow, similar results with more pronounced effects will be achieved.

Chapter 6   Conclusions and future directions

This work focused on improvement of the Euler-Lagrange (EL) approaches in modeling of particle-laden turbulent flows. In this approach, the fluid phase is typically solved using an Eulerian framework while particles are treated as Lagrangian point-particles (PP) and tracked following the Newton's second law of motion based on the available closures for the fluid forces acting on them. The effect of particles on the background flow is modelled by applying the particle reaction force to the flow through a momentum source term. However, such a simplified point-force model for capturing the inter-phase interactions has been shown to be insufficient or produce erroneous predictions.

When the fluid and particle phases are two-way coupled, inaccuracies arise in predictions of this approach. One source of inaccuracy is that the fluid phase equations in this approach are solved for the entire flow field including the volume occupied by the particles, while the mass displacement of the particles is not accounted for. The other source is that the accuracy of fluid forces decays in two-way coupled simulations, owing to the disturbance created by particle reaction forces. The closure models for computing fluid forces acting on the particles require undisturbed fluid velocity at the location of particles. However, when the fluid and particle phases are two-way coupled, the particle reaction force disturbs the background flow at the location of particles, and using such a disturbed fluid velocity for the force computations results in erroneous predictions. These two sources of inaccuracy were tackled in this dissertation in order to improve the predictions of EL approach.

Concerning the first issue, the spatio-temporal variations of the fluid phase volume fraction were accounted for in solving the continuity and Navier-Stokes equations of the fluid phase. Using this volume-averaged formulation, two source terms appear in both continuity and momentum equations that account for the

mass displacement effect of particles on the background flow. The inter-phase coupling are then enforced through two different mechanisms; (i) momentum exchange through reaction force between phases and (ii) the mass displacement effect of particles on the background flow through these two source terms. Large Eddy Simulations (LES) of a particle-laden jet under a wide range of volume loadings $(0.047\%-37.6\%)$ and particle Strokes numbers $(0.038-11.6)$ were carried out with and without the mass displacement effect of particles. It was shown that for volume loadings above 5%, the displacement effect of particles enhances both mean and r.m.s. velocities of the carrier phase near the nozzle exit. The mechanism behind such an enhancement was found to be due to the continuity source term that diminishes further downstream of the nozzle, owing to the radial dispersion of particles and jet spread. Lowering the Stokes number of particles decreased the displacement effects near the nozzle, however, increased further downstream. Preferential concentration and dispersion of particles were found to be responsible for these two observations, respectively.

The second issue that arises in the fluid force computation of the two-way coupled simulations was resolved by introducing a general velocity correction scheme in order to recover the undisturbed fluid velocity at the location of particles from the available disturbed field. The newly developed model is general and can be used for (i) unbounded and wall-bounded regimes, (ii) isotropic and anisotropic gris resolutions, (iii) particles with different density and size, (iv) arbitrary interpolation and distribution functions, and (v) flows with finite particle Reynolds number. The scheme captures the disturbance of a particle created in a computational cell by modeling that cell as a solid object that is exposed to the particle's force. Using analytical and empirical expressions, the response of the cell to the particles force is computed at each time step concurrently to the equation of motion of particles. knowing the disturbance velocity, the undisturbed fluid velocity at the location of particles is retrieved. The model was assessed for settling velocity of a particle in unbounded and wall-bounded regimes with few percent errors at all wall distances. Ignoring wall effects in the model, however, results in errors

on the same order of magnitude of the uncorrected scheme, underscoring the need for such a wall-modified correction scheme.

The volume-averaged formulation along with the velocity correction scheme developed in Chapter 2 and 3, respectively, were employed to predict the interaction of particle and turbulence in a horizontal turbulent channel flow with Re_τ=583.33. It was observed that the standard EL-PP approach, wherein neither mass displacement effect of particles nor undisturbed fluid velocity is employed, fails in capturing the experimental observations. Results of this approach in the presence or absence of particles were nearly identical, revealing the weakness of this uncorrected approach in capturing particles' effect. Furthermore, it was observed that accounting for the mass displacement of particles does not improve the predictions and results with and without this effect are similar. However, when the undisturbed fluid velocity at the location of particles was recovered, the fluid forces acting on the particles were computed accurately, and the effect of particles on the background flow was correctly captured, in line with the experimental observations. Increase in the friction velocity as well as enhancing in the near wall dynamics were both observed. In addition, the so-called damping effect of particles on the fluid mean velocity was observed, as well.

Finally, the deformation of particles that is commonly encountered in the liquid droplets (before breakup happens) in liquid atomization flows was investigated. It was shown that the current models are each suitable for a particular breakup regime, and a hybrid deformation model is required to accurately predict the deformation effect of a real atomization process, wherein different breakup regimes are encountered. As a test case, deformation of a droplet in a simplified configuration wherein the droplet was injected into a cross flow, was studied. It was observed that ignoring such an effect produces underprediction on the motion of the droplet, which could ultimately affect the the breakup process and the size of product drops.

6.1 Future directions

The formulation developed in this dissertation will open up many other investigations for the near future. From model development to studying the underlying physics of the particle-laden flows, different extensions of the current work are explained briefly in the following.

Concerning the model development, the correction scheme introduced in Chapter 3 requires further refinements. The scheme was built based on the concept that the relative velocity of the particles to the fluid is small enough, e.g., $Re_p < O(0.1)$, that the assumption of Stokes flow around the particles becomes valid. Although an adjustment to account for Re_p up to 10 was introduced in the model, the non-linear and asymmetric behaviour of the flow around the particle in larger values ($Re_p > 10$) were not captured in that adjustment. There are many applications such as spray atomization or liquid jet in cross flow wherein the liquid droplets will not experience such a Stokes flow condition. Although the need for such a correction in extremely large Re_p cases diminishes, further investigations are still required to identify a range of Re_p for which the correction is necessary. For such a range modifications due to the larger Re_p in the correction scheme is crucial.

Besides, the correction scheme was based on the assumption that the loading of particles in the flow is so dilute that the disturbance created by each particle does not affect the ones created by others. For each particle, its disturbance is computed as if there is no other particles in its vicinity, and the background flow is only influenced by the presence of itself. However, for flows with dense loadings or areas with clustering of particles, such an assumption does not necessarily hold and the disturbance created by each particle affects the others'. In a simplified configuration, let us assume having two particles almost touching each other. The disturbance created on the background flow at their interface will be the superposition of the disturbance created by each individual particle. Such a disturbance will certainly differ from the one that would have been created if there was only one particle. When we predict the disturbance created by the particles on the background flow, such a secondary effect must be taken into account, otherwise,

erroneous predictions will be obtained by ignoring such an effect. A remedy to account for neighbouring effect is to change the current formulation from Lagrangian to Eulerian framework. Currently, the correction velocity formulation is attached to each particle in a Lagrangian frame and solved for each particle, individually. One can use the same formulation for disturbance created for each Eulerian computational cell rather than each Lagrangian particle. In this case, the disturbance created by all particles in a computational cell will be superimposed and stored in that cell. In other words, a disturbance velocity will be associated to each fluid cell in the computational domain. When the disturbance is needed at the location of each particle, then the disturbances created in the adjacent computational cells are interpolated to the particle which this process automatically captures the neighbouring effects.

It is imperative to mention that such an effect should also be accounted on the drag force of particles, when the dense regime is concerned. Akiki *et al.* (2017*a*,*b*) showed the significant deviation in the drag force of each individual particle when situated in a dense pack. Such an effect, that is currently ignored, could be added to the estimation of the drag force to improve the accuracy of the EL-PP approaches.

Moreover, Maxey & Riley (1983) derived all possible forces acting on a sphere in the Stokes regime, among which the history effect and the undisturbed forces are usually ignored in the EL-PP simulations. The latter, which is the force that would exist in the undisturbed fluid flow if the particles was not present, could become important for flows with low density ratio such as sediment transport. However, without recovering the undisturbed fluid velocity and analogous to other forces, this force would have been computed based on the erroneous disturbed field which could have produced incorrect predictions and potentially negligible effect. Upon having the current correction scheme, however, one could quantify the accurate contribution of this force in comparison with other forces, particularly with the dominant steady state drag force.

The present formulation can help better understand and revisit some of the underlying physics involved in the particle-laden flows. Of importance is the pref-

erential concentration and clustering of particles for which most of the studies have been performed using one-way coupled PP approaches, owing to the dilute concentration of particles in these flows. However, the local interaction of particles and turbulence in the preferentially concentrated regions might be strong enough that the two-way coupled simulations become necessary to be performed. Nevertheless, as explained in Chapters 3 and 4, the predictions of the uncorrected two-way coupled PP approach could become incorrect or identical to the one-way coupled results (similar to the channel results of Chapter 4), hence researchers would rely on one-way coupled predictions for analysis of these flows. With the corrected two-way coupled PP approach, it is conjectured that more accurate observations will be obtained for the studies of the clustering of particles. Similarly, turbophoresis, that is the tendency of particles to accumulate near the wall in the wall-bounded flows, can be revisited using the present two-way coupled formulation. Energy harvesting (Kamrani Fard *et al.*, 2019; Esmaeilzadeh & Alam, 2019; Siala *et al.*, 2020) and effect of particles in this context could be explored further using the developed formulation in this dissertation. In addition, the present methodology can be applied for investigations in the field of oil recovery (Esmaeilzadeh *et al.*, 2019, 2020).

Rotation of particles might have significant effect on the background flow in the areas wherein particles are larger than the local grid resolutions (fluid length scale). Such configuration occurs in the near wall region of the channel flow simulations or near the nozzle in jet in cross flows. Andersson *et al.* (2012) developed a method for capturing the rotation effect of particles on the background flow. In their model, the divergence of the particles' torque is added to the momentum equation in each direction through a source term, analogous to the force effect of particles on the fluid flow. Such a simplified force-wise model does not necessarily capture the rotation effect of the particles. One can develop a model that measures the torque of each particle and based on that, adds a distribution of forces to the adjacent computational cells so that these forces produce the same torque as the particle would do in reality. Such a model, however, requires particles to be either on the

same size of or larger than the computational cell. How much such a model captures the rotation effect of particles on the background flow and how significantly this effect alters the results are open questions for the future investigations.

Finally, in this dissertation we only considered cold particle-laden flows wherein the temperature difference between phases was negligible to have any inter-phase heat transfer. For heated particle-laden flows such as solar receivers (Pouransari & Mani, 2017), fluidized bed reactors, volcanic plumes, and combustion-triggered soot formation, among others, an energy exchange between phases happens due to the temperature difference between phases. Thus, the energy equation for both fluid and particle phases must be solved in addition to the momentum equations. For two-way energy coupled simulations, the inter-phase energy exchange is modeled by adding the particles' heat flux to the fluid energy equation through a heat flux source term. This source term disturbs the fluid temperature at the location of particles and using such a disturbed temperature field for estimating the particle's heat in the next time step will produces erroneous results, owing to the fact that the closure models for heat transfer depend on the undisturbed fluid temperature. Analogous to the velocity correction scheme, a temperature correction scheme is required to capture the disturbance created in the temperature field in order to recover the undisturbed fluid temperature. Such a model can be based upon the formulation developed in this dissertation using the same concept. The disturbance created in the computational cell due to the particle's heat flux can be obtained by treating the computational cell as a solid object that is subject to the particle's heat flux. Using the lumped assumption for such an object, one can write the energy balance equation for this object and find the temperature created by the particle's heat. Then, this temperature is the disturbance created in the temperature field that is missing in the standard two-way energy coupled simulations. Upon predicting this disturbance, it will be added to the disturbed field (that is available in the computation) in order to recover the undisturbed field. Analogous to Chapter 3, wall effects on the temperature disturbance can be developed as well. Developing such a temperature correction scheme along with the present

velocity correction scheme will certainly open up further investigations in the field and improve the state-of-the-art of the modeling of the heated particle-laden flows.

Bibliography

AKIKI, G, JACKSON, TL & BALACHANDAR, S 2017*a* Pairwise interaction extended point-particle model for a random array of monodisperse spheres. *Journal of Fluid Mechanics* **813**, 882–928.

AKIKI, G, MOORE, WC & BALACHANDAR, S 2017*b* Pairwise-interaction extended point-particle model for particle-laden flows. *Journal of Computational Physics* **351**, 329–357.

ANDERSON, T BO & JACKSON, ROY 1967 Fluid mechanical description of fluidized beds. Equations of motion. *Industrial & Engineering Chemistry Fundamentals* **6** (4), 527–539.

ANDERSSON, HELGE I, ZHAO, LIHAO & BARRI, MUSTAFA 2012 Torque-coupling and particle–turbulence interactions. *Journal of Fluid Mechanics* **696**, 319–329.

APTE, SV, GOROKHOVSKI, MIKHAEL & MOIN, PARVIZ 2003 LES of atomizing spray with stochastic modeling of secondary breakup. *International Journal of Multiphase Flow* **29** (9), 1503–1522.

APTE, SV, MAHESH, KRISHNAN & LUNDGREN, T 2008 Accounting for finite-size effects in simulations of disperse particle-laden flows. *International Journal of Multiphase Flow* **34** (3), 260–271.

AUTON, TIMOTHY ROBERT 1983 The dynamics of bubbles, drops and particles in motion in liquids. PhD thesis, University of Cambridge.

BAGCHI, PROSENJIT & BALACHANDAR, S 2003 Effect of turbulence on the drag and lift of a particle. *Physics of Fluids* **15** (11), 3496–3513.

BALACHANDAR, S 2009 A scaling analysis for point–particle approaches to turbulent multiphase flows. *International Journal of Multiphase Flow* **35** (9), 801–810.

BALACHANDAR, S & EATON, JOHN K 2010 Turbulent dispersed multiphase flow. *Annual review of fluid mechanics* **42**, 111–133.

BALACHANDAR, S, LIU, KAI & LAKHOTE, MANDAR 2019 Self-induced velocity correction for improved drag estimation in euler–lagrange point-particle simulations. *Journal of Computational Physics* **376**, 160–185.

BATTISTA, FRANCESCO, MOLLICONE, J-P, GUALTIERI, PAOLO, MESSINA, ROBERTA & CASCIOLA, CARLO MASSIMO 2019 Exact regularised point particle (erpp) method for particle-laden wall-bounded flows in the two-way coupling regime. *Journal of Fluid Mechanics* **878**, 420–444.

BENSON, MICHAEL J & EATON, JOHN K 2003 The effects of wall roughness on the particle velocity field in a fully developed channel flow. PhD thesis, Stanford University Stanford, CA.

BEST, J., BENNETT, S. & LEDDER, J. BRIDGE M. 1997 Turbulent modulation and particle velocities over flat sand beds at low transport rates. *J. Hydr. Engng ASCE* **123**, 1118–1129.

BLAKE, JR 1971 A note on the image system for a stokeslet in a no-slip boundary. In *Mathematical Proceedings of the Cambridge Philosophical Society*, , vol. 70, pp. 303–310. Cambridge University Press.

BLOKKEEL, GREGORY, BARBEAU, B & BORGHI, R 2003 A 3D Eulerian model to improve the primary breakup of atomizing jet. *SAE Technical Paper* (No. 2003-01-0005).

BRENNER, HOWARD 1961 The slow motion of a sphere through a viscous fluid towards a plane surface. *Chemical engineering science* **16** (3-4), 242–251.

CAPECELATRO, J. & DESJARDINS, O. 2013 An Euler-Lagrange strategy for simulating particle–laden flows. *Journal of Computational Physics* **238**, 1–31.

CAPECELATRO, JESSE, DESJARDINS, OLIVIER & FOX, RODNEY O 2014 Numerical study of collisional particle dynamics in cluster-induced turbulence. *Journal of Fluid Mechanics* **747**, R2.

CHAOUI, MOHAMED & FEUILLEBOIS, FRANÇOIS 2003 Creeping flow around a sphere in a shear flow close to a wall. *Quarterly Journal of Mechanics and Applied Mathematics* **56** (3), 381–410.

CHESNEL, JEREMY, MENARD, THIBAUT, REVEILLON, JULIEN & DEMOULIN, FRANCOIS-XAVIER 2011*a* Subgrid analysis of liquid jet atomization. *Atomization and Sprays* **21** (1), 41–67.

CHESNEL, JEREMY, REVEILLON, JULIEN, MENARD, THIBAUT & DEMOULIN, FRANCOIS-XAVIER 2011*b* Large eddy simulation of liquid jet atomization. *Atomization and Sprays* **21** (9), 711–736.

CIHONSKI, ANDREW J, FINN, JUSTIN R & APTE, SOURABH V 2013 Volume displacement effects during bubble entrainment in a travelling vortex ring. *Journal of Fluid Mechanics* **721**, 225–267.

CLARK, MARK M 1988 Drop breakup in a turbulent flow—i. conceptual and modeling considerations. *Chemical engineering science* **43** (3), 671–679.

CLIFT, ROLAND, GRACE, JOHN R & WEBER, MARTIN E 2005 *Bubbles, drops, and particles*. Courier Corporation.

COLEMAN, NEIL L 1986 Effects of suspended sediment on the open-channel velocity distribution. *Water Resources Research* **22** (10), 1377–1384.

COX, RAYMOND G & BRENNER, HOWARD 1967 The slow motion of a sphere through a viscous fluid towards a plane surface—ii small gap widths, including inertial effects. *Chemical Engineering Science* **22** (12), 1753–1777.

CROWE, CT, TROUTT, TR & CHUNG, JN 1996 Numerical models for two-phase turbulent flows. *Annual Review of Fluid Mechanics* **28** (1), 11–43.

CUNDALL, P.A. & STRACK, O.D.L. 1979 A discrete numerical model for granular assemblies. *Geotechnique* **29**, 47–65.

DAI, YI, KOBAYASHI, TOSHIO & TANIGUCHI, NOBUYUKI 1994 Large eddy simulation of plane turbulent jet flow using a new outflow velocity boundary condition. *JSME International Journal Series B Fluids and Thermal Engineering* **37** (2), 242–253.

DARMANA, DADAN, DEEN, NIELS G & KUIPERS, JAM 2006 Parallelization of an Euler–Lagrange model using mixed domain decomposition and a mirror domain technique: Application to dispersed gas–liquid two-phase flow. *Journal of Computational Physics* **220** (1), 216–248.

DEEN, NG, ANNALAND, M VAN SINT, VAN DER HOEF, MARTIN ANTON & KUIPERS, JAM 2007 Review of discrete particle modeling of fluidized beds. *Chemical Engineering Science* **62** (1-2), 28–44.

DEEN, NIELS G, VAN SINT ANNALAND, M & KUIPERS, JAM 2004 Multi-scale modeling of dispersed gas–liquid two-phase flow. *Chemical Engineering Science* **59** (8), 1853–1861.

DETKOVSKII, DA & FROLOV, SM 1994 Model of the deformation of a liquid droplet in a gas flow. *Journal of applied mechanics and technical physics* **35** (6), 911–919.

DUKOWICZ, JOHN K 1980 A particle-fluid numerical model for liquid sprays. *Journal of Computational Physics* **35** (2), 229–253.

EATON, JOHN K 2009 Two-way coupled turbulence simulations of gas-particle flows using point-particle tracking. *International Journal of Multiphase Flow* **35** (9), 792–800.

ELGHOBASHI, S 1991 Particle-laden turbulent flows: direct simulation and closure models. *Applied Scientific Research* **48** (3-4), 301–314.

ELGHOBASHI, S 1994 On predicting particle-laden turbulent flows. *Applied Scientific Research* **52** (4), 309–329.

ELGHOBASHI, SAID 2006 An updated classification map of particle-laden turbulent flows. In *IUTAM Symposium on Computational Approaches to Multiphase Flow*, pp. 3–10. Springer.

ELGHOBASHI, S & TRUESDELL, GC 1993 On the two-way interaction between homogeneous turbulence and dispersed solid particles. i: Turbulence modification. *Physics of Fluids A: Fluid Dynamics* **5** (7), 1790–1801.

ESMAEILZADEH, SOHEIL & ALAM, MOHAMMAD-REZA 2019 Shape optimization of wave energy converters for broadband directional incident waves. *Ocean Engineering* **174**, 186–200.

ESMAEILZADEH, SOHEIL, SALEHI, AMIR, HETZ, GILL, OLALOTITI-LAWAL, FEYISAYO, DARABI, HAMED & CASTINEIRA, DAVID 2019 A general spatio-temporal clustering-based non-local formulation for multiscale modeling of compartmentalized reservoirs. *arXiv preprint arXiv:1904.13236* .

ESMAEILZADEH, SOHEIL, SALEHI, AMIR, HETZ, GILL, OLALOTITI-LAWAL, FEYISAYO, DARABI, HAMED & CASTINEIRA, DAVID 2020 Multiscale modeling of compartmentalized reservoirs using a hybrid clustering-based non-local approach. *Journal of Petroleum Science and Engineering* **184**, 106485.

Esmaily, Mahdi & Horwitz, JAK 2018 A correction scheme for two-way coupled point-particle simulations on anisotropic grids. *Journal of Computational Physics* **375**, 960–982.

Ferrante, Antonino & Elghobashi, Said 2004 On the physical mechanisms of drag reduction in a spatially developing turbulent boundary layer laden with microbubbles. *Journal of Fluid Mechanics* **503**, 345–355.

Ferrante, Antonino & Elghobashi, Said 2005 Reynolds number effect on drag reduction in a microbubble-laden spatially developing turbulent boundary layer. *Journal of Fluid Mechanics* **543**, 93–106.

Fessler, John R, Kulick, Jonathan D & Eaton, John K 1994 Preferential concentration of heavy particles in a turbulent channel flow. *Physics of Fluids* **6** (11), 3742–3749.

Finn, Justin, Shams, Ehsan & Apte, Sourabh V 2011 Modeling and simulation of multiple bubble entrainment and interactions with two dimensional vortical flows. *Physics of Fluids* **23** (2), 023301.

Finn, Justin R, Li, Ming & Apte, Sourabh V 2016 Particle based modelling and simulation of natural sand dynamics in the wave bottom boundary layer. *Journal of Fluid Mechanics* **796**, 340–385.

Fox, Rodney O 2014 On multiphase turbulence models for collisional fluid–particle flows. *Journal of Fluid Mechanics* **742**, 368–424.

Germano, Massimo, Piomelli, Ugo, Moin, Parviz & Cabot, William H 1991 A dynamic subgrid-scale eddy viscosity model. *Physics of Fluids A: Fluid Dynamics* **3** (7), 1760–1765.

Goldman, Arthur Joseph, Cox, Raymond G & Brenner, Howard 1967 Slow viscous motion of a sphere parallel to a plane wall—i motion through a quiescent fluid. *Chemical engineering science* **22** (4), 637–651.

Gondret, P, Hallouin, E, Lance, M & Petit, L 1999 Experiments on the motion of a solid sphere toward a wall: From viscous dissipation to elastohydrodynamic bouncing. *Physics of Fluids* **11** (9), 2803–2805.

Gore, RA & Crowe, Clayton T 1989 Effect of particle size on modulating turbulent intensity. *International Journal of Multiphase Flow* **15** (2), 279–285.

Gualtieri, Paolo, Picano, F, Sardina, Gaetano & Casciola, Carlo Massimo 2015 Exact regularized point particle method for multiphase flows in the two-way coupling regime. *Journal of Fluid Mechanics* **773**, 520–561.

He, X, Karra, S, Pakseresht, P, Apte, SV & Elghobashi, S 2018 Effect of heated-air blanket on the dispersion of squames in an operating room. *International Journal for Numerical Methods in Biomedical Engineering* **34** (5), e2960.

Herrmann, Marcus 2010*a* Detailed numerical simulations of the primary atomization of a turbulent liquid jet in crossflow. *Journal of Engineering for Gas Turbines and Power* **132** (6), 061506.

Herrmann, Marcus 2010*b* A parallel Eulerian interface tracking/Lagrangian point particle multi-scale coupling procedure. *Journal of Computational Physics* **229** (3), 745–759.

Herrmann, Marcus 2011 On simulating primary atomization using the refined level set grid method. *Atomization and Sprays* **21** (4), 283–301.

Van der Hoef, MA, van Sint Annaland, M, Deen, NG & Kuipers, JAM 2008 Numerical simulation of dense gas-solid fluidized beds: a multiscale modeling strategy. *Annu. Rev. Fluid Mech.* **40**, 47–70.

Horwitz, Jeremy, Iaccarino, Gianluca, Eaton, John & Mani, Ali 2019 Comparison of euler-lagrange schemes in two-way coupled particle-laden channel flow. *Bulletin of the American Physical Society* .

Horwitz, JAK & Mani, Ali 2016 Accurate calculation of stokes drag for point–particle tracking in two-way coupled flows. *Journal of Computational Physics* **318**, 85–109.

Horwitz, JAK & Mani, A 2018 Correction scheme for point-particle models applied to a nonlinear drag law in simulations of particle-fluid interaction. *International Journal of Multiphase Flow* **101**, 74–84.

Hsiang, L-P & Faeth, Gerard M 1992 Near-limit drop deformation and secondary breakup. *Int. Journal of Multiphase Flows* **18** (5), 635–652.

Ibrahim, EA, Yang, HQ & Przekwas, AJ 1993 Modeling of spray droplets deformation and breakup. *Journal of Propulsion and Power* **9** (4), 651–654.

IRELAND, PETER J & DESJARDINS, OLIVIER 2017 Improving particle drag predictions in euler–lagrange simulations with two-way coupling. *Journal of Computational Physics* **338**, 405–430.

JOSEPH, DD, LUNDGREN, TS, JACKSON, R. & SAVILLE, DA 1990 Ensemble averaged and mixture theory equations for incompressible fluid-particle suspensions. *International Journal of Multiphase Flow* **16** (1), 35–42.

KAFTORI, D, HETSRONI, G & BANERJEE, S 1995 Particle behavior in the turbulent boundary layer. ii. velocity and distribution profiles. *Physics of Fluids* **7** (5), 1107–1121.

KAMRANI FARD, KIANA, MA, PENGLEI, PRIER, MICHAEL & LIBURDY, JAMES 2019 Numerical and experimental investigation of oscillating flexible foils with application in energy harvesting. *Bulletin of the American Physical Society* **64**.

KIGER, KT & PAN, C 2002 Suspension and turbulence modification effects of solid particulates on a horizontal turbulent channel flow. *J. Turbul* **3** (1).

KRZECZKOWSKI, STEFAN A 1980 Measurement of liquid droplet disintegration mechanisms. *International Journal of Multiphase Flow* **6** (3), 227–239.

KUERTEN, JOHANNES GM & VREMAN, AW 2015 Effect of droplet interaction on droplet-laden turbulent channel flow. *Physics of Fluids* **27** (5), 053304.

KULICK, J.D., FESSLER, J.R. & EATON, J.K. 1994 Particle response and turbulence modification in fully developed. *J. Fluid Mech.* **277**, 109–134.

LEBAS, ROMAIN, BLOKKEEL, GREGORY, BEAU, P-A & DEMOULIN, F-X 2005 Coupling vaporization model with the Eulerian-Lagrangian spray atomization (ELSA) model in diesel engine conditions. *SAE Technical Paper* (No. 2005-01-0213).

LEITH, DAVID 1987 Drag on nonspherical objects. *Aerosol science and technology* **6** (2), 153–161.

LIANG, CHAO, FEIGL, KATHLEEN A & TANNER, FRANZ X 2017 Axisymmetric simulations of drop deformation and breakup for validation of a modified taylor analogy breakup model. *Atomization and Sprays* **27** (5).

LIU, ALEX B, MATHER, DANIEL & REITZ, ROLF D 1993 Modeling the effects of drop drag and breakup on fuel sprays. *SAE Transactions* pp. 83–95.

Liu, Kai, Lakhote, Mandar & Balachandar, S 2019 Self-induced temperature correction for inter-phase heat transfer in euler-lagrange point-particle simulation. *Journal of Computational Physics* **396**, 596–615.

Lomholt, S, Stenum, B & Maxey, MR 2002 Experimental verification of the force coupling method for particulate flows. *International Journal of Multiphase Flow* **28** (2), 225–246.

Lu, SS & Willmarth, WW 1973 Measurements of the structure of the reynolds stress in a turbulent boundary layer. *Journal of Fluid Mechanics* **60** (3), 481–511.

Lyn, D.A. 1988 A similarity approach to turbulent sediment-laden flows in open channles. Turbulence and turbulent transport in sediment-laden open channel. *J. Fluid Mech.* **193**, 1–26.

Marchioli, Cristian 2017 Large-eddy simulation of turbulent dispersed flows: a review of modelling approaches. *Acta Mechanica* **228** (3), 741–771.

Maxey, MR 1987 The gravitational settling of aerosol particles in homogeneous turbulence and random flow fields. *Journal of Fluid Mechanics* **174**, 441–465.

Maxey, MR & Patel, BK 2001 Localized force representations for particles sedimenting in stokes flow. *International journal of multiphase flow* **27** (9), 1603–1626.

Maxey, MR, Patel, BK, Chang, EJ & Wang, L-P 1997 Simulations of dispersed turbulent multiphase flow. *Fluid Dynamics Research* **20** (1-6), 143–156.

Maxey, Martin R & Riley, James J 1983 Equation of motion for a small rigid sphere in a nonuniform flow. *The Physics of Fluids* **26** (4), 883–889.

McLaughlin, John B 1989 Aerosol particle deposition in numerically simulated channel flow. *Physics of Fluids A: Fluid Dynamics* **1** (7), 1211–1224.

Mehrabadi, M, Horwitz, JAK, Subramaniam, S & Mani, A 2018 A direct comparison of particle-resolved and point-particle methods in decaying turbulence. *Journal of Fluid Mechanics* **850**, 336–369.

Moin, Parviz & Apte, Sourabh V 2006 Large-eddy simulation of realistic gas turbine combustors. *AIAA Journal* **44** (4), 698–708.

MOIN, PARVIZ, SQUIRES, KYLE, CABOT, W & LEE, SANGSAN 1991 A dynamic subgrid-scale model for compressible turbulence and scalar transport. *Physics of Fluids A: Fluid Dynamics* **3** (11), 2746–2757.

MOSER, ROBERT D, KIM, JOHN & MANSOUR, NAGI N 1999 Direct numerical simulation of turbulent channel flow up to re τ= 590. *Physics of fluids* **11** (4), 943–945.

MOSTAFA, AA, MONGIA, HC, McDONELL, VG & SAMUELSEN, GS 1989 Evolution of particle-laden jet flows-a theoretical and experimental study. *AIAA Journal* **27** (2), 167–183.

MUKHERJEE, DEBANJAN, PADILLA, JOSE & SHADDEN, SHAWN C 2016 Numerical investigation of fluid–particle interactions for embolic stroke. *Theoretical and Computational Fluid Dynamics* **30** (1-2), 23–39.

MÜLLER, KATHRIN, FEDOSOV, DMITRY A & GOMPPER, GERHARD 2016 Understanding particle margination in blood flow–a step toward optimized drug delivery systems. *Medical engineering & physics* **38** (1), 2–10.

MUSTE, M. & PATEL, V.C. 1997 Velocity profiles for particles and liquid in open-channel flow with suspended sediment. *J. Hydr. Engng. ASCE* **123**, 742–751.

MUSTE, M., YU, K., FUJITA, I. & ETTEMA, R. 2009 Two phase flow insights into open channle flows with suspended particls of different densities open channel. *Environ Fluid Mech.* **9**, 161–186.

NING, WEI, REITZ, ROLF D, DIWAKAR, RAMACHANDRA & LIPPERT, ANDREAS M 2009 An Eulerian-Lagrangian spray and atomization model with improved turbulence modeling. *Atomization and Sprays* **19** (8), 727–739.

O'NEILL, ME 1967 A slow motion of viscous liquid caused by a slowly moving solid sphere: an addendum. *Mathematika* **14** (2), 170–172.

O'NEILL, MICHAEL E 1964 A slow motion of viscous liquid caused by a slowly moving solid sphere. *Mathematika* **11** (1), 67–74.

O'ROURKE, PJ & BRACCO, FV 1980 Modeling of drop interactions in thick sprays and a comparison with experiments. *Proceedings of the Institution of Mechanical Engineers* **9**, 101–106.

O'Rourke, Peter J 1985 The KIVA computer program for multidimensional chemically reactive fluid flows with fuel sprays. In *Numerical Simulation of Combustion Phenomena*, pp. 74–89. Springer.

O'Rourke, Peter J & Amsden, Anthony A 1987 The TAB method for numerical calculation of spray droplet breakup. *SAE Technical Paper* (No. 872089).

Pakseresht, Pedram & Apte, Sourabh 2018 Volumetric displacement effects of the gaseous phase on the euler-lagrange prediction of spray atomization. *Bulletin of the American Physical Society* **63**.

Pakseresht, Pedram, Apte, Sourabh & Finn, Justin 2014 Ineractions of turbulence and sediment particles in an open channel flow. In *APS Meeting Abstracts*.

Pakseresht, Pedram, Apte, Sourabh & Finn, Justin 2015 Dns with discrete element modeling of suspended sediment particles in an open channel flow. In *APS Division of Fluid Dynamics Meeting Abstracts*.

Pakseresht, Pedram, Apte, Sourabh & Finn, Justin 2016 Dns-dem of suspended sediment particles in an open channel flow. In *APS Meeting Abstracts*.

Pakseresht, Pedram & Apte, Sourabh V 2017 Prediction of a densely loaded particle-laden jet using a euler-lagrange dense spray model. In *APS Division of Fluid Dynamics Meeting Abstracts*.

Pakseresht, Pedram & Apte, Sourabh V 2019*a* Modeling the dense spray regime using an euler-lagrange approach with volumetric displacement effects. *arXiv preprint arXiv:1910.00746* .

Pakseresht, Pedram & Apte, Sourabh V 2019*b* Volumetric displacement effects in euler-lagrange les of particle-laden jet flows. *International Journal of Multiphase Flow* **113**, 16–32.

Pakseresht, Pedram, Apte, Sourabh V & Finn, Justin R 2017 On the predictive capability of DNS-DEM applied to suspended sediment-turbulence interactions. In *ASME 2017 Fluids Engineering Division Summer Meeting*, pp. V01BT11A025–V01BT11A025. American Society of Mechanical Engineers.

Pakseresht, P., Bahrainian, S.S. & Bahoosh Kazerooni, R. 2012 An algorithm in element deletion process used in moving three zones unstructured grid for arbitrary relative motion of two objects. In *Proceedings of 3 rd International Conference on Theoretical and Applied Mechanics, Athens, Gr*.

Pakseresht, Pedram, Esmaily, Mahdi & Apte, Sourabh V 2019 A correction scheme for two-way coupled euler-lagrange wall-bounded flows. *Bulletin of the American Physical Society* .

Pakseresht, Pedram, Esmaily, Mahdi & Apte, Sourabh V 2020 A general velocity correction scheme for two-way coupled point-particle simulations. *Submitted to Journal of Computational Physics* .

Pan, Y & Banerjee, S 1996 Numerical simulation of particle interactions with wall turbulence. *Physics of Fluids* **8** (10), 2733–2755.

Paris, AD & Eaton, JK 2001 Turbulence attenuation in particle-laden channel flow. report no. tsd-137, dept. *Mech. Engr., Stanford University* .

Park, Jong-Hoon, Yoon, Youngbin & Hwang, Sang-Soon 2002 Improved tab model for prediction of spray droplet deformation and breakup. *Atomization and sprays* **12** (4).

Patankar, NA & Joseph, DD 2001*a* Lagrangian numerical simulation of particulate flows. *International Journal of Multiphase Flow* **27** (10), 1685–1706.

Patankar, NA & Joseph, DD 2001*b* Modeling and numerical simulation of particulate flows by the Eulerian–Lagrangian approach. *International Journal of Multiphase Flow* **27** (10), 1659–1684.

Pedinotti, S, Mariotti, G & Banerjee, S 1992 Direct numerical simulation of particle behaviour in the wall region of turbulent flows in horizontal channels. *International journal of multiphase flow* **18** (6), 927–941.

Pierce, Charles D & Moin, Parviz 1998 A dynamic model for subgrid-scale variance and dissipation rate of a conserved scalar. *Physics of Fluids* **10** (12), 3041–3044.

Pouransari, Hadi & Mani, Ali 2017 Effects of preferential concentration on heat transfer in particle-based solar receivers. *Journal of Solar Energy Engineering* **139** (2), 021008.

REITZ, ROLFD 1987 Modeling atomization processes in high-pressure vaporizing sprays. *Atomisation and Spray Technology* **3** (4), 309–337.

RIGHETTI, M & ROMANO, GIOVANNI PAOLO 2004 Particle–fluid interactions in a plane near-wall turbulent flow. *Journal of Fluid Mechanics* **505**, 93–121.

ROGERS, CB & EATON, JK 1991 The effect of small particles on fluid turbulence in a flat-plate, turbulent boundary layer in air. *Physics of Fluids A: Fluid Dynamics* **3** (5), 928–937.

ROUSON, DAMIAN WI & EATON, JOHN K 2001 On the preferential concentration of solid particles in turbulent channel flow. *Journal of Fluid Mechanics* **428**, 149–169.

SAFFMAN, PGT 1965 The lift on a small sphere in a slow shear flow. *Journal of Fluid Mechanics* **22** (02), 385–400.

SEGURA, J.C. 2004 Predictive Capabilities of Particle-Laden Large Eddy Simulation. PhD Thesis, Stanford University.

SHAMS, EHSAN, FINN, J & APTE, SV 2011 A numerical scheme for Euler–Lagrange simulation of bubbly flows in complex systems. *International Journal for Numerical Methods in Fluids* **67** (12), 1865–1898.

SIALA, FIRAS F, KAMRANI FARD, KIANA & LIBURDY, JAMES A 2020 Experimental study of inertia-based passive flexibility of a heaving and pitching airfoil operating in the energy harvesting regime. *Physics of Fluids* **32** (1), 017101.

SNIDER, DM 2001 An incompressible three-dimensional multiphase particle-in-cell model for dense particle flows. *Journal of Computational Physics* **170** (2), 523–549.

SOR, SUTHYVANN & GARCÍA-MAGARIÑO, ADELAIDA 2015 Modeling of droplet deformation near the leading edge of an airfoil. *Journal of Aircraft* **52** (6), 1838–1846.

SQUIRES, KYLE D & EATON, JOHN K 1990 Particle response and turbulence modification in isotropic turbulence. *Physics of Fluids A: Fluid Dynamics* **2** (7), 1191–1203.

SQUIRES, KYLE D & EATON, JOHN K 1991 Preferential concentration of particles by turbulence. *Physics of Fluids A: Fluid Dynamics* **3** (5), 1169–1178.

TAKEMURA, FUMIO & MAGNAUDET, JACQUES 2003 The transverse force on clean and contaminated bubbles rising near a vertical wall at moderate reynolds number. *Journal of Fluid Mechanics* **495**, 235–253.

TAYLOR, G I 1963 The shape and acceleration of a drop in a high speed airstream. *The scientific papers by G.I. Taylor, edited by G.K. Batchelor,* **III Univ. Press, Cambridge, UK.**

TENNETI, S, GARG, R & SUBRAMANIAM, S 2011 Drag law for monodisperse gas–solid systems using particle-resolved direct numerical simulation of flow past fixed assemblies of spheres. *International Journal of Multiphase Flow* **37** (9), 1072–1092.

TSUJI, YUTAKA, TANAKA, TOSHITSUGU & ISHIDA, T 1992 Lagrangian numerical simulation of plug flow of cohesionless particles in a horizontal pipe. *Powder Technology* **71** (3), 239–250.

VALLET, A & BORGHI, R 1999 An Eulerian model of atomization of a liquid jet. *Comptes Rendus de l'Academie des Sciences Series IIB Mechanics Physics Astronomy* **327** (10), 1015–1020.

VALLET, A, BURLUKA, AA & BORGHI, R 2001 Development of a Eulerian model for the "atomization" of a liquid jet. *Atomization and Sprays* **11** (6), 619–642.

VASSEUR, P & COX, RG 1977 The lateral migration of spherical particles sedimenting in a stagnant bounded fluid. *Journal of Fluid Mechanics* **80** (3), 561–591.

VREMAN, A.W. 2007 Turbulence characteristics of particle-laden pipe flow. *Journal of Fluid Mechanics* **584**, 235–279.

VREMAN, AW, GEURTS, BERNARDUS J, DEEN, NIELS G & KUIPERS, JAM 2004 Large-eddy simulation of a particle-laden turbulent channel flow. In *Direct and Large-eddy Simulation V*, pp. 271–278. Springer.

WANG, CHEN, CHANG, SHINAN, WU, HONGWEI, DING, LIANG & THOMPSON, JM 2015 Theoretical modeling of spray drop deformation and breakup in the multimode breakup regime. *Atomization and Sprays* **25** (10).

WANG, CHAO, CHANG, SHINAN, WU, HONGWEI & XU, J 2014 Modeling of drop breakup in the bag breakup regime. *Applied Physics Letters* **104** (15), 154107.

Wang, Qunzhen & Squires, Kyle D 1996 Large eddy simulation of particle-laden turbulent channel flow. *Physics of Fluids* **8** (5), 1207–1223.

Yamamoto, Yasufumi, Potthoff, Matthias, Tanaka, Toshitsugu, Kajishima, Tsui & Tsuji, Yutaka 2001 Large-eddy simulation of turbulent gas–particle flow in a vertical channel: effect of considering inter-particle collisions. *Journal of Fluid Mechanics* **442**, 303–334.

Yu, Kwonkyu, Yoon, Byungman & Kim, Dongsu 2014 Re-evaluation of change of mean velocity profiles in turbulent open-channel flows due to introducing sediment particles. *KSCE Journal of Civil Engineering* **18** (7), 2261–2267.

Zeng, Lanying, Najjar, Fady, Balachandar, S & Fischer, Paul 2009 Forces on a finite-sized particle located close to a wall in a linear shear flow. *Physics of fluids* **21** (3), 033302.